Metal oxide semiconductors as humidity and NOx sensors for environmental monitoring

Chapter 5 - Glass – Ceramic sensors

5.1. Ceramic Materials and Sensors

In today's information-oriented age, computer-based systematization is penetrating through the factory and the office into homes. As a result, recent automated systems require various kinds of sensors. Functional ceramic materials, which are superior in physical strength and chemical resistance as well as the electrical properties, are widely used to satisfy diverse needs for sensing devices. Improved results have especially been obtained in the field of atmospheric sensors, e.g. temperature, humidity and gas sensors.

The controlled-pore ceramics are suitable for atmospheric sensors such as humidity and gas sensors.

In addition, most materials, including ceramics, are not single-functional, but are multifunctional in nature. Thus, attempts to develop multifunctional devices are directed toward making full use of the intrinsic multiple functions of materials. Humidity or gas sensors are normally exposed to atmospheres containing various other components and tend to lose their inherent sensitive properties during use as a result of several complicated physical and chemical processes between these components and various materials. Therefore, major research effort is being directed toward developing highly reliable and functional ceramic materials [1].

Ceramics are usually prepared by a relatively simple process consisting of mixing raw materials, forming the part, and sintering. Sintered ceramics are composed essentially of a large number of crystal grains.

Ceramics are characterized by their unique structure consisting of crystal grains, grain boundaries, surfaces, and pores, as shown in Fig.5.1.

The representative ceramic sensors are summarized in Table 5.1.

Table 5.1. Examples of ceramic sensors [1]

Sensor	Sensor Ceramic Material	Sensor Function
Temperature	(Mn, Cu) (Mn, Co, Ni)$_2O_4$, $CoAl_2O_4$, $NiAl_2O_4$, $Mg(Al, Cr, Fe)_2O_4$, SiC $BaTiO_3$ VO_2, (Mn, Zn) Fe_2O_4	NTC thermistor PTC thermistor Temperature switch
Humidity	$MgCr_2O_4$-TiO_2, V_2O_5-TiO_2, $ZnCr_2O_4$-$LiZnVO_4$, Al_2O_3, $Ca_{10}(PO_4)_6(OH)_2$ ZrO_2-MgO	H_2O (Ionic conduction) H_2O (Electronic conduction)
Gas	SnO_2, ZnO, γ-Fe_2O_3, α-Fe_2O_3, TiO_2, CoO-MgO ZrO_2-CaO, MgO, Y_2O_3	CH_4, i-C_4H_{10} etc. } Electronic conduction O_2 O_2 (Ionic conduction)
Ion	AgX (X: Cl, Br, I, CN, SCN) PbS-Ag_2S, CdS-Ag_2S CuS-Ag_2S, LaF_3	Ion selective electrode
Position velocity	Pb (Zr, Ti) O_3	Piezoelectricity
Optics	$PbTiO_3$, $LiTaO_3$ $LiNbO_3$, Pb (Zr, Ti) O_3 CaF_2, Li_2B4O_7	Pyroelectricity (Infrared detection) Thermoluminescence

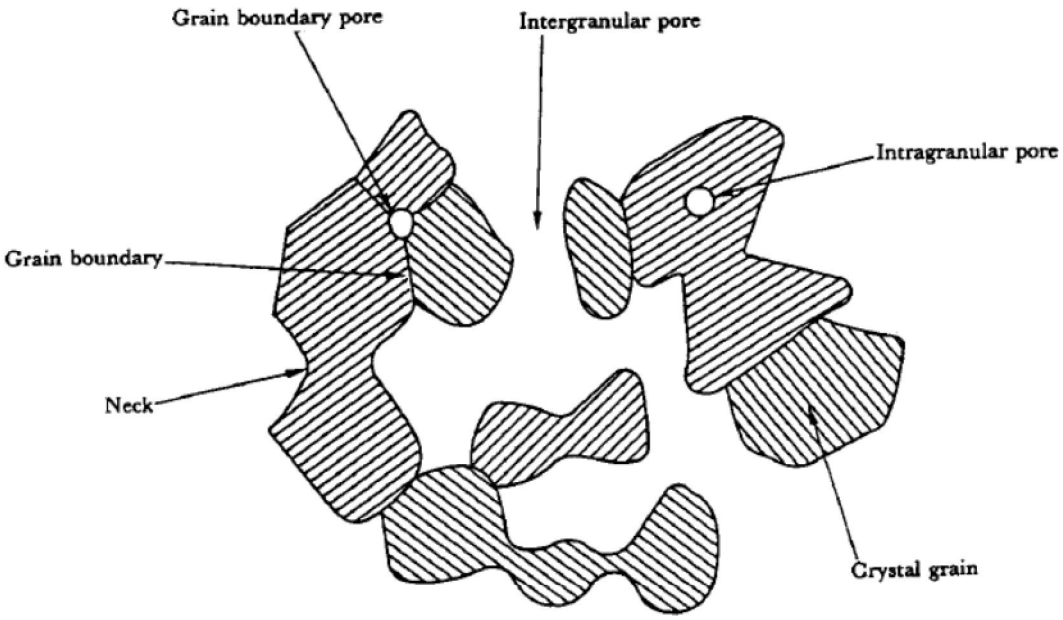

Fig.5.1. Schematic drawing of a typical ceramic microstructure

Both high-density and porous ceramics are easily produced by controlling the sintering conditions. Furthermore, in ceramic materials, solid solutions can form more easily than they can in single crystals, and improving properties is also easier. Moreover, a ceramic form sintered at high temperature is essentially more stable physically, chemically, and thermally than the powder form.

Many ceramic sensors utilize the electrical properties of crystal grains themselves in high-density ceramics, which are comparable to those of single crystals. For example, the temperature dependence of electrical properties find practical use in temperature sensors, and the piezoelectric properties are useful in ultrasonic sensors. Moreover, the electrical properties of grain boundaries in semiconductor ceramics are applied in sensing devices. For instance, in a semiconductor of ferroelectric material such as $BaTiO_3$, a positive temperature coefficient of resistance (PTCR) is obtained indicating that the resistance changes rapidly in the vicinity of the Curie point.

On the other hand, the surfaces and open pores in ceramics tend to collect water vapor and gases by absorption, adsorption, and condensation. Especially in semiconductor ceramics, electrical properties are largely related to the porosity and the pore size of the open pores. The pore-surface conductivity changes with even small changes in humidity or with the adsorption of various gases.

These ceramics are called porous ceramics, as opposed to high-density ceramics. Since gas adsorption in porous ceramics causes changes in surface electrical properties, the material can be used as humidity or gas sensors.

As noted above, humidity or gas sensors are usually exposed to atmospheres containing various other components and tend to lose their inherent sensitive properties during use because of a number of complicated physical and chemical processes which occur between these components and various materials. Major

research effort is thus being directed toward developing highly reliable and function ceramic materials.

In addition, most materials, including ceramics, are not single-functional but multifunctional in nature. Therefore, the key to success in developing a single functional material is the technology of masking undesired functions.

Many recently developed systems require a device that can perform various functions with a single element. As an example, in atmospheric sensors based on physical surface properties there has been a recent demand for a multifunctional sensor that can simultaneously, yet independently, measure the humidity and the presence of a gas, or sometimes both humidity and temperature.

Thus, attempts to make multifunctional devices are directed toward making active use of the intrinsic multiple functions of materials. In developing multifunctional devices, it is important to establish technology that can discriminate signals without cross talk in place of the conventional masking technology. For instance, from a multifunctional point of view, a ceramic sensor can exhibit two or more functions such as sensing temperature, humidity, gas as well as acting as a catalyzer, with high or low sensitivity. Thus, the multifunctional ceramic sensor effectively utilizes adsorption on the ceramic grain surface as well as the crystal grain property.

As mentioned above, ceramic materials with their unique structure consisting of crystal grains, grain boundaries, surfaces, and pores are suitable for multifunctional as well as single-functional atmospheric sensors such as humidity and gas.

5. 2. Adsorption and Ceramics

Adsorption of gases is an important property of solid surfaces. There are probably at least two different types of adsorption, physisorption and chemisorption. Adsorption isobars often take the shape such as that shown in Fig.5.2. Three or more regions are found for the adsorption of a particular gas on a particular solid.

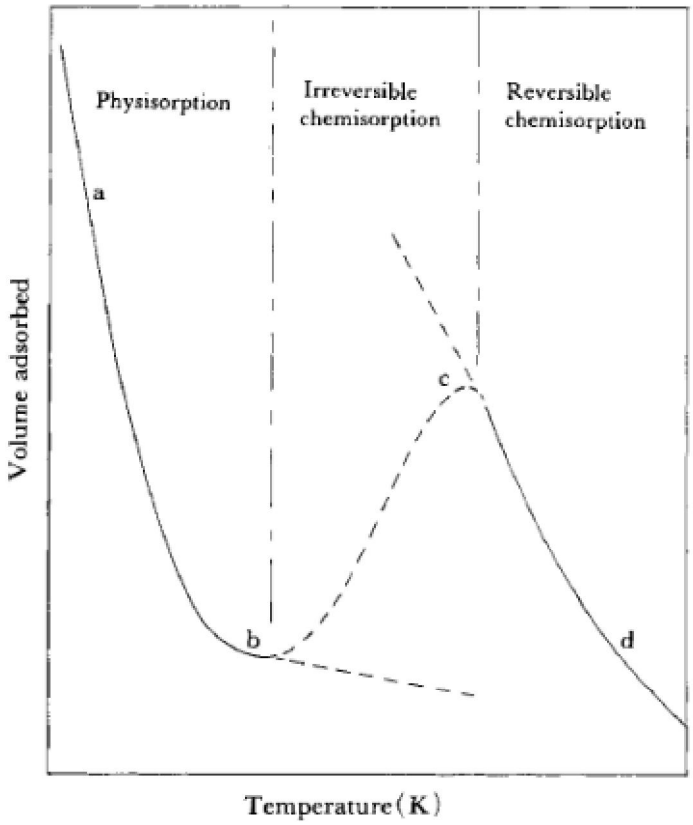

Fig.5.2. Adsorption isobar.

At low temperatures of region a-b, physisorption occurs, where the surface coverage is at equilibrium and decreases with increasing temperature. At some temperatures, a region b-c of irreversible chemisorption is reached. The activation energy will increase with coverage, and the rate of adsorption decreases with coverage. If at each temperature, the outgassed sample is permitted to adsorb gas for a given time, a curve shape as indicated by the dotted line may be obtained. At this temperature, desorption

will not occur by simply lowering the pressure. High-temperature outgassing is required.

At temperatures high enough to overcome the activation energy (region c-d), reversible chemisorption is in principle reached, and the volume chemisorbed decreases with increasing temperature. However, behavior in this high temperature region is often masked by chemical reactions.

The surfaces of most metal oxides usually exhibit a complex structure comprising metal ions, oxygen ions, impurities, and imperfections. Thus, there are many interactions between adsorbates and surface states. In atmospheres containing water vapor, for example, the surfaces of metal oxides are covered by hydroxyl groups on which water molecules adsorb through formation of hydrogen bonds. The surface hydroxyl groups can generally be removed by dehydration at higher temperatures in vacuum.

However, the surface structure of metal oxides in powder form is easily subject to permanent changes by repeated heat-cleaning cycles at high temperatures.

On the other hand, a ceramic body sintered at high temperature is essentially more stable physically, chemically, and thermally than the powder form.

As with many porous systems, controlled-pore ceramics adsorb gases throughout the pore structure. The adsorption of gases generally tends to occur preferentially on the necks of the grain surfaces. The neck usually exhibits properties closely related to the crystal grain itself. In particular, a metal oxide ceramic semiconductor tends to exhibit changes in electrical conductivity due to the adsorption of gases on the necks [1].

In general, electrical and magnetic properties of ceramic materials can be utilized in sensors applications. Materials suitable for these applications include: (1) ionic and

electronic conductors, (2) ferroelectric and piezoelectric, (3) magnetic and (4) electro-optic materials.

Electrical conduction of ceramic materials can be used to measure temperature and gas concentrations [2].

5.3. Electrical Conduction in Ceramic Materials

The electrical conductivity of a solid is the sum of the contributions of all conducting species. The total electrical conductivity of a solid can be expressed as follows:

$$\sigma = \Sigma\, n\, z\, e\, \mu \quad (1)$$

Where σ is the electrical conductivity, n is the charge carrier concentration, z is the charge of the conducting species in units of e, e is the elementary charge and μ is the mobility.

In oxide ceramics, the charge carriers can be either ions or electrons. The sources of these species could either be generated by thermal agitation (intrinsic) or by aliovalent substitutions (extrinsic).

5.3.1. Charge carriers

5.3.1.1. Intrinsic charge carriers in stoichiometric hosts

Intrinsic charge carriers in stoichiometric hosts are generated by thermal agitation, and when the ions are activated and migrate to the surface of the crystal, ionized vacancies are formed in the lattice illustrating the following relationship:

$$nil = V_m'' + V_O.. \quad (2)$$

Where V_m'' stands for the double ionized metal vacancies, $V_O..$ for double ionized oxygen vacancies in the crystalline lattice and 'nil' represents the defect-free lattice. Electrons (e^-) can be activated to the conduction band by thermal energy leaving

electron holes (+) in the valency band. Thus, both electrons in the conduction band and the holes in the valency band are charge carriers:

$$nil = [e^-] + [+] \quad (3)$$

For intrinsic ionic charge carriers, under equilibrium conditions, according to the mass action law, the concentration of charge carriers is

$$n = Vm'' = V_{O}.. = C' \exp(-\Delta H_f/2kT) \quad (4)$$

Where C' is a constant, ΔH_f is the enthalpy of formation, k is Boltzmann's constant and T is the temperature. For the intrinsic electronic charge carriers

$$n = [e^-] = [+] = C'' \exp(-E_g/2kT) \quad (5)$$

E_g is the energy required to excite the electrons across the energy gap.

5.3.1.2. Non-stoichiometry

A third type of intrinsic defect occurs in crystalline material where the ions can have more than one stable valency state. Metal oxides with normal divalent cations, that can tolerate a small concentration (x) of trivalent cations in certain temperature and oxygen partial pressure regions, can become non-stoichiometric and have the chemical formula

$$M^{2+}_{1-x} M^{3+}_{x} O^{2-}_{1+x/2} \quad (6)$$

A possible reaction for the creation of the M^{3+} states preserving the charge balance in the lattice of these oxides is

$$2M^{2+} + \frac{1}{2}O_2 = 2M^{3+} + V_{M*} + O^{2-} \quad (7)$$

Under equilibrium conditions,

$$[M^{3+}]^2 [V_{M*}] / P_{O2}^{1/2} = C \exp(-\Delta H_f/2kT) \quad (8)$$

Where $[V_{M*}]$ is metal vacancy, and has no effective charge. The hole mobility will be higher than that of the ionic vacancies, hence the dominating charge carriers in this case will be positive holes. This solid will appear to be a p-type semiconductor.

Since $[M^{3+}] = [+] = 2[V_M]$ (9)

then $[+] = P_{O2}^{1/6} \; C` exp(-\Delta H_f/3kT)$ (10)

Using the same treatment, in tetravalent metal oxides a small amount of ions of a lower oxidation state (3^+) may exist in the lattice, and the charge carriers will be negatively charged electrons, as in an n-type semiconductor.

Then, the charge carrier concentration will be

$$[e^-] = P_{O2}^{1/6} \; C` exp(-\Delta H_f/3kT) \quad (11)$$

5.3.1.3. Extrinsic charge carriers

Extrinsic charge carriers are generated by aliovalent chemical substitutions. An example of extrinsic ionic charge carriers is cubic stabilized zirconia.

In the ZrO_2 - Y_2O_3 system, Y^{3+} ions substituting Zr^{4+} ions stabilize the cubic fluorite structure. The Zr^{4+} ions are in the most stable oxidation state, and the charge neutrality in the lattice will be preserved by the generation of oxygen vacancies. The presence of a high concentration of oxygen vacancies results in a high oxygen ion diffusion rate and hence high ionic conductivity.

Nb_2O_5-doped TiO_2 and Li_2O-doped NiO are examples of extrinsic electronic semiconductors. Nb_2O_5-doped TiO_2 is an n-type semiconductor.

The pentavalent Nb^{5+} ions substitute Ti^{4+} ions in the lattice and the electrical neutrality is maintained by reducing Ti^{4+} to Ti^{3+}. Li_2O-doped NiO is a p-type

semiconductor. When Li^{+} ions are present in the NiO lattice, the electrical neutrality is maintained by oxidizing the Ni^{2+} to Ni^{3+}.

Hence, the charge carrier concentration can be estimated from the concentration of the dopant.

Frozen-in non-stoichiometric defects are also considered as extrinsic charge carriers. The temperature dependence of the conductivity of NiO from Mitoff's paper (1966) [3] is given in Fig.5.3. The line A-G represents the high temperature conductivity of an intrinsic non-stoichiometric semiconductor.

The lines G-H, E-F and C-D were measured at lower temperatures where oxidation-reduction reactions could not proceed; hence, the charge carrier concentration remained constant. Therefore, their electrical conductivity can be considered as extrinsically electronic.

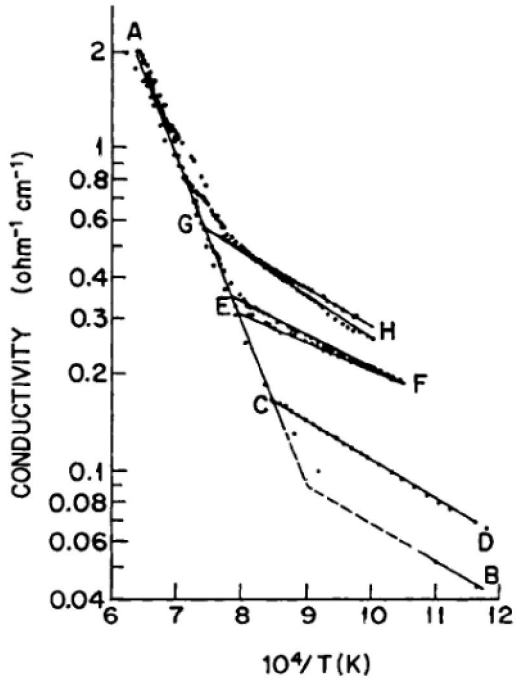

Fig.5.3. Temperature dependence of the electrical conductivity of NiO [3].

5.3.1.4. Mobility

In ceramic materials, the mobility μ of the ionic charge carriers is described by a 'hopping' mechanism which follows the relationship

$$\mu = (C/T) \exp(-\Delta H^*/kT) \quad (12)$$

Where C is a constant and ΔH^* is the enthalpy change.

For broadband materials, the mobility should be described by a scattering mechanism. For sensor applications, this type of material is seldom encountered.

In narrow band electronically conducting ceramic materials, the mobility follows either the large polaron or small polaron model. For most sensor applications the mobility follows the 'small polaron' or 'hopping' model which is described by Equation 12.

5.4. Electrical conductivity in oxides

Electrical conductivity is the sum of the products of charge carrier concentration and mobility, as in Equation 1. In describing the conductivity of ceramic materials, the following possibilities have to be considered:

(1) Are the carriers ions, or electrons and holes?

(2) Is the mobility limited by scattering and collision (broadband), or by thermal activation over an energy barrier?

(3) Is the conductivity intrinsic, or dominated by chemical substitution?

(4) Is the host stoichiometric, or non-stoichiometric?

(5) Is thermodynamic equilibrium established with all important species contributing to the conductivity, or only some of them?

Considering these alternatives, according to Mitoff (1966) [3], the combinations offer 32 possible conduction mechanisms. Of these 32 possibilities, 24 are either demonstrated or possible examples in real materials.

5.5. Conduction Mechanisms

For sensor applications, only extrinsic ionic and extrinsic electronic conduction in stoichiometric hosts and intrinsic conduction in non-stoichiometric hosts were utilized. These sensors will be discussed separately according to their conduction mechanisms.

5.5.1. Sensor application using non-stoichiometric compounds

Under equilibrium conditions, the electrical conductivity of a non-stoichiometrical compound is described by the equation:

$$\sigma = (P_{O2}^{m} C''/T) \exp [(-\Delta H_f/3+\Delta H^*)/kT)] \quad (13)$$

where the exponent *m* has a positive value for p-type semiconducting metal oxides, and a negative value for n-type semiconducting metal oxides.

When the temperature is held constant, the electrical resistance of these non-stoichiometric compounds is a function of oxygen partial pressure under equilibrium conditions. The electrical resistance of semiconducting TiO_2 as a function of oxygen partial pressure is given in (Fig.5.4) [4]. The conductivity in the low oxygen partial pressure region is n-type. A slope change was observed in the higher oxygen pressure region which was caused by the presence of cation vacancies owing to the Al^{3+} ions acting as acceptors in the TiO_2 lattice.

TiO_2 has been used as an automotive exhaust gas sensor or equilibrium oxygen sensor as presented by Tien *et al.* (1975) [5], to measure and control the air-to-fuel (A/F) ratio of internal combustion engines. When the A/F mixture entering an internal

combustion engine is at the stoichiometric ratio, combustion can be described by the reaction

$$CH_X + yO_2 + 3.76\ N_2 \longrightarrow CO_2 + \tfrac{1}{2}\,xH_2O + 3.76yN_2 \quad (14)$$

If there is excess fuel (rich), CO will be the main residue product of combustion; but if there is excess air (lean), free oxygen will be present in the exhaust gas. The oxygen partial pressure of the exhaust gas will thus be determined by the free oxygen concentration in the lean region and by the CO/CO_2 ratio in the rich region. The theoretical equilibrium oxygen partial pressure of the exhaust gas as a function of A/F at 700°C is shown by the solid line in Fig.5.5, with the negative of the log of the partial oxygen pressure being shown at the left vertical axis. At the right-hand vertical axis, the resistance of the device is shown. The experimentally measured resistance of a TiO_2 sensor as a function of the A/F ratio at 700°C is shown on the curve as dots [5]. The agreement is excellent.

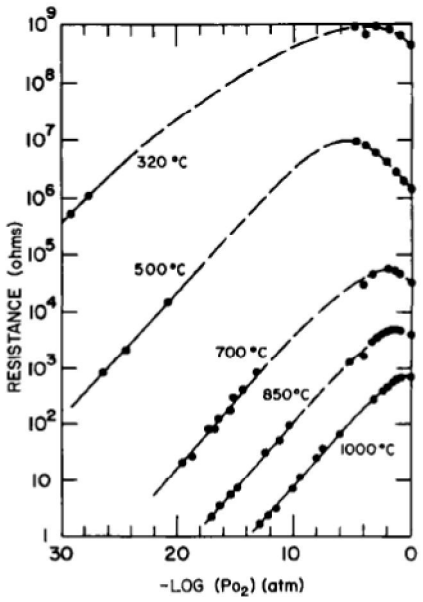

Fig.5.4. The electrical resistance of a TiO_2 sensor as a function of oxygen partial pressure. The material is a mixed-valency n-type semiconductor at low oxygen partial

pressure. At high oxygen pressures, the material becomes a p-type semiconductor owing to the presence of aluminium impurities [4].

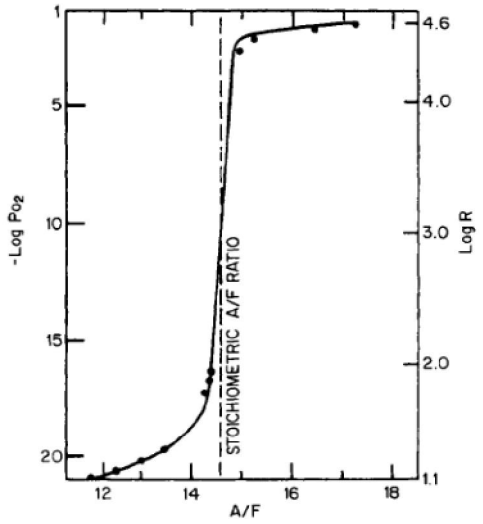

Fig.5.5. Equilibrium oxygen partial pressure vs air-to-fuel ratio at 700°C [5].

For automotive exhaust gas sensor applications, it is required that the sensor is operated at low temperatures and the response time has to be 100 milliseconds or shorter at its operating temperatures. It is necessary that the sensors should be porous and fine grained. For improved sensitivity of the sensors, catalysts are always used. Sensors without catalyst can only be operated at high temperatures. The catalysts help to bring the gas-gas and gas-solid reactions into equilibrium at lower temperatures.

A TiO_2 sensor design is illustrated in Fig.5.6. This sensor is made by a standard thick film process with a printed TiO_2 sensing element and a platinum heater on an alumina substrate [6]. The temperature dependence of the sensor resistance is given in Fig.5.7 for both Lean and rich exhaust gases [7].

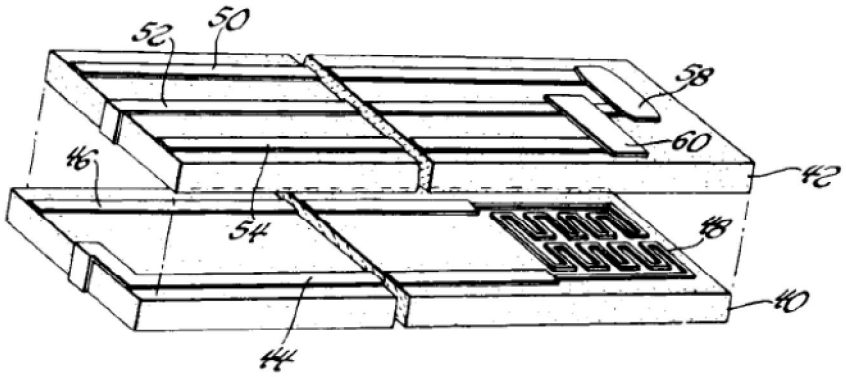

Fig.5.6. A thick-film TiO_2 sensor design [6].40 and 42 are alumina substrates, 44, 46, 50 and 52 are platinum electrodes, 48 is a Pt heater, 58 is a printed thick-film TiO_2 sensing element and 60 is a thermistor.

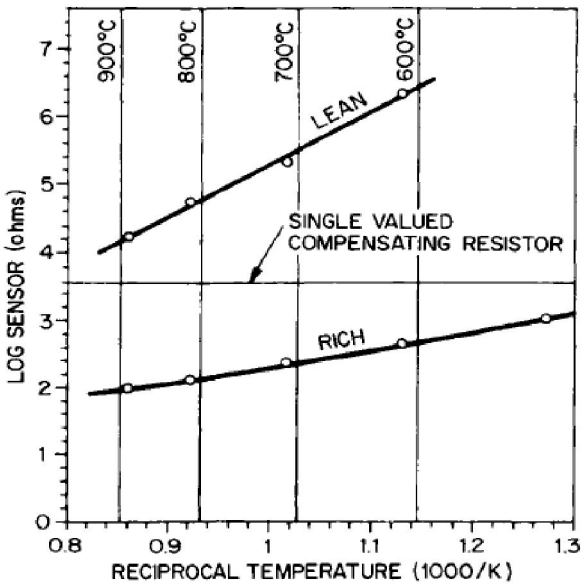

Fig.5.7. Temperature dependence of resistance of TiO_2 sensors [7].

The response time measured by the laboratory setup is given in Fig.5.8a. It should be noted that sufficient catalyst must be present for an acceptable sensor performance. A switching curve of a sensor without catalyst is given in Fig.5.8b. The switching time is defined as the time needed for the resistance to change from1/3 to 2/3 between the rich and lean value when the A/F ratio changes from rich to lean and vice versa.

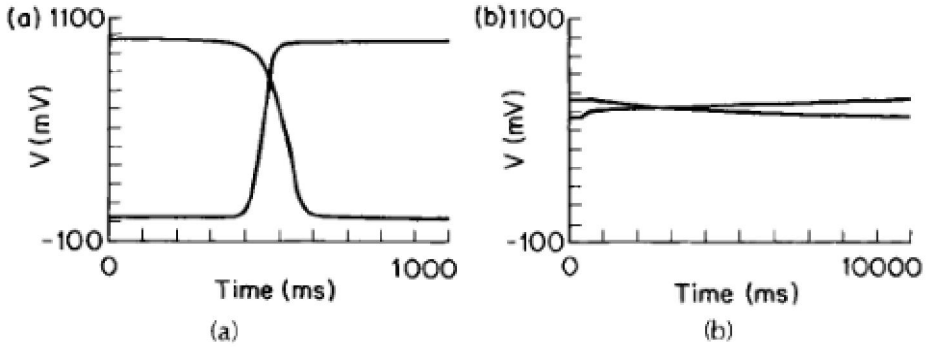

Fig.5.8. Response time of a TiO_2 sensor. The response times were measured at 550°C [7]. a) Sensor with a Pt catalyst. The rich-to-lean response time was 41 ms and the lean-to-rich response time was 25 ms. b) Sensor without a Pt catalyst. Response times were too long to be measured.

As shown in Fig.5.8a, the gas temperature was 547°C while the sensor was heated to 800°C.

5.5.2. Sensor application using extrinsic ionic conductors

Oxygen ion conducting metal oxides have been used as solid electrolytes in devices measuring equilibrium oxygen pressure in gas mixtures [8]. The sensor of this type is an oxygen concentration cell.

Reference gas, Pt | Oxygen ion conductor | Pt, sample gas

P_{O2}, $\mu°_{O2}$ ZrO_2-Y_2O_3 P_{O2}, μ_{O2}

The e.m.f. of the cell follows the equation

$$E = -(\mu_{O2} - \mu°_{O2})/4F = RT/4F(\ln P_{O2}/ P°_{O2}) \qquad (15)$$

Where F is the Faraday constant, μ is the chemical potential, P_{O2} is the oxygen partial pressure and R is the universal gas constant. The superscript (°) refers to the reference

gas. From the determination of E, the unknown oxygen pressure, P_{O2}, may be calculated when the partial pressure of oxygen in the reference gas, P^{o}_{O2}, is known. There are many other applications for an oxygen concentration cell of this type, as discussed by Jagannathan et al. (1980) [8]. This cell has been used as an automotive exhaust gas sensor [9]. The e.m.f. values, measured at the different A/F ratios of an automotive engine, are plotted in Fig.5.9.

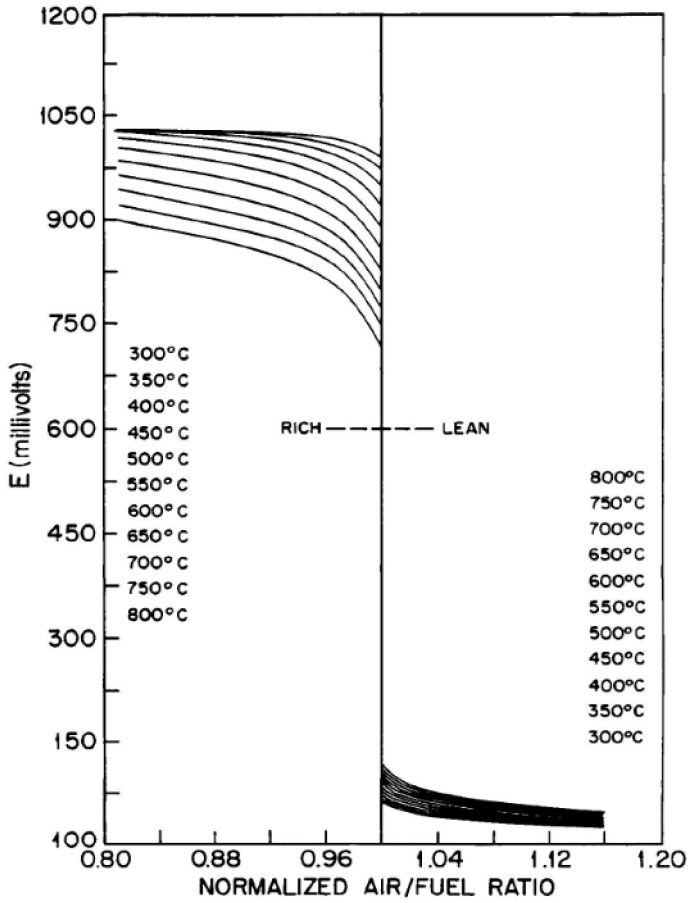

Fig.5.9. Characteristics of a galvanic (zirconia) automotive exhaust sensor [9].

This graph shows a discontinuity of the e.m.f. at the engine control point, where the A/F ratio is at the stoichiometry point. It is necessary for the exhaust gas mixture to be under equilibrium conditions at the gas-solid-electrode interfaces. In case equilibrium

conditions are not realized, the sensor will have a very low voltage value in the rich region. It is important that the electrodes should be catalytically active. TiO_2 sensors will also give high erroneous resistance values in the rich region if equilibrium is not established between the gas and the sensing element.

5.5.3. Sensor application using extrinsic electronic conductors

In general, based on the physical origins responsible for the response of a sensor, two types of oxide gas sensors can be distinguished: bulk conduction-based sensors and surface layer-controlled gas sensors.

5.5.3.1. Extrinsic electronic conductors - bulk effect

This class of materials includes mixed-valency semiconductors and nonstoichiometry compounds with frozen-in defects. The conductivity of these materials can be expressed as

$$\sigma = C''n \exp(- \Delta H^*/kT) \qquad (16)$$

Where n is the charge carrier concentration in a mixed-valency semiconducting compound or the concentration of frozen-in defects in a non-stoichiometric compound. The conductivity of these materials does not change with oxygen partial pressure in the temperature and the oxygen pressure region of interest.

Beyond this region, they become non-stoichiometric intrinsic semiconductors.

These materials have been used as thermistors. Transition metal oxide spinels and Li_2O-doped NiO are examples. From Equation 16, the slope of the log σ vs 1/T curve is lower than that of the intrinsic semiconductors, i.e. the activation energy ΔH^* is lower. It is desirable that the slope is higher. The value of ΔH^* can be increased by increasing the hopping distance for charge carriers. In a mixed-valency oxide

semiconductor, the hopping distance of charge carriers is to the nearest cation neighbor of the same element. This distance will be increased by forming solid solutions in the semiconducting oxide lattice.

On the other hand, the bulk conduction-based sensors involve gas solid reactions in series with a change in the stoichiometry of the bulk (grains) of the sensor material. The change in the bulk conductivity (σ) is a reflection of the equilibration between the oxygen activity in the oxide and the oxygen content (oxygen partial pressure, P_{O2}) in the surrounding atmosphere.

$$\sigma = \sigma_{0\,exp}\left(-\frac{E_a}{kT}\right)P_{O2}^{\pm 1/n} \quad (17)$$

Where σ_0 is a constant, E_a is the activation energy for conduction, and the magnitude and sign of $1/n$ are determined by the type of dominant bulk defect involved in the equilibration process. Sensors based on $SrTiO_3$ and Nb_2O_5 for example, fall into this category [10].

An isoresistance diagram of the compositions in the system Ni-Fe- Mn oxides is given in Fig.5.10. The phases present at these compositions could be either spinel solid solutions or solid solutions of rock salt structure as determined in (Fig.5.11) [11] . Figure3.12 shows the relationships between the resistance of a thermistor at room temperature and the B value in the equation

$$R_T = A\,\{(B/T) + (C/T^2) + (D/T^3) + ...\} \quad (18)$$

For selected NTC (negative temperature coefficient of resistance) thermistor

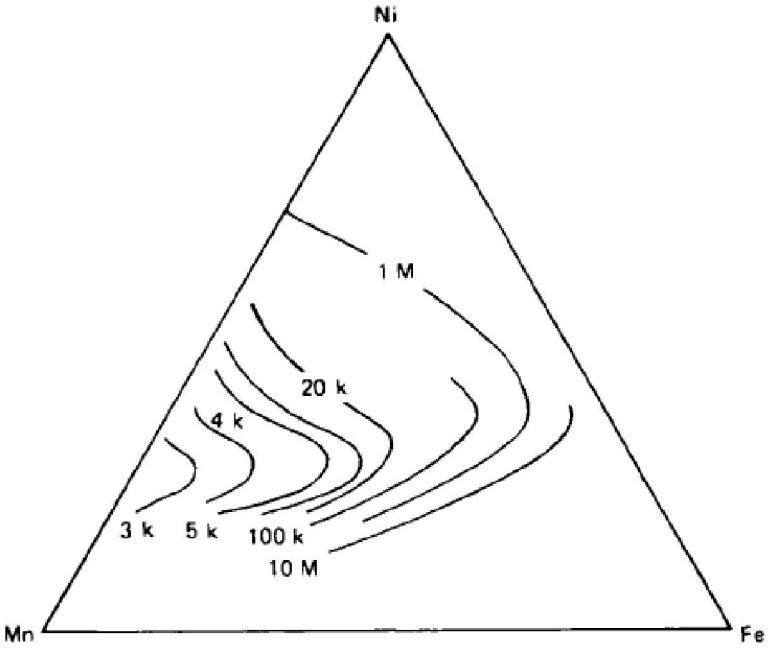

Fig.5.10. Iso-resistance curves of compositions in the system Mn-Ni-Fe oxides.

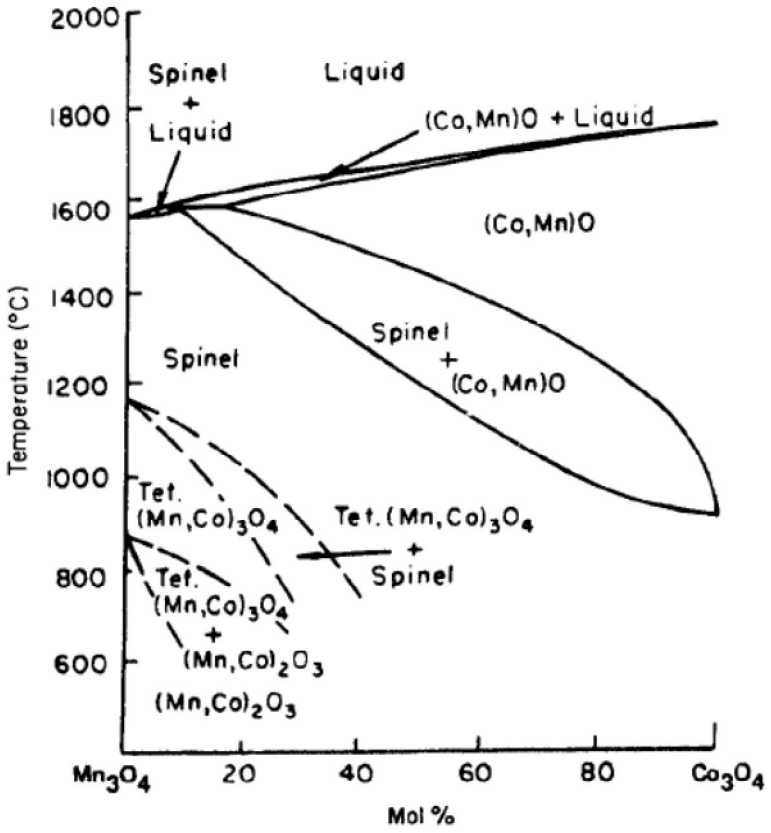

Fig.5.11. Phase relationships in the pseudo-binary system Mn_3O_4-Co_3O_4 [11].

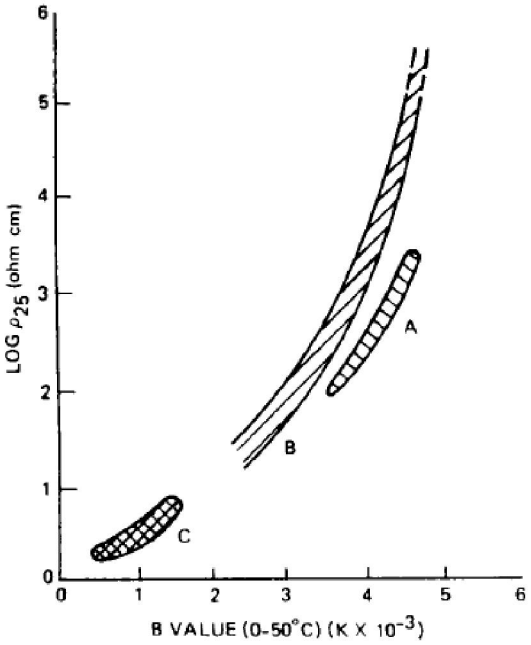

Fig.5.12. The relationships between resistivity and the s value as given in Equation 18 for selected NTC (negative temperature coefficient of resistance) thermistor materials classes; A, Li-doped (Mn, Ni, Co) oxides; B, complex spinels AB_2O_4, $(Ni, Mn)_3O_4$, $(Ni, Mn, Co)_3O_4$, $(Ni,Mn,Fe)_3O_4$; and C, hematite $(Fe,Ti)_2O_3$.

materials classes as specified in the caption [12].Extrinsic ionic conductors have also been used as thermistor materials for high-temperature applications. The conductivity of extrinsic ionic conductors does not change with oxygen pressure.

5.5.3.2. Extrinsic electronic conductors - surface effect

When the surface-to-bulk ratio of a semiconducting ceramic or thin film is high, the surface effect dominates the resistance. These devices can be used as gas sensors. Sensors detecting gas compositions are usually porous ceramics or thin films of extrinsic electronic semiconductors.

Surface layer-controlled gas sensors use the change in the concentration of conduction electrons as a result of chemical reactions at the surface. These reactions, chemisorption and/or catalytic reactions modify the defect states of the oxide surface layer to a depth of a few micrometers or less. The working temperature of this type of sensor is usually lower than that of the bulk conduction-based gas sensors, typically 300 - 800°C, depending on the base oxide and the target application [10].

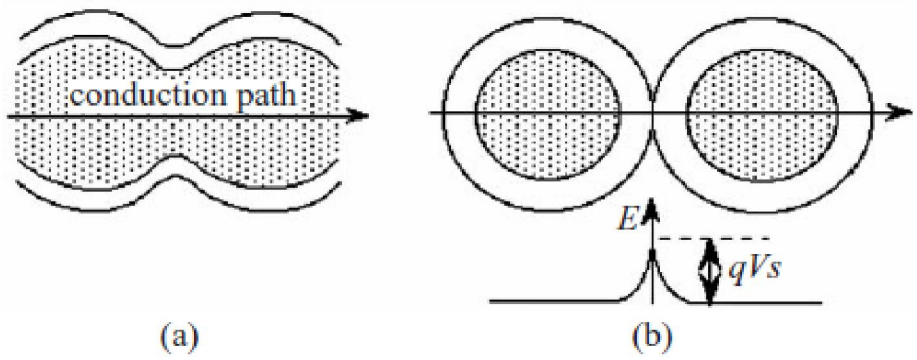

Fig.5.13. Models for surface layer-controlled gas sensing, showing two limiting cases: (a) continuous surface layer and (b) formation of a potential barrier (Schottky barrier) across the intergranular boundary.

The temperature should be low enough to allow sufficient surface adsorption and slow down the bulk defect equilibration processes, and high enough for catalysis reactions and charge transfer between the surface layer and the bulk interior.

Two distinct cases of the surface layer-controlled gas sensors are depicted in Fig.5.13. Both are characterized by a thin surface layer (a few atomic layers), and rely on the gas-solid reactions which change the trapping (space charge) density on the oxide surface or at the intergranular interface. They are different in whether the surface layer is continuous or forms a potential barrier across the intergranular boundary. It should be noted, however, that often such a distinction is more of a theoretical assumption for modeling rather than a clear conclusion supported by straightforward

experimental evidence. A gas sensor using the presence of the Schottky barrier at the grain boundaries (back-to-back Schottky barrier) typically consists of poorly sintered body, porous thin film, or thick film, where the grains are loosely in contact and the surface layer overlaps at the neck. Fig.5.14 illustrates this type of mechanism, using an n-type semiconducting oxide as an example.

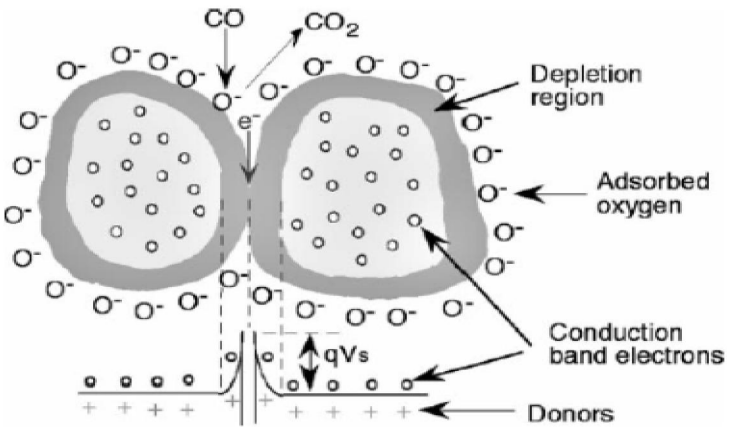

Fig.5.14.Compressed powder model illustrating CO sensing mechanism in an n-type oxide.

First, oxygen from the ambient adsorbs on the exposed surface of the grains, and, extracting an electron from the material, ionizes to O^- or O^{2-}; O^- is believed to be dominant [13]. This leads to the formation of a depletion region and the conduction is determined by the height of the barrier (qVs) at the intergranular contacts:

$$\sigma_s = \sigma_0 \exp(-qV_S / kT) \quad (19)$$

Where σ_s and σ_0 are the conductivity and pre-exponential constant, respectively. When exposed to a reducing gas such as CO, the adsorbed CO reacts with the adsorbed O^-, releasing the trapped electron back to the conduction band, subsequently lowering the barrier height and the resistance. At temperatures up to about 450°C, the characteristics of SnO_2 and ZnO based CO sensors have been reported to follow the

Schottky barrier-controlled conduction mechanism [14]. This effect has also been attributed to the sensing behavior of an anatase titania (TiO_2)-based CO sensor [15, 16].

Surface layer-controlled gas sensors are usually used for the monitoring of gas species other than oxygen [10].

For reducing gas sensors; Materials studied most extensively for these applications are extrinsic n-type semiconducting tin oxides and zinc oxides. Both of these semiconductors are non-stoichiometric compounds with frozen-in defects. Thin film and porous tin oxide and/or, for example, zinc oxide sensors have been developed by many investigators for CO and other reducing gas measurements. The resistance of a tin oxide sensor as a function of gas composition is shown in Fig.5.15. Windischmann and Mark (1979) [13] suggested that initially the film is depleted of electrons because of the adsorption of oxygen on the surface according to the reaction:

$$O_2\ (gas) + s \longrightarrow O_{2,ads}\ (20)$$

$$O_{2,ads} + e^- \longrightarrow O^-_{2,ads}\ (21)$$

Where s is an adsorption site on the surface. When small concentrations of CO are introduced in the surrounding gas, the following reactions take place on the surface:

$$CO\ (gas) + s' \longrightarrow CO_{ads} \qquad (22)$$

$$2CO_{ads} + O^-_{2,ads} \longrightarrow 2CO_{2,ads} + e^- + s \qquad (23)$$

$$2CO_{2,ads} \longrightarrow CO_2(gas) + s' \qquad (24)$$

As in Equation 22, as the electrons are returned to the bulk, the conductance of the film increases. Figure 5.15 shows performance curves of CO sensors. It should be noted that the resistance for each individual sensor is different and therefore calibration of each sensor is needed.

Tin oxide and zinc oxide sensors also respond to other reducing gaseous species, such as hydrocarbon molecules, identically as to CO. These sensors are not able to differentiate the gases in a mixture, as shown in Fig.5.16.

Therefore, selectivity is a serious problem in gas sensors of this type. There are several ways of improving the selectivity of gas sensors. The commonly used methods are (1) temperature control, and (2) catalysts on the surface of sensing elements. The temperature effect is due to the surface reaction between hydrocarbons and oxygen [17]. For hydrocarbon molecules (RH_2) absorbed on the sensor surface, the reaction between the hydrocarbon molecules and the surface oxygen is

$$RH_2 + 2O^- \rightarrow RO + H_2O + 2e^- \qquad (25)$$

The rate of this reaction is a function of temperature. When a sensor is operated at low temperatures, the reaction will be slow. When the sensor is operated at higher temperatures, the reaction occurs so rapidly that the sensor is not able to detect the combustion reaction; therefore there will be a maximum in the sensitivity vs temperature curve. As the reaction rates for the various gases are different, the maximum for each gas occurs at a different temperature. An example is shown in Fig.5.17.

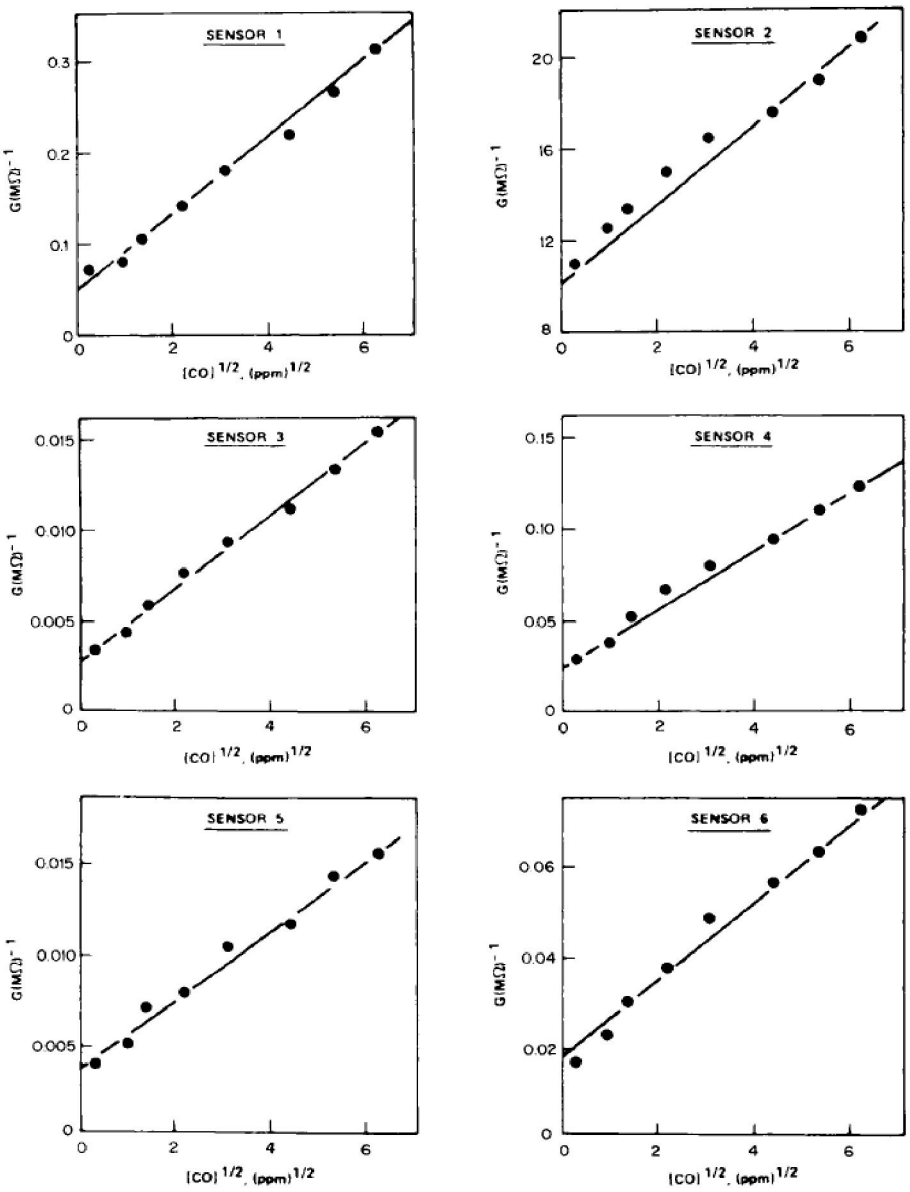

Fig.5.15. The sensitivity of a tin oxide sensor to CO concentrations [13].

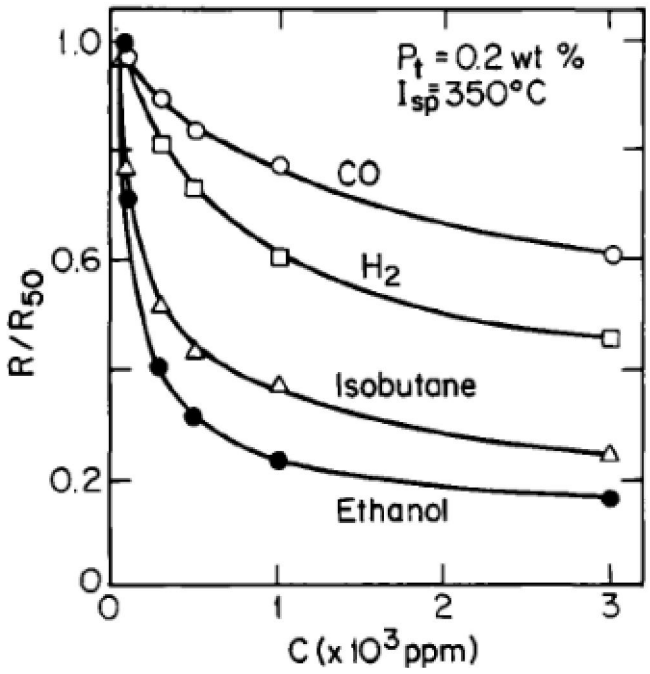

Fig.5.16. the sensitivity of tin oxide gas sensors to different gases [18] Polycrystalline SnO_x sensor with a Pt catalyst.

Figure 5.18.illustrates the effects of catalysis on the selectivity of a semiconducting polycrystalline tin oxide gas sensor [19]. It shows that the use of a platinum catalyst is very effective on the selectivity of a SnO_x sensor.

The sensitivity of SnO_x sensors varies with different catalysts and different sensor shapes [18]. A polycrystalline SnO_x sensor with platinum catalysts (Fig.5.18) has a low selectivity, while a thin-film sensor containing palladium (Fig.5.19) has a very high selectivity for ethanol. Figure 5.20 shows the behavior of a thick-film sensor containing palladium.

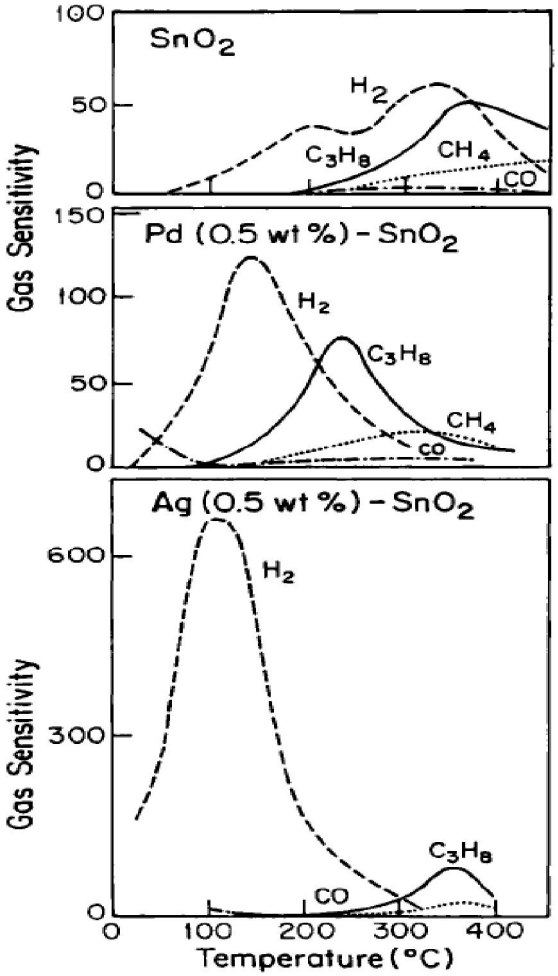

Fig.5.17. The temperature dependence of gas sensitivities of different tin oxide sensors to different gases [18].

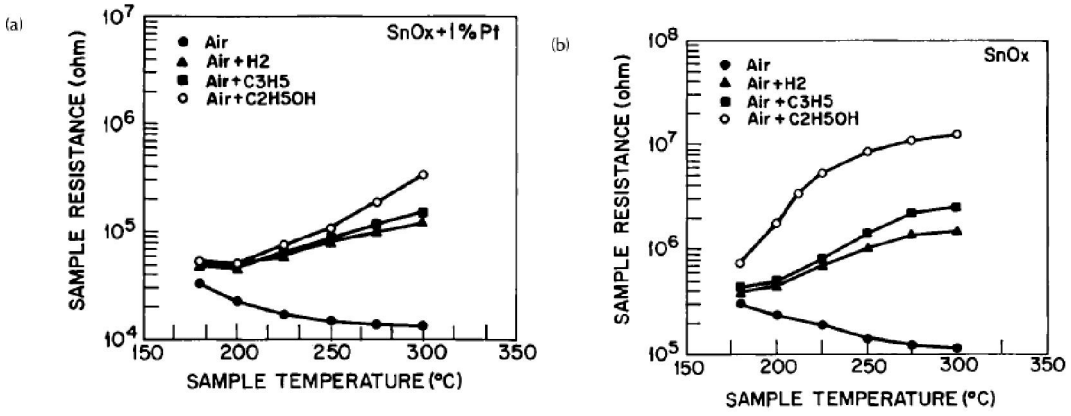

Fig.5.18. The catalytic effect on tin oxide gas sensors [19] (a) Sensor with a Pt catalyst; (b) sensor without catalyst.

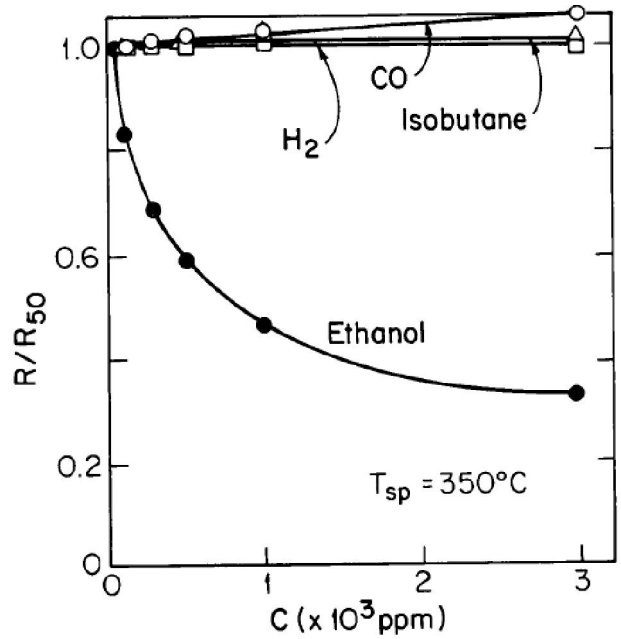

Fig.5.19. The sensitivity to different gases of tin oxide gas sensors [18].Thin-film SnO_x sensor with a Pt catalyst.

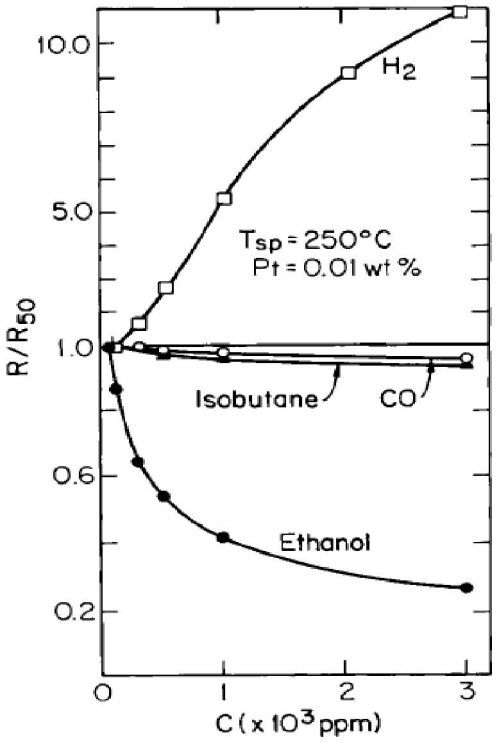

Fig.5.20. The sensitivity of tin oxide gas sensors to different gases [18]. Thick-film SnO_x sensor with Pd catalyst.

5.6. Humidity sensors

The best-known humidity sensor is a p-type semiconducting $MgCr_2O_4$-TiO_2 (Nitta et al, 1980). This sensor operates as follows. On the surface, water molecules dissociate into protons and hydroxyl groups. The hydroxyl groups combine with the surface oxygen ions forming water and the protons become positive charge carriers, hence the conductance of the p-type semiconductor increases in air of higher humidity. The sensor characteristics are given in Fig.5.21 Phase relationships in the system $MgOCr_2O_3$ - TiO_2 [20]. 31 mol% TiO_2 forms solid solutions in $MgCr_2O_4$ spinel. It is very possible that the spinel has a formula $(Mg_6V_{Mg_2})\ (Cr_4^{2+} + Cr_8^{3+} + Ti_4^{4+})O_4$, which is a mixed-valency semiconductor.

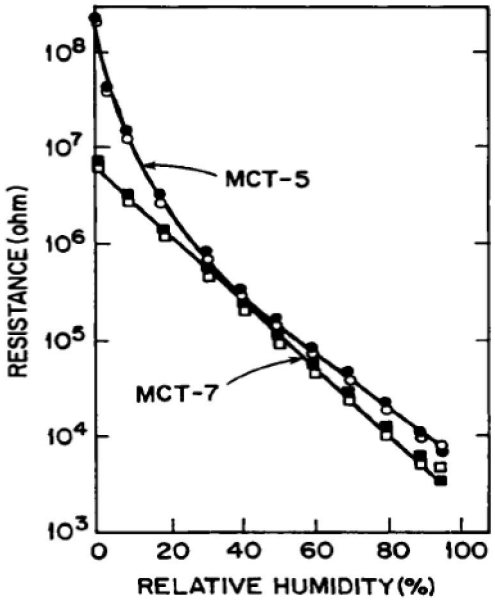

Fig.5.21. Humidity-resistance characteristics of two $MgCr_2O_4$-TiO_2 sensors [21].

Extrinsic electronic conductors - boundary effect

Polycrystalline $BaTiO_3$ doped with rare-earth oxides, Ln_2O_3, is a mixed-valency $(Ba_{1-x}^{2+}Ln_x^{3+})\ \ (Ti_{1-x}^{4+}Ti_x^{3+})O_3$ semiconductor [22]. The resistivity of these ceramics exhibits typical extrinsic n-type semiconductor characteristics.

The resistance of these materials increases by several orders of magnitude at 120°C for $BaTiO_3$, as shown in Fig.5.22 (PTCR, positive temperature coefficient of resistance). The change of resistance in $BaTiO_3$-$SrTiO_3$ and $BaTiO_3$-$PbTiO_3$ solid solutions coincides with the ferroelectric Curie temperatures of these compositions [23]. The resistance-temperature anomaly (PTCR) at the Curie temperature does not occur in fully reduced polycrystalline materials [24].

Goodman (1963) [25] demonstrated that this anomaly is not observed in a doped single crystal, whereas a polycrystalline specimen prepared from the same single crystal does exhibit the PTCR anomaly. These investigations indicated that the doped polycrystalline $BaTiO_3$ which exhibits the PTCR anomaly is a two-component system consisting of conducting grains and intergranular regions of lower conductivity. The difference in conductivity gives rise to large field effects at the intergranular region which, when coupled with the temperature dependence of the high-field dielectric constant, lead to the onset of anomalous conduction at the Curie temperature [26].

5.7. Concluding Remarks

We have discussed the principles and practices of sensor designs and applications utilizing the electrical conductivity of ceramic materials. It should be mentioned that all of these presentations are based on ideal conditions, i.e. (1) equilibrium within solid, between solid-gas and gas-gas phases was reached during operation when non-stoichiometric compounds were involved; (2) no reaction took place within the solid phase when extrinsic conductors were used. However, in order to obtain these ideal conditions, there are many important factors which have to be considered. The following are just a few examples.

5.7.1. Microstructure of ceramics

For TiO_2 sensors the sensing elements should be porous, allowing a large solid-gas contact area. Sensing elements should be fine grained to allow valency change of the titanium ions to take place in the shortest possible time.

Sensors using extrinsic semiconductors, mixed-valency compounds and/or semiconductors with frozen-in defects should be dense to avoid the oxidation reduction reactions taking place within the solid. Tin oxide gas sensors should have a high surface-to-bulk ratio to maximize the surface effect on the electrical resistance of the devices.

5.7.2. Catalysis

Catalysts affect sensor sensitivity and selectivity of gas sensors. For equilibrium gas sensors (equilibrium oxygen sensors), catalysts can induce gas-gas and gas-solid reactions to occur at lower temperatures. The efficiency of catalysts depends on composition as well as on microstructure.

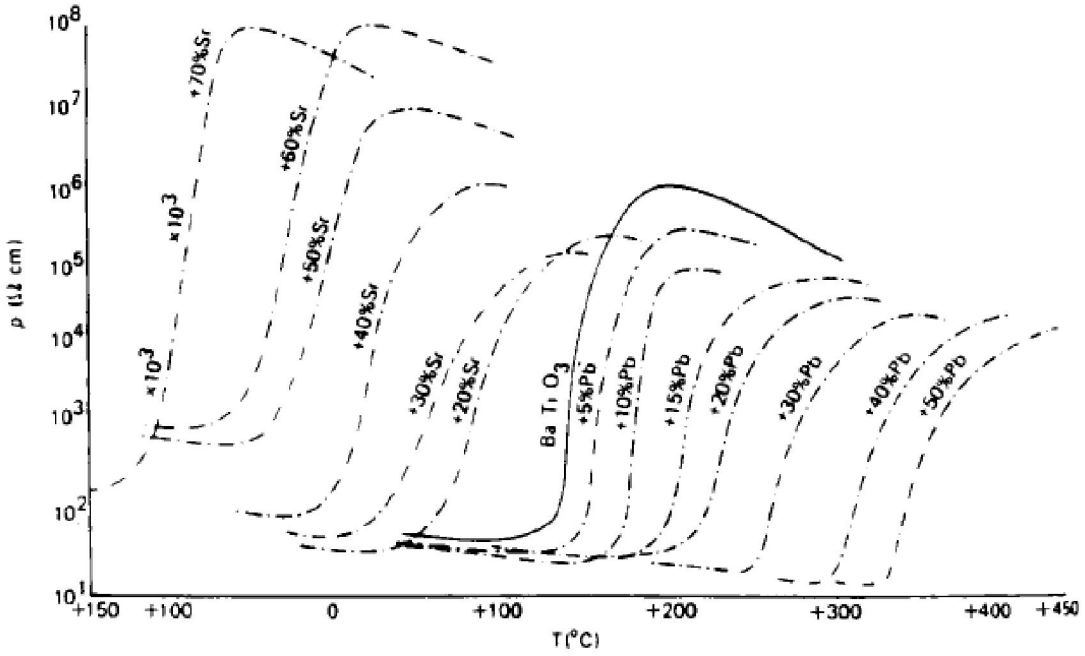

Fig.5.22. Resistivity-temperature curves for $BaTiO_3$ PTCR thermistors containing isovalent substitutions for barium. The solid line represents $BaTiO_3$ and dashed lines show the effect of strontium (shift to the left) and lead (shift to the right) substitution in the proportions indicated [22].

5.8. Motivation of using glass ceramic as gas sensor

The base materials most widely used for ceramic gas sensors are transition metal oxides. A change in their electrical conductivity is typically exploited in the sensing measurements. Oxides such as ZnO, TiO_2, and SnO_2 are the most widely investigated ones. They not only have been adopted as model systems for fundamental studies, but also as base materials for the development of various sensors for the detection of gases such as H_2, CO, NO_x, CO_2, CH_4, and other hydrocarbons.

The fact that a single oxide like SnO_2 can be used as a base material for the detection of a variety of gases seems to suggest an unlimited potential for oxide based gas sensors. There are, however, at least two issues, selectivity (or cross-sensitivity) and stability (or aging), which have limited their applications and further development. Poor selectivity toward the target gas or cross-sensitivity toward other gases makes the output of a sensor unreliable. In addition, aging or poor stability causes the response of a sensor to drift with time. There is a considerable effort directed at resolving the selectivity issue. Two commonly adopted approaches for improving selectivity are: (a) addition of suitable catalysts and/or dopants, and (b) selection of an optimum operation temperature. Other approaches include the:

(1) development of new base oxides other than the traditional oxides such as SnO_2 and TiO_2; (2) use of impedance (frequency modulation) instead of DC resistance measurements; (3) use of filtration membrane or multilayer sensors for selective

adsorption or reaction; and (4) use of arrays of partially sensitive sensors in conjunction with pattern recognition and multicomponent analysis [27].

In contrast to the selectivity issue, the problem of stability is rarely addressed in the literature. This does not mean that the stability issue has less impact on the usefulness of a gas sensor. It is rather an engineering issue often addressed at the prototyping and manufacturing stages, and is difficult to resolve mostly owing to lack of precise knowledge of the underlying physical and chemical processes [10].

Percolated conductive fillers in an insulating matrix have attracted tremendous interest for a long time, due to the electromechanical interactions between the various phases [28]. In general, conductor–insulator composites consist of glass, ceramic, or polymer as an insulating phase and of metal or carbon as conducting phase.

So, interactions between the matrix and the conductive phase have a large influence on the formation of the percolated network.

The conductivity of such composites drastically increases at a certain conductive filler concentration. This phenomenon is based on the formation of conducting strains in the insulating matrix potentially disconnected by gaps [29].

Many parameters influence the percolation: the concentration, the filler distribution, the filler shape, and the filler–matrix interactions and of course the synthesis method. Percolated network above sinter temperatures of the glass transition temperature also could help. In order to have sufficient diffused filler inside the matrix to reach the desired percolation network, it is necessary:

1- To check the phase separation.
2- To check from the literature, the formed phases conductivity and their electrical behavior.

3- To try a sample below and above the glass transition temperature and to look at them by means of SEM (to find the percolation difference).
4- To measure the conductivity of the different prepared materials and to check if they are conductive; near to metal conductivity or not?
5- To measure the relative density of the prepared materials.

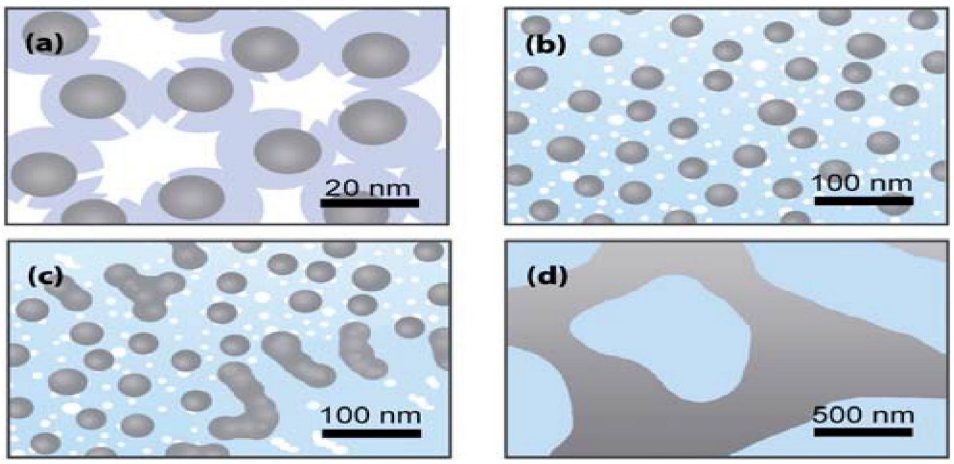

Fig.5.21. Sketch of the formation of a percolated metal/conductive filler network by heat treatment [29].

Glass or ceramic materials as the sensitive material are based on the variation of their electrical properties, such as impedance or capacitance. For sensors with thick film glass it is important to control the microstructure and hence, sensor sensitivity, crystal growth onto the glass amorphous surface conditions.

Crystal growth structure depends on firing temperature, submersion time (time consumed for immersing glass into deioized water allowing small crystals to grow on the glass surface forming the sensitive layer) which determines crystal size and, to a smaller extent, on the thickness of glass film [30].

5.9. Experimental Work: Crystallization of zinc oxide by melt quenching technique

5.9.1. Material and Methods

The idea is to check the possibility to fabricate ZnO crystals within a glass matrix by means of crystallization process.

For that purpose, we quenched a melt with nominal composition 58% ZnO 33.3% B_2O_3 4% WO_3 4% Bi_2O_3. The chosen glass sample was then subjected to the heat treatment for 15 hours at the temperature close to the established T_x.

5.9.1.1. Precursors

The starting materials for preparation of mixtures are: zinc oxide (ZnO - Aldrich > 99 %), bismuth oxide (Bi_2O_3 - Alfa Aesar, 99.999% metal basis), tungsten oxide (WO_3 - Aldrich > 99 %, particle size below 100 nm) and boric acid (H_3BO_3 - Alfa Aesar, 99.999% metal basis).

5.9.1.1. Preparation of material and methods

1 - Select the compositions of each batch from the triangle which is presented as a mole ratio of oxides (figure 5.22).

Mol% and weight% can be calculated by the following equation:

$$\mathbf{x_A = (X_A.M_A / X_A.M_A + X_B.M_B) * 100\%}$$

Where: $\mathbf{x}$ **(wt%)** …; **X (mol%)** is known from triangle or table; **M** is (Molecular mass)

*ZnO is used as ZnO.

*WO_3 is used as WO_3.

*Bi_2O_3 is used as Bi_2O_3.

*B_2O_3 is used as H_3BO_3 (boric acid) due to this reaction: $2H_3BO_3 \rightarrow B_2O_3 + 3H_2O$.

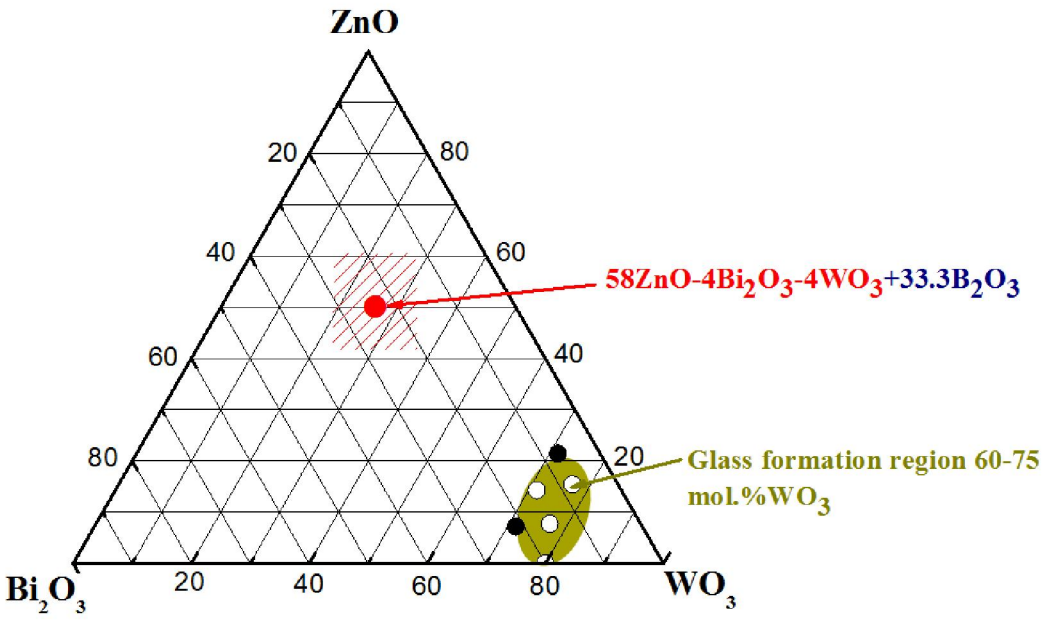

Fig.5.22. Triangle of ZnO-Bi_2O_3-WO_3 system [31], Where (○) glasses and (●) crystals, (●) 58ZnO-4Bi_2O_3-4WO_3-33.3B_2O_3

2 - Calculating the bismuth oxide amounts, boric acid, Zinc oxide and Tungsten oxide for 10 g batch.

3 - Mixing and milling of the components in the Agate mortar (10 min) until good homogenization in order to prepare the batch.

4 - Transferring the homogenized batch in a suitable crucible.

5 - Heating in the electric furnace for 5 - 10 minutes at the temperature of 1300^{0}C depending on the liquid temperature in each binary system.

During heating and melting, the following reactions in the raw materials may occur:

- Release of adsorbed moisture around 100^{o}C;
- Organics burn around 440^{o}C;
- Evolution of gases;
- Solid-state reactions between the various oxides;
- Appearance of the eutectic liquid;

- Increase rate of reaction to form a molten mass;
- Evaporation of volatiles components from the melts;
- Gradual removal of bubbles;
- Homogenization of the melt;
- Reaction with the container throughout the melting period.

6 - Pouring the melt on the metal plate in order to be quenched with a rate of 10^2-10^3K/s.

7- Preparing nanomaterials based on ZnO by:

- Thermal treatment in the electric furnace at 500^0C for 15 h.

5.9.2. Physico-chemical data for the ternary system

5.9.2.1. Binary system Bi_2O_3-ZnO

The phase diagram of binary Bi_2O_3-ZnO system is constructed by Guna et al [32] (Fig.5.23).

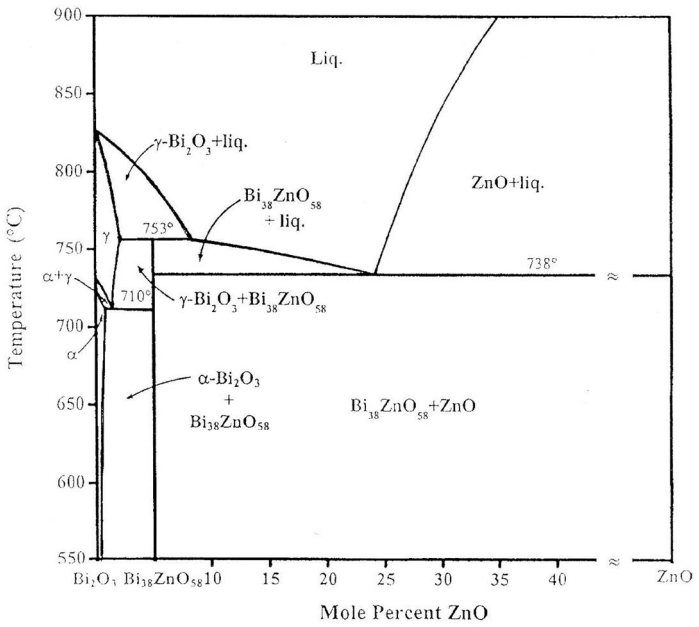

Fig.5.23. Phase diagram of the binary Bi_2O_3-ZnO system (α=low-temperature monoclinic Bi_2O_3, γ= body-centered-cubic solid solution, liq=liquid) [32]

The authors reveal that incorporation of a small amount of ZnO into the high-temperature face-centered-cubic lattice of Bi_2O_3 (δ-Bi_2O_3) gives rise to the formation of a body-centered-cubic solid solution (γ-Bi_2O_3). The maximum solid solubility of ZnO in Bi_2O_3 occurs at a temperature near 750ºC and is limited to a composition of 2.2% ZnO. On cooling, the γ-Bi_2O_3 solid solution undergoes a eutectoid transformation at a temperature near 710ºC to yield the low-temperature monoclinic polymorph of Bi_2O_3 (α-Bi_2O_3) and $Bi_{38}ZnO_{58}$. The eutectoid occurs in the Bi_2O_3-rich region of the Bi_2O_3-ZnO system at a composition near 1.8 mol% ZnO. The compound $Bi_{38}ZnO_{58}$ has a crystal structure analogous to that of the b.c.c-based γ-Bi_2O_3 solid solution and melts incongruently at 753±2ºC to yield γ-Bi_2O_3 and liquid. A binary eutectic between $Bi_{38}ZnO_{58}$ and ZnO occurs at a composition of 25 ± 1.0 mol% ZnO with a melting temperature of 738 ± 2ºC [32, 33].

The glass formation region in the binary Bi_2O_3-ZnO is not investigated.

5.9.2.2. Binary system Bi_2O_3-WO_3

The phase relations in the Bi_2O_3-WO_3 system are described by Speranskaya [34] (Fig.5.24). It is established the formation of five compounds with the compositions: Bi_6WO_{12} (congruently melts at 1040°C); Bi_2WO_6 (congruently melts at 1070°-1080°C); $Bi_2W_2O_9$ (decomposes at 880ºC); Bi_4WO_9 and $Bi_{12}WO_{21}$, existing under subsolidus line, decompose at 770 and 875°C respectively. There is also one

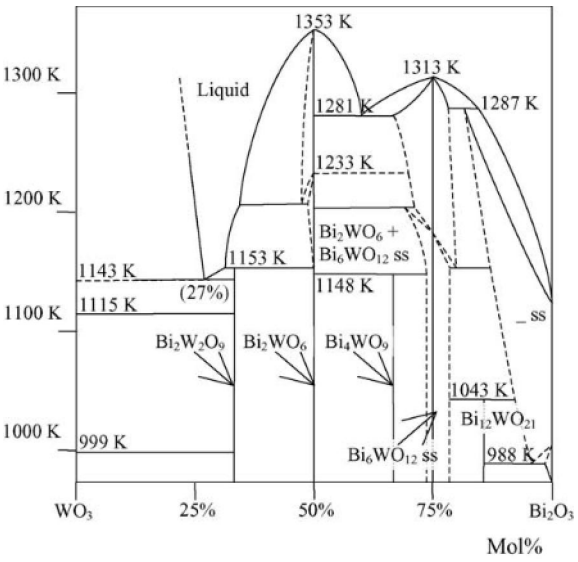

Fig.5.24. Phase diagram of Bi_2O_3-WO_3 system [8]

solid solution region in the Bi_2O_3 rich area based on β-Bi_2O_3. On the phase diagram one eutectic point could be seen containing 27 mol% Bi_2O_3 with melting temperature of 870°C.

According to the phase diagram proposed by Hoda and Chang [35] and as well as the subsequent studies [36, 37] three compounds were found in the Bi_2O_3-WO_3 system: Bi_2WO_6 (50 mol% WO_3); $Bi_2W_2O_9$ (66.67 mol%) and $Bi_{14}WO_{24}$ (12.5 mol% WO_3) and another intermediate phase $Bi_7WO_{13.5}$ (22.22 mol% WO_3) which forms a solid solution. A recent phase equilibrium study of Watanabe et al. [38] revealed that $Bi_7WO_{13.5}$ phase exists stably above 670ºC. Below 670ºC $Bi_7WO_{13.5}$ decomposes sluggishly to yield a mixture of a bismuth-rich limit of the solid solution and a small quantity of $Bi_{14}WO_{24}$. The stable solid-solubility region expands from 20 to 27 mol% WO_3 at 850ºC and from 23 to 25.5 mol% WO_3 below 500ºC. The same author identified three stable polymorphs in $Bi_{14}WO_{24}$ [39]. On heating the low-temperature monoclinic form changes to the intermediate orthorhombic form around 40ºC, and the intermediate form changes to the high-temperature face-centered cubic (fcc) form at 780ºC. Both transitions are reversible. The 40ºC transition is displacive and the 780ºC transition is reconstructive.

The literature data on the crystalline phases present in the binary system Bi_2O_3-WO_3 show that the Bi_2WO_6 possesses Aurivillius-type structure consisting of alternating $(Bi_2O_2)_n^{2n+}$ layers and perovskite-like $(WO_4)_n^{2n-}$ layers build up of WO_6 octahedra (Fig 3.25). The $(Bi_2O_2)_n^{2n+}$ layers are made of a square planar net of oxygen anions with the Bi^{3+} cations alternatively above and below the plane and can be described as forming caps of the BiO_4 square pyramids [40,41].

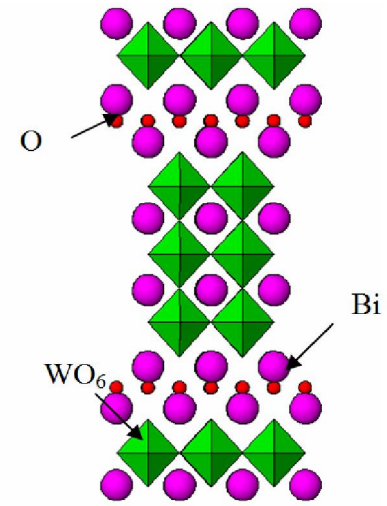

Fig.5.25. Structure of Bi_2WO_6

$Bi_2W_2O_9$ compound belongs to the family of layered bismuth compounds with the chemical formula $(Bi_2O_2)^{2+}$ $(A_{n-1}B_nO3_{n-1})^{2-}$ [42, 43]. X-ray diffraction and high resolution electron microscopy have proved that $Bi_2W_2O_9$ has a structure consisting of alternate stacking of Bi_2O_2 layer and a deformed ReO_3 type W_2O_7 sheet which contains two corner linked WO_6 octahedral units (Fig.5.26) [44].

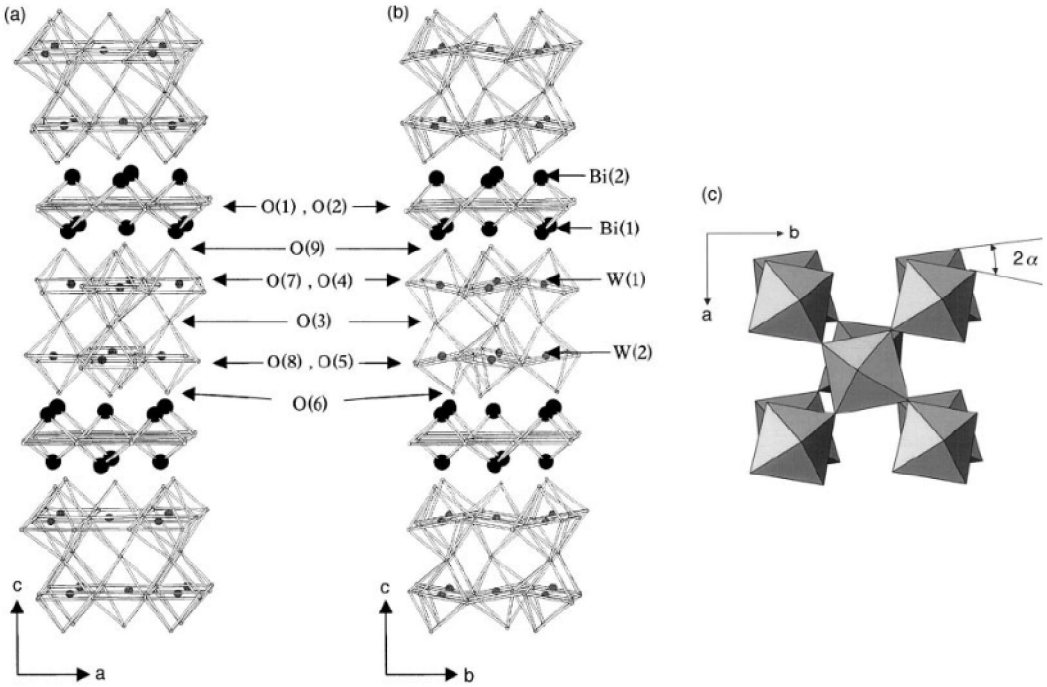

Fig.5.26. Spatial views of the $Bi_2W_2O_9$ structure along (a) the b axis, (b) the an axis and (c) the c axis. [44]

The refined structural parameters of $Bi_2W_2O_9$ show the presence of a short W-O (0.172 nm) bond which, by analogy with WO_3 can be indicated as a double bond. Bi atoms are surrounded by eight oxygen atoms forming the distorted square antiprisms BiO_8 [44].

Glass formation in the binary Bi_2O_3-WO_3 system has been investigated previously [31]. Glasses are obtained in a narrow compositional range (60-75 mol% WO_3), at high cooling rates (10^4-10^5 K/s), applying roller quenching technique. Infrared spectral data revealed the formation of WO_6 (940 cm^{-1}, ν(W=O); 850, 800, 760 cm^{-1} ν(W-O-W)) and WO_4 (800-740 cm^{-1} $\nu_3(WO_4)$) structural units building up the amorphous network.

5.9.2.3. Binary system ZnO-WO_3

Phase diagram of ZnO-WO_3 system is shown in (Fig.5.27) [45]. As it is seen from the figure, one binary phase exists in the system- $ZnWO_4$ congruently melting at 1200°C. Two invariant points are established, containing 56 mol% ZnO (melting temperature at 1182°C) and 34 mol% ZnO (melting temperature at 1090°C) respectively. Solid solutions of both ZnO and WO_3 in $ZnWO_4$ are also formed from 900°C to 1160°C, above which melting occurs.

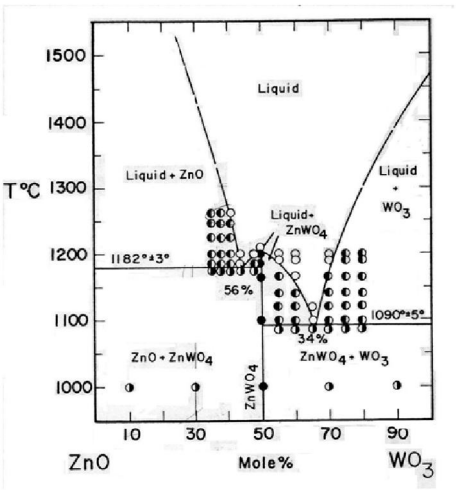

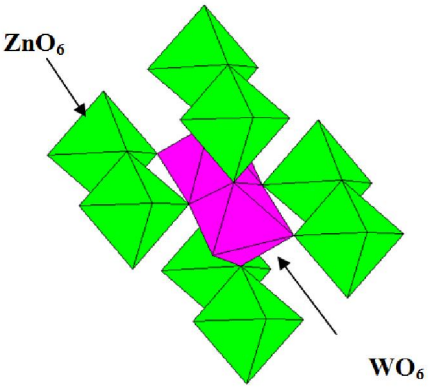

Fig.5.27 Phase diagram of the system ZnO-WO_3 [45] *Fig.5.28 Structure of $ZnWO_4$*

$ZnWO_4$ has wolframite-type structure (Fig.5.28) [46]. Tungsten and zinc atoms are within highly distorted octahedra of oxygen atoms. Two oxygen atoms of each octahedron are shared by adjacent octahedra, resulting in a chain-type structure. The chains of octahedra are in zig-zag array.

There is no data concerning the glass formation tendency in the ZnO-WO_3 system.

5.9. 3. Characterizations

Differential Thermal Analysis, In order to check the nearest glass to be as an amorphous precursor guide, the thermal characteristic of glass composition $70ZnO.5WO_3.5Bi_2O_3.20B_2O_3$ was examined by DTA (Fig.5.29). Taking into account the estimated crystallization onset of glass T_x=538ºC, the chosen glass sample was subjected to the heat treatment for 15 hours at the temperature near to the established T_x (500ºC).

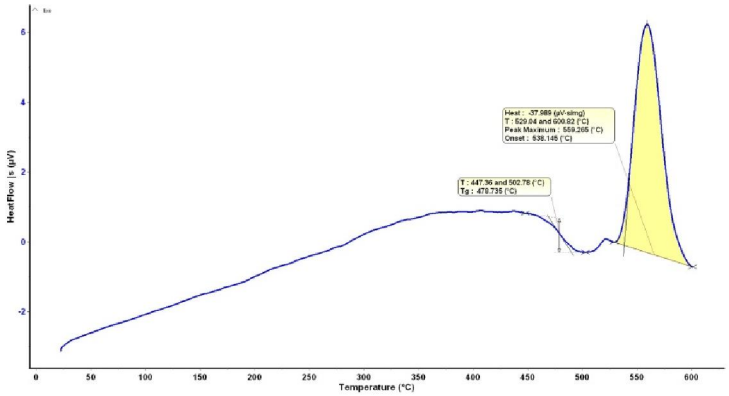

Fig.5.29. DTA curve of glass with nominal composition $70ZnO.5WO_3.5Bi_2O_3.20B_2O_3$

XRD diffraction, The formation of two different crystal phases: ZnO (JCPDS 89-0511) and Bi_2WO_6 (JCPDS 73-2020) has been observed (Fig.5.30). ZnO looks as the primary crystalline phase.

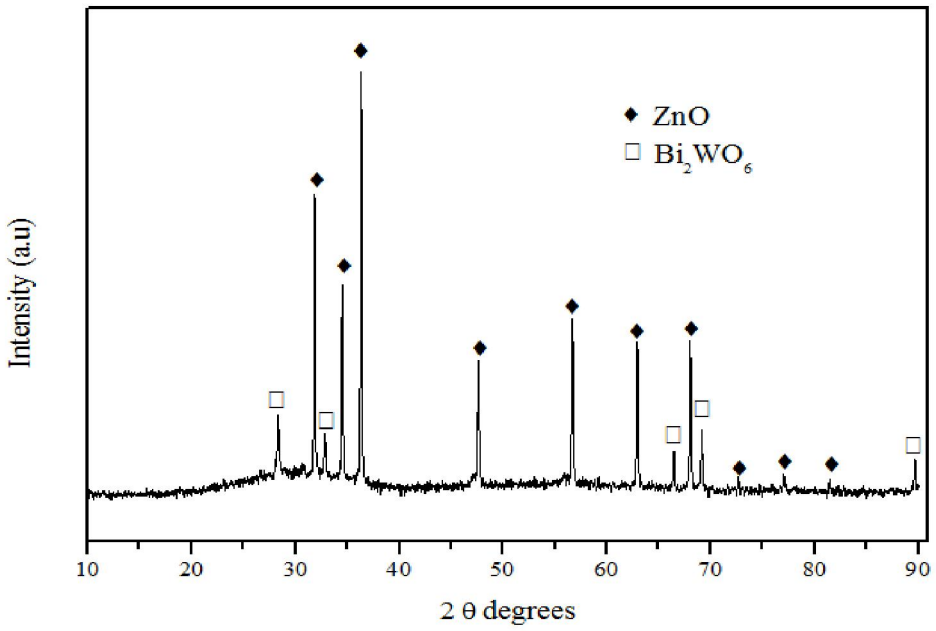

Fig.5.30. XRD pattern of glass with nominal composition $58ZnO.4WO_3.4Bi_2O_3.33.4B_2O_3$ heat treated at 500ºC for 15 hours.

SEM/FESEM observations and elemental microanalysis

FE-SEM observations, showed the presence of a glass matrix where particles with different size and shape are embedded.

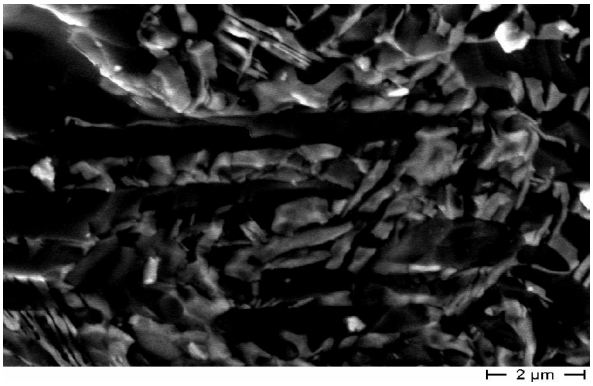

Fig.5.31. FE-SEM micrograph of as prepared glass ceramic x 10000

EDS analysis, has been done on different points along the crysals (Fig.5.31) and the matrix. It confirmed the presence of Zn, W, and Bi atoms. In addition, it revealed the presence of Zn along the crystals and the matrix; with slightly more percentage along the crystals (Fig.5.32).

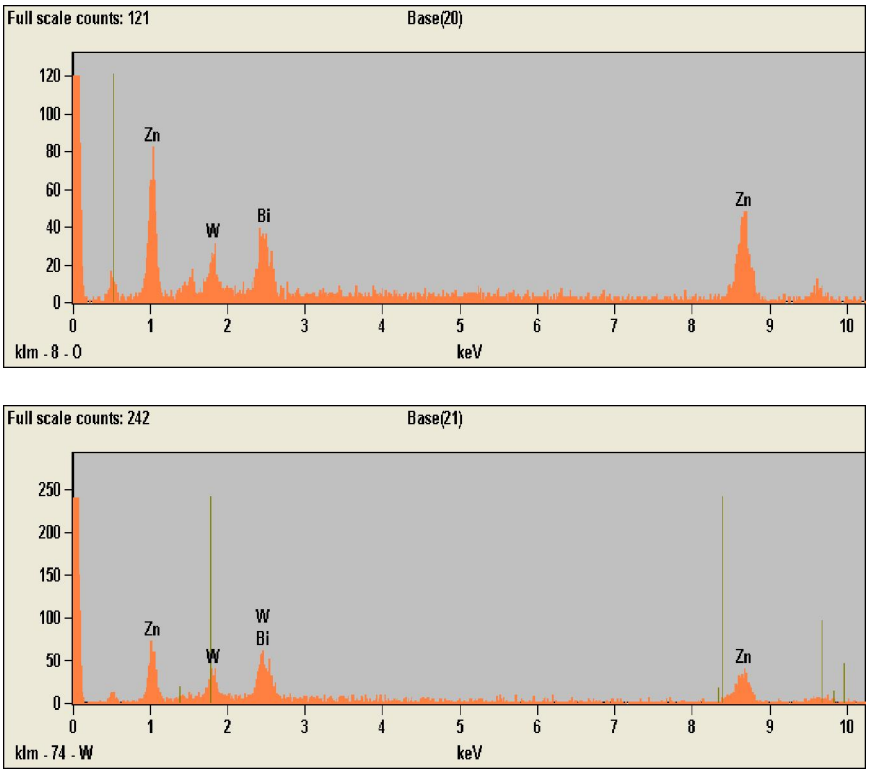

EDS results of the glass ceramic as - prepared material

	At. %	
Element	Crystal	Matrix
Zn	84.94	79.94
W	0.85	3.35
Bi	14.21	16.71

Fig.5.32. EDS results of the glass ceramic as prepared material

5.9.4. NO_2 sensitivity measurements

As prepared glass ceramic (GC) samples have been prepared as mentioned above (section 1) then the ink was prepared by adding 2- propanediol and was mixed in a mortar till getting an acceptable viscous paste. The ink has been screen printed over an alumina substrate onto Pt electrodes.

Fig.5.33.Screen-printed GC sample onto alumina substrate contains Pt electrode.

The prepared samples were fired at 550ºC for 1 h and, then tested by DC resistance measurements with gas mixing system under different concentrations of an oxidizing (NO_2 1, 2.5, 5 ppm) and a reducing gas (H_2 20, 50, 100 ppm) in a dry and humid air (50%) for 24 hours at different temperatures 150 and 250ºC. The detailed pulse program is illustrated in chapter one table 6.

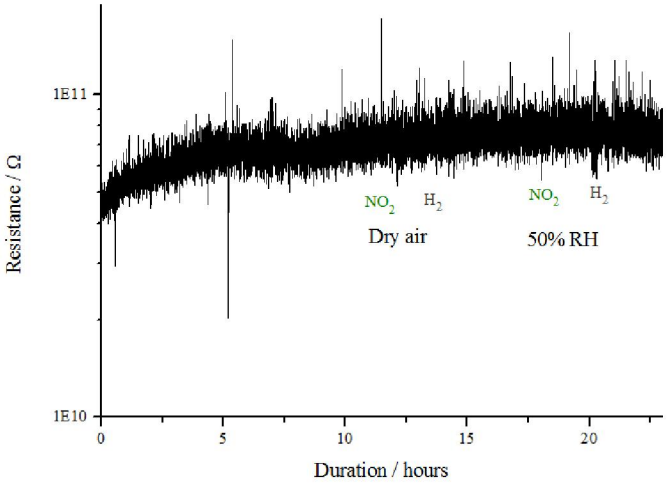

Fig.5.34. Response curve of glass-ceramic at 250ºC

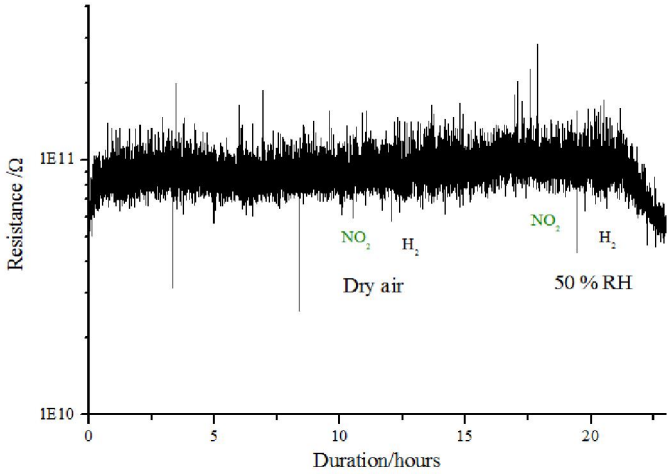

Fig.5.35. Response curve of glass-ceramic at 150ºC

From the response curves of the glass-ceramic, we could observe that there isn't any response to the targeted gases. On the contrary, there is too much noise and the sensors present very high resistances ~ 100 GΩ (fig.5.34, 35).

In order to improve the adhesion and to decrease the resistance of the screen printed sensors, a sol-gel phase based on ZnO has been added to as prepared glass ceramic sample as follows; 200 mg of zinc acetate dihydrate was dissolved in 0.625 cm^3 ethanol, and subsequently 0.066 mL monoethanolamine (MEA) were added under

stirring. After 30 minutes, 0.625 mL of EMFLOW (mixed Terpinols) were added after 5 more minutes of stirring, 70 wt% of liquid was added to the as prepared glass ceramic powder. Then, the paste was screen printed over an alumina substrate onto Pt electrodes.

FE-SEM observations have been done for the sol-gel glass ceramic film fig.5.36.

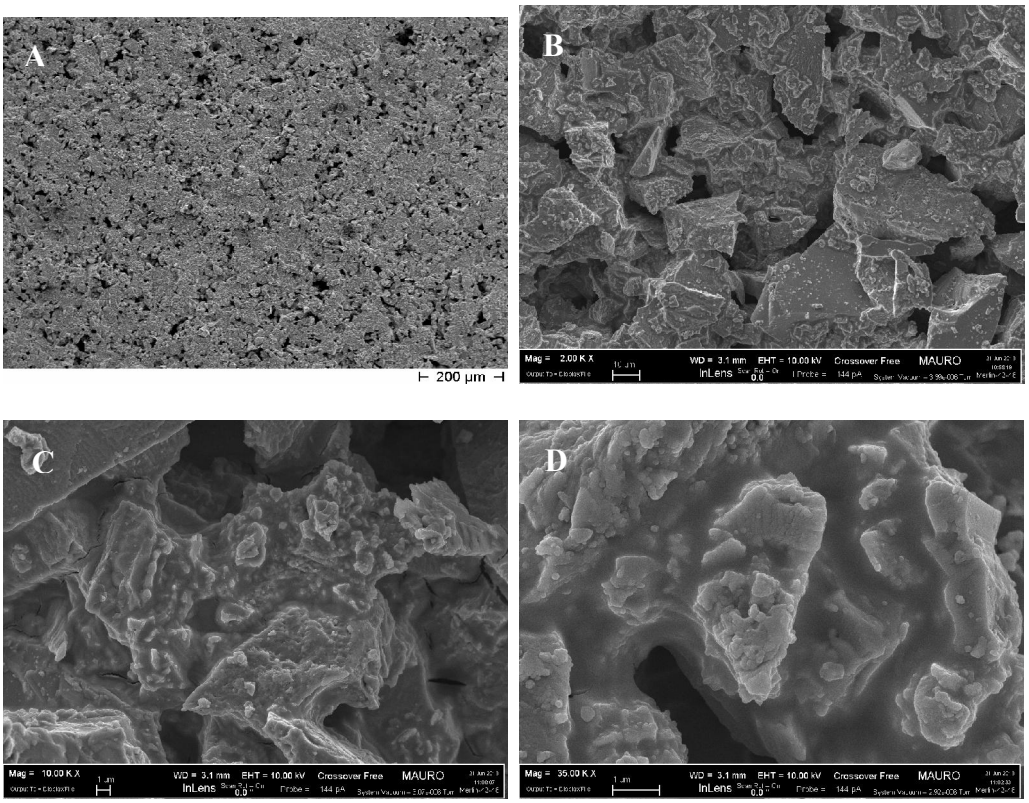

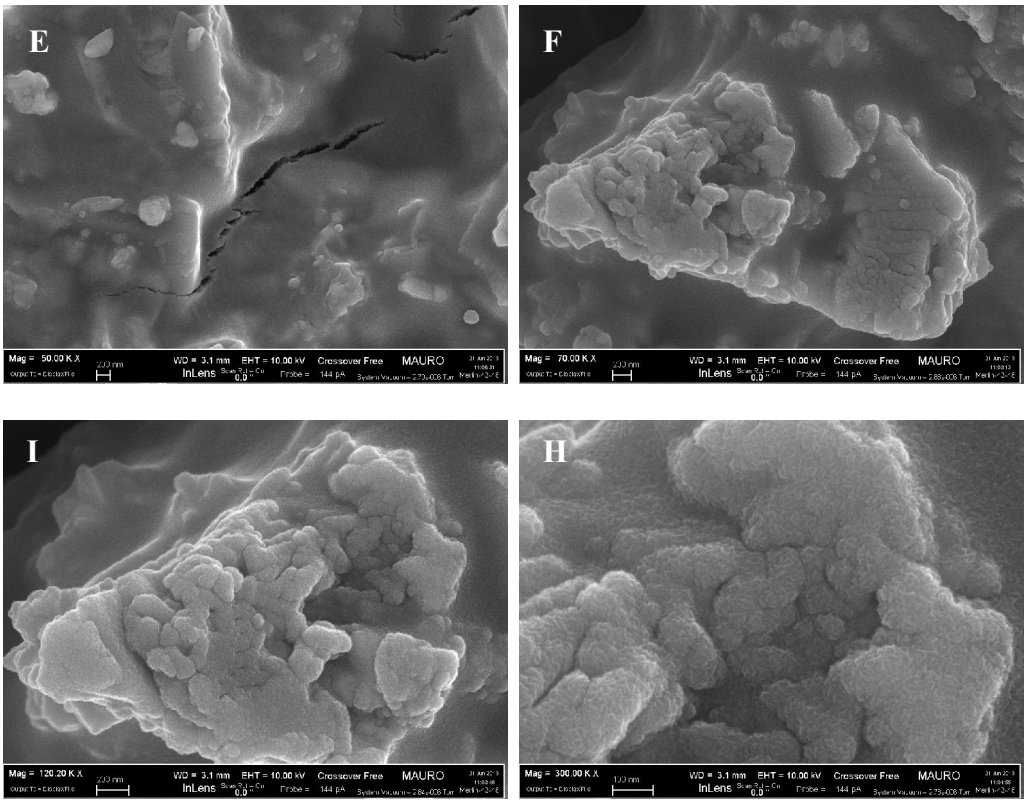

Fig.5.36.FE-SEM micrographs of sol-gel glass ceramic thick film

A well distributed porous film has been observed see fig.5.36- b. Also, we could investigate the presence of three phases; amorphous phase (matrix), crystalline phase (mostly ZnO) and a base from sol-gel phase which appears with some cracks more clearly at fig.5.36- E. Nucleation from the amorphous phase could be observed from fig.5.36- F,I,H.

The prepared samples were fired at 550ºC for 1 h then tested by DC resistance measurements with gas mixing system under different concentrations of an oxidizing (NO_2, 1, 2.5, 5 ppm) and a reducing gas (H_2, 20, 50, 100 ppm) in a dry and humid air (50%) for 24 hours at different temperatures 150, 200 and 250ºC.

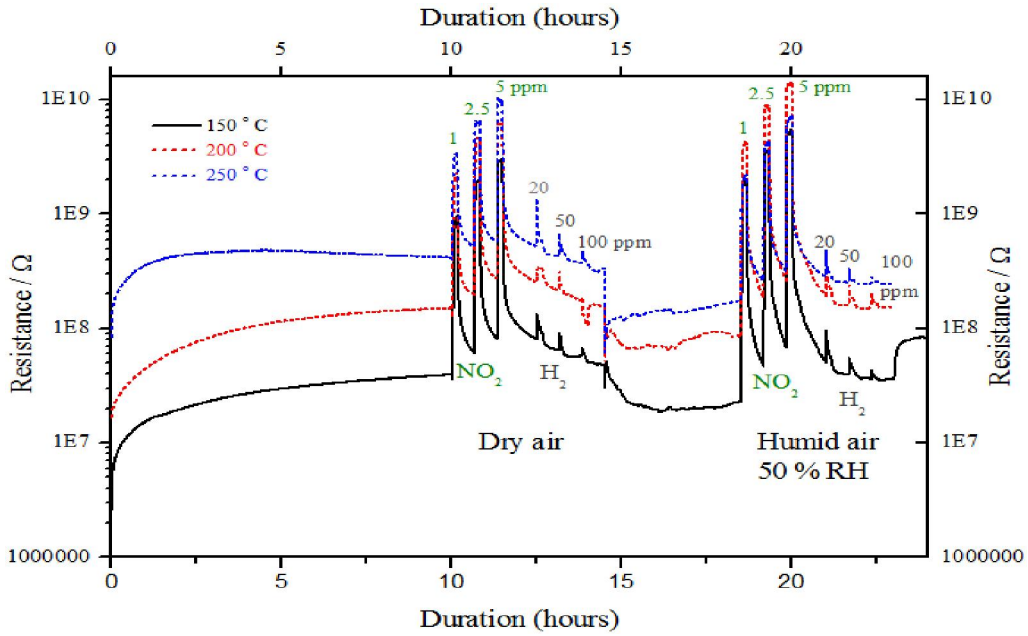

Fig.5.37.Response curves of sol-gel GC sample at 150, 200 and 250ºC

Sol-gel GC sample seems to be more sensitive to NO_2 than for H_2 (Fig.5.37). The best responses were attained at 150ºC (Fig.5.38).

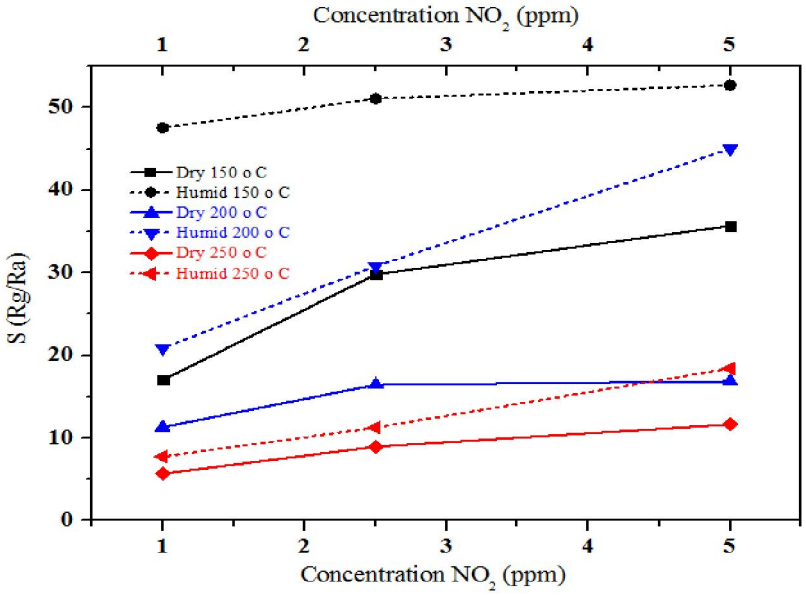

Fig.5.38. Sensor responses of GC sol-gel sample at 150, 200 and 250ºC under NO_2 in dry air and 50 %RH.

A certain interference with water vapor has been observed (Fig.5.38)

Conclusions

- It is established that we could obtain glass-crystalline material containing ZnO as a primary crystalline phase by melt quenching technique.
- Sol-gel glass ceramic gives the ability to detect NO_2 at a quite low working temperature (150ºC), in conditions close to the environmental ones by low cost procedure.
- Glass ceramic materials are promising in sensors application not only as humidity sensor but also for detecting several gases with a quite good selectivity.

References

1. T. Seiyama, Chemical Sensor Technology, 1 (1988) 57–78, ISBN: 978-0-444-98901-7.
2. G. Kostorz, High-Tech Ceramics Viewpoints and Perspectives (1989) 137–159, ISBN: 978-0-12-421950-2.
3. S. P. Mitoff, Electrical Conduction Mechanisms in Oxides, 4 (1966) 217-264, Oxford: Pergamon Press.
4. E.M. Logothetis, Resistive type exhaust sensors, Ceram. Proc. Eng. Sci. 1 (1980) 281- 301.
5. T. Y. Tien, H. L. Stadler, E. F. Gibbons and P. J. Zacmanidis, Ceramic Bulletin 54 (1975) 280-85.
6. T. Y. Tien, 1977. US Patent 4007435.
7. J. L. Pfeifer, T. A. Libsch and H. P. Wertheimer, Society of Automotive Engineers, New York: Paper 840142, International Congress & Exposition, Detroit, Michigan Feb 27-March 2, 1984.
8. K. P. Jagannathan, S. K. Tiku, H. S. A.Ray, A. Ghosh and E. C. Subbarao, (1980) 201-260, New York: Plenum Press.
9. Eddy, D. S., 1971. US Patent 3616, 274
10. S. A. Akbar, P. K. Dutta, High-temperature ceramic oxide gas sensors, Minerals, Metals and Materials Society, (1999) 33-44, Warrendale, PA.
11. E. Aukrust, and A. Muan, Journal of American Ceramic Society 46 (1963) 511.
12. D. C. Hill and H. L. Tuller, In Ceramic Materials for Electronics, Buchanan, R. C. (ed.), (1986) 265-375, New York and Basel. Marcel Dekker, Inc.

13. H. Windischmann, P. Mark, A model for the operation of a thin-film SnO_x conductance-modulation carbon monoxide sensor, J. Electrochem. Soc., 126 (1979) 627.

14. Y. Shimizu, Y. Nakamura,M. Egashira, Effects of diffusivity of hydrogen and oxygen through pores of thick film SnO_2-based sensors on their sensing properties Sensors Actuat. B13-14 (1993) 128-131.

15. S. A. Akbar, L. B. Younkman, Sensing mechanism of a titania-based CO sensor, J. Electrochem. Soc., 144 (1997) 1750-1753.

16. P. K. Dutta, A. Ginwalla, B. Hogg, B. R. Patton, B. Chwieroth, Z. Liang, P. Gouma, M. J. Mills, S. A. Akbar, Interaction of carbon monoxide with anatase surfaces at high temperatures: optimization of a carbon monoxide sensor, J. Phys. Chem., B103 (1999) 4412-22.

17. S. R. Morrison, Selectivity in semiconductor gas sensors, Sensors and Actuators 12 (1987) 425-440.

18. T. Oyabu,T. Kurobe, and T. Hidai, In Chemical Sensors: Analytical Chemistry Symposia Series, T. Seiyama, , K. Fueki, , J. Shiokawa, and S. Suzuki (eds), 17 (1983) 12-17, Tokyo: Kodansha and Elsevier.

19. A. L. Micheli, S. C. Chang and D. B. Hicks, Ceramics Engineering and Science (1987) 1095-1105.

20. S. Somiya, S. Hirano and M. Ishizaka, Phase equilibrium in the system MgO-Cr_2O_3-TiO_2 air at 1400 degree Celsius, Journal of the ceramic society of Japan, 85 (1977) 201-209.

21. T. Nitta, Z. Terada and S. J. Halyadawa, Journal of the American Ceramic Society 63 (1980) 295-300.

22. E. Andrich, Electrical Appliances 26 (1965/66) 123.

23. O. J. Saburi, Properties of Semiconductive Barium Titanates, Journal of the Physical Society of Japan, 14 (1959) 1159-74.
24. T. -Y. Tien and W. G. Carlson, Influence of Oxygen Partial Pressure on Properties of Semiconducting Barium Titanate, Journal of the American Ceramic Society, 46 (1963) 297-98.
25. G. J. Goodman, Electrical Conduction Anomaly in Samarium-Doped Barium Titanate, American Ceramic Society 46 (1963) 48-54.
26. W. Heywang, Bariumtitanat als sperrschichthalbleiter, Solid State Electronic 3 (1961) 51-58.
27. W. Göpel and G. Reinhardt, Metal Oxide Sensors: New Devices Through Tailoring Interfaces on the Atomic Scale, VCH, Weinheim (FRG) 1 (1996) 49, ISBN 3-527-29329-9.
28. A. C. C. Rotzetter, N. A. Luechinger, E. K. Athanassiou, D. Mohn, F. M. Koehler and R. N. Grass, Sintering of core–shell Ag/glass nanoparticles: metal percolation at the glass transition temperature yields metal/glass/ceramic composites, J. Mater. Chem., 20 (2010) 7769–7775.
29. G. Goor, P. Stigesser, K. Berroth, Electrically conductive ceramic composites, Solid State Ionics 101-103 (1997) 1163-1170.
30. S. N. Gwirc, Glass modified sensitive surface thick film humidity sensor, Sensors and Actuators B, 18-19 (1994) 107-110.
31. M. Milanova , R. Iordanova , L. Aleksandrov , M. Hassan , Y. Dimitriev, Glass formation and structure of glasses in the ZnO—Bi_2O_3—WO_3—MoO_3 system, Journal of Non-Crystalline Solids 357 (2011) 2713–2718.
32. J. P. Guna, S. Kunej, D. Suvorov, Phase equilibrium relations in the binary system Bi_2O_3-ZnO, J. Mater. Sci. 39 (2004) 911-918.

33. Š. Kunej, J. P. Guha and D. Suvorov, The formation and stability of a body – centered – cubic γ-Bi_2O_3 solid solution in the Bi_2O_3-ZnO system, Acta Chim. Slov., 51 (2004) 551-558

34. E. I. Speranskaya, The Bi_2O_3-WO_3 system, Neorg. Mater. 6 (1970) 149-151.

35. S. N. Hoda, L. L. Y. Chang, Phase Relations in the System Bi_2O_3-WO_3, J. Am. Ceram. Soc. 57 (1974) 323 - 326.

36. C. D. Ling, R. L. Withers, S. Schmid, J. G. Thompson, A Review of Bismuth-Rich Binary Oxides in the Systems Bi_2O_3–Nb_2O_5, Bi_2O_3–Ta_2O_5, Bi_2O_3–MoO_3, and Bi_2O_3–WO_3, J. Solid State Chem. 137 (1998) 42 - 61.

37. C. D. Ling, Structural Relationships among Bismuth-Rich Phases in the Bi_2O_3– Nb_2O_5, Bi_2O_3– Ta_2O_5, Bi_2O_3–MoO_3, and Bi_2O_3–WO_3 Systems, J. Solid State Chem. 148 (1999) 380 - 405.

38. A. Watanabe, A. Ono, Thermostable region of an oxide ion conductor, $Bi_7WO_{13.5}$ (=$7Bi_2O_3 \cdot 2WO_3$), and the solid solubility extension, Solid State Ionics 174 (2004) 15-18.

39. A. Watanabe, Polymorphism in $Bi_{14}WO_{24}$: A monoclinic low-temperature stable form with $\beta \approx 90°$ and its displacive transformation to an orthorhombic intermediate form at about 40 °C, Solid State Ionics 176 (2005) 1281-1289.

40. K. S. Knight, The crystal structure of russellite; are-determination using neutron powder diffraction of synthetic Bi_2WO_6, Mineral. Mag. 56 (1992) 399 - 409.

41. A. D. Rae, J. G. Thompson and R. L. Wuthers, Structure Refinement of Commensurately Modulated Bismuth Tungstate, Bi_2WO_6, Acta Crystallogr. B47 (1991) 870.

42. R. Newnhman, R. Wolf, J. Dorrian, Structural Basis of Ferroelectricity in the Bismuth Titanate Family, Mater. Res. Bull. 6 (1971) 1029 - 1040.

43. A. Watanabe, M. Gota, Characterization of $Bi_2W_2O_9$ having a unique layered structure, Less-Common Metals 61 (1978) 265 - 272.

44. JC. Champarnaud-Mesjard, B. Frit and A. Watanabe, Crystal structure of $Bi_2W_2O_9$, the n=2 member of the homologous series $(Bi_2O_2)B^{VI}_nO_{3n+1}$ of cation-deficient Aurivillius phasesJ. Mater. Chem., 9 (1999) 1319 - 1323.

45. D. J. Morell, J. S. Cantrell, L. L. Y. Chang, Phase Relations and Crystal Structures of Zn and Cd Tungstates, J. Am. Ceram. Soc. 63 (5-6) (1980) 261-264.

46. P. F. Schofield, K. S. Knight, G. Cressey, Neutron powder diffraction study of the scintillator material $ZnWO_4$, J. Mater. Sci. 31 (1996) 2873-2877.

Chapter 6 – Commercial In_2O_3 and ZnO different morphologies NO_x sensors

The objective of this work is the development of materials with hierarchical architectures for the realization of gas sensors capable of detecting low concentration of NO_2 in air at low temperature. Although the results of the research will likely be of interest in several fields, the development of gas sensors is the field of application to which this research is devoted.

A quite novel approach is the development of hierarchical structures and nanostructures. There are different hierarchical structures proposed in the literature, but in general they are made of a microstructure with relatively large pores which walls are decorated with nanostructured objects. The rapid and effective gas diffusion toward the entire sensing surfaces is facilitated by the microporous structure, and the nanostructure offers a large sensing surface area. Thus both the gas response and response speed should increase simultaneously and substantially [1].

This work has been done within PRIN project 2009 “Development of materials with hierarchical architectures for nitrogen oxides sensors operating at low temperature, for environmental monitoring” Four research units had been involved in this project Università di Padova (PD), Università di Pavia (PV), Università di L'Aquila (AQ) and Politecnico Di Torino.

This project aims to exploit the potentialities of nanostructured materials and hierarchical architectures obtained from different methods in the development of high sensitive sensors for nitrogen dioxide, operating at low temperatures. The activities of the involved research units will be focused on the synthesis of thick and thin films, and on hierarchical structures obtained from three oxides: ZnO, WO_3 and In_2O_3. The

tests on the sensitivity of the produced materials will be performed using different techniques; conductometric, potentiometric, optic.

6.1. Thin nanostructured films for gas sensing

The development of better efficient gas sensors can take advantage from nanotechnologies, both in the bottom-up development of new materials and structures, and the top-down fabrication of miniaturized devices by radiation lithography or imprinting techniques on suitable materials. The application of nanostructured materials in the design of new gas-sensing devices is presently one of the most dynamic research issues, as it is possible to increase the sensing performance by exploiting the high activity, large specific surface and small size of active materials [2]. During the last years Università di Padova developed nanocomposite materials based on porous sol-gel SiO_2 films containing Au and NiO nanoparticles and used their transmittance properties to selectively detect H_2 and CO [3]. Through the control of the porosity in the matrix and the shape and structure of the nanoparticles it was shown that the optical gas sensing properties of the nanocomposite film can be adjusted to optimize both the sensitivity and the selectivity [4, 5].

Università di Pavia recently developed a micropatterning method based on soft-lithography techniques, which enables the realization of complex integrated devices. During this project two techniques will be considered: microtransfer molding and capillary force lithography [6, 7, and 8]. In microtransfer molding, the stamps are filled with a precursor solution and are then placed in contact with the substrate. In capillary force lithography, the precursor is spin or dip coated on the substrate, then the elastomeric mold is placed on the film and left unperturbed for an extended period of time. Once solvent evaporated through the stamp and image is formed. In both

cases the patterned hydrogel is solidified through UV exposure and the stamp is removed.

6.2. Hierarchical structures for gas sensing

A quite novel approach is the development of hierarchical structures and nanostructures. The concept at the base of this approach is that both thick and thin films have advantages and drawbacks, and hierarchical architectures should allow minimizing the disadvantages and maximizing the advantages. A "hierarchical structure" is a micro- or nanostructure composed of many low dimensional nano-building blocks. In these structures the nanocomponents are represented by nanoparticles, or nanowires, assembled in order to form large complex microstructures characterized by an extremely large surface/volume ratio and by an extremely high surface area. The rapid and effective gas diffusion toward the entire sensing surfaces is facilitated by the microporous structure, and the nanostructure offers a large sensing surface area. Thus, both the gas response and response speed should increase simultaneously and substantially [6]. In the recent literature two types of hierarchical structures received attention in relation with gas sensing applications: hollow structures, based on the organization of nanoparticles, and dendritic/urchin structures deriving from the organization of nanowires or nanotubes [6]. Three-dimensional tungsten oxide nanowire networks have been obtained and used to build high-surface area, ultrasensitive and highly selective gas sensors.

Low concentrations of NO_2 (50 ppb) could be detected in this way [7]. Brush-like hierarchical ZnO nanostructures were tested as ethanol sensors [8], but recently also bunched roselike and core-shell-like particles have been synthesized [1]. Also In_2O_3 has been investigated and hierarchical and hollow microspheres have been tested for

CO sensing [9]. The application of these structures to gas detection, particularly in the case of NO_x detection is, however, still very limited [10].

6.3. ZnO and In_2O_3 sensing materials choice

Trends in the stability of different oxidation states are very important in surface chemistry, as they control both the types of defect that may be formed easily, and the type of chemisorptions that may take place. Only transition-metal oxides with *d*0 and *d*10 electronic configurations find their real gas sensor application. As we know, the post-transition-metal oxides, such as ZnO and SnO_2 have cations with the filled *d*10 configuration. The *d*0 configuration is found in binary transition-metal oxides such as TiO_2, V_2O_5, WO_3, and also in perovoskites such as $ScTiO_3$, $LiNbO_3$, etc.

These compounds share many features with the non-transition metal oxides. They have a filled valence band of predominantly O 2p character, and gap between valence band and an empty conduction band. Typical band gaps are 3–4 eV.

Unlike transition-metal oxides with $0 < n < 10$, stoichiometric, post-transition-metal oxides ZnO, SnO_2, and *d*0 transition-metal oxides may be reduced, but not oxidized. The post-transition oxides ZnO, In_2O_3, SnO_2, as well as majority of transition-metal oxides are active in “redox” reactions since the electron configuration of the solid may be altered. However, the reaction with oxidizing species such as O_2 is expected only with samples that have been bulk reduced or where the surfaces have been made oxygen deficient. At that the reduction of post-transition oxides as a rule leads to the formation of free carriers, which greatly increase the metal oxide conductivity, a fact that is crucial for sensor applications.

However, limited use of pure transition-metal oxides ($1 < n < 10$) for conductometric gas sensor fabrication does not mean that transition-metal oxides are not of interest of

gas sensor designers. On the contrary, unique surface properties, plus high catalytic activity make them very attractive for various sensor applications, such as properties' modification of more stable and wide band gap oxides, and forming of more complicated nanocomposite materials [11].

6.3.1. Zinc Oxide

The modern technological progress is closely related to the fundamental investigation of known materials and revolutionary changes in the techniques of their synthesis, which result in the obtaining of principally new materials including also nanostructures. In this respect, zinc oxide represents particular interest from the point of view of its multi-functionality and opportunities of modification and management of various nanostructures. An important specific characteristic of ZnO is its unique ability to form nanostructures with different morphology and different sizes: ribbon, tubes, rods, wires, and tetrapods. One dimensional semiconductor nanowires and nanorods have attracted increasing attention due to their physical properties arising from quantum confinement (such as electronic quantum transport and enhanced radiative recombination of carriers) Zinc oxide (ZnO), a wide bandgap (3.4 eV) II-VI compound semiconductor, has a stable wurtzite structure with lattice spacing a = 0.325 nm and c = 0.521 nm. It has attracted intensive research effort for its unique properties and versatile applications in transparent electronics, ultraviolet (UV) light emitters, piezoelectric devices, chemical sensors and spin electronics [12].

Zinc oxide crystallizes in three forms: hexagonal wurtzite (Fig.6.1a), cubic zinc blende (Fig.6.1b), and the rarely observed cubic rocksalt (Fig.6.1c)). The wurtzite structure is most stable at ambient conditions and thus most common. The zinc blende form can be stabilized by growing ZnO on substrates with cubic lattice structure. In

both cases, the zinc and oxide centers are tetrahedral. The rocksalt (NaCl-type) structure is only observed at relatively high pressures about 10 GPa [13].

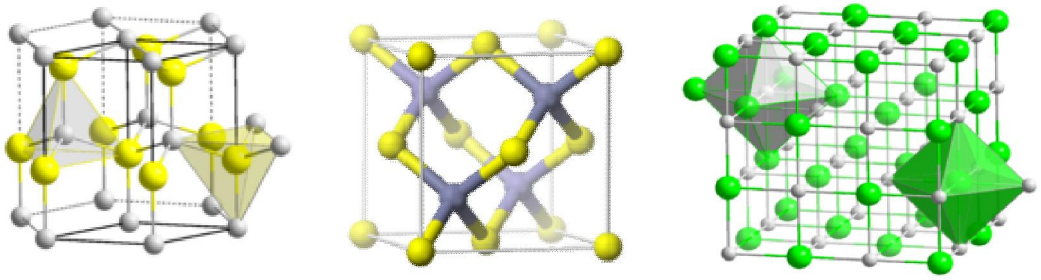

a) wurtzite b) zinc blende c) rocksalt

Fig.6.1. ZnO polymorphs

Based on the remarkable physical properties and the motivation of device miniaturization, large effort has been focused on the synthesis, characterization and device applications of ZnO nanomaterials. An assortment of ZnO nanostructures, such as nanowires, nanotubes, nanorings, and nano-tetrapods have been successfully grown via a variety of methods including chemical vapor deposition, thermal evaporation, and electrodeposition, etc [14].

Recently many advances take place in ZnO nanostructures. Issues of synthesis methods, structural, electrical, optical, magnetic, and gas sensing properties are summarized.

6.3.1.1. Chemical Sensing prosperities of ZnO

Oxygen vacancies on metal-oxide surfaces are electrically and chemically active. These vacancies function as n-type donors and often significantly increase the conductivity of oxide. Upon adsorption of charge accepting molecules at the vacancy sites, such as NO_2 and O_2, electrons are effectively depleted from the conduction

band, leading to a reduced conductivity of the n-type oxide. On the other hand, molecules, such as CO and H_2, would react with surface adsorbed oxygen and consequently remove it, leading to an increase of conductivity. Most metal-oxide gas sensors operate based on this principle. As one of the major materials for solid state gas sensor, bulk and thin films of ZnO have been proposed for CO, NH_3, alcohol and H_2 sensing under elevated temperature (~400°C). From the aspect of sensing performance, Q1D ZnO, such as nanowires and nanorods, is expected to be superior to its thin film counterpart. Since their diameter is small and comparable to the Debye length, chemisorption induced surface states effectively affect the electronic structure of the entire channel, thus confer Q1D ZnO higher sensitivity than thin film. In addition, ZnO nanowires and nanorods can be configured as either two terminal sensing devices or as FETs in which a transverse electric field can be utilized to tune the sensing property. Recently, Wan et al [15] fabricated ZnO nanowire chemical sensor using microelectromechanical system technology. Massive nanowires were placed between Pt interdigitating electrodes. Under an operation temperature of 300°C, the resistance of nanowires significantly decreases upon exposure to ethanol. Electrical transport studies show that O_2 ambient has considerable effect on the ZnO nanowires. Fan et al. [16] discussed the relationship between oxygen pressure and ZnO nanowire FET performance. It is shown that ZnO nanowires have fairly good sensitivity to O_2 (Fig.6.2a). In addition, it is observed that the sensitivity is a function of back gate potential, i.e., above gate threshold voltage of FET, sensitivity increases with decreasing gate voltage (Fig.6.2a inset). This implies that the gate voltage can be used to adjust the sensitivity range. Furthermore, a gate-refresh mechanism was proposed. As demonstrated in Fig.6.2b, the conductance of nanowire can be recovered by using a negative gate potential larger than the threshold voltage. The gas selectivity

for NO_2 and NH_3 using ZnO nanowire FET was also investigated under the gate refresh process, exhibiting a gas distinguish ability function. The large surface-to-volume ratio of nanowires not only results in their enhanced gas sensing performance, but also facilitates potential hydrogen storage property. Wan et al. [17] investigated hydrogen storage characteristics under room temperature. The highest storage of 0.83 wt% was achieved at a pressure of 3.03 MPa. It was suggested that hydrogen storage was due not only to surface adsorption but also to the incorporation of H_2 into the crystal interstitial sites [18].

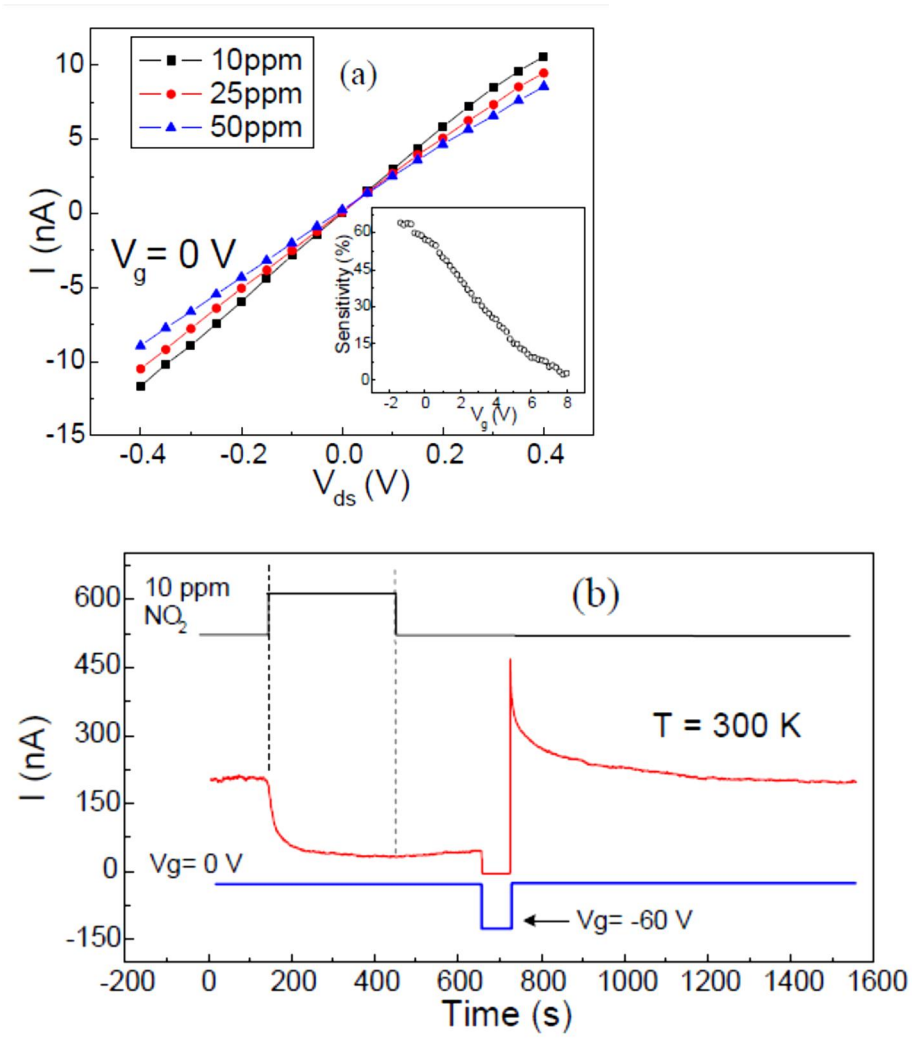

Fig.6.2 (a) I-V curves of a ZnO nanowire under 50 ppm O_2. Inset: gate potential dependence of sensitivity under 10 ppm O_2. (b) The nanowire sensing response to 10

ppm NO_2 and the conductance recovery process assisted by a -60 V gate voltage pulse [18].

6.3.2. Indium Oxide

Indium oxide (In_2O_3) has attracted considerable research. It is known to have a body centered cubic structure (a = 1.012 nm). In_2O_3 has been widely used in the microelectronic field as gas detectors, window heaters, solar cells, memory devices, and flat panel display materials.

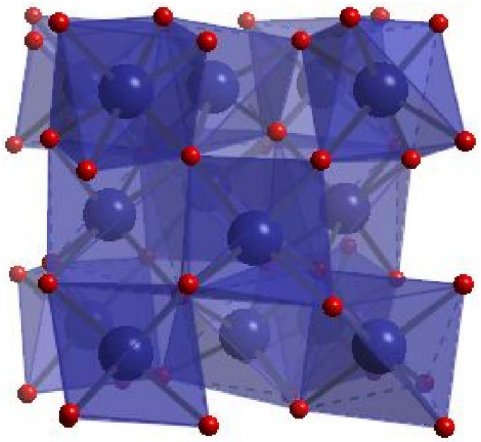

Fig.6.3: In_2O_3: body centered cubic structure [19].

The applications of the In_2O_3 nanostructures depend on controlled synthesis of these materials with specific morphologies. Different In_2O_3 morphologies such as nanowires (including nanowire arrays), nanobelts, nanoparticles (including nanocubes, nanoflowers and octahedra), nanotowers, microarrows, nanotubes, In/In_2O_3 nanocables, lotus-root-like In_2O_3 nanorods and nanocolumns, nanocrystal chains, and hollow spheres have been prepared by chemical vapor deposition (CVD), pulsed laser deposition (PLD), the alumina or mesoporous silica template method, and wet chemical methods, and so on.

1-D has attracted tremendous attention since the revolutionary discovery of carbon nanotubes in 1991.These 1-D nanostructures with high aspect-ratios suggest better crystallinity, smooth surface, higher integration density, and lower power consumption. Moreover, owing to a large surface-to-volume ratio and a Debye length comparable to the small size, they exhibit superior sensitivity to surface chemical processes. Also, their size internment provides tunable band gap, higher optical gain, and faster operation speed. 1-D In_2O_3 nanostructures have been employed to fabricate field-effect transistors, nanoscale chemical sensors for the detection of NO_2, NH_3, acetone, DNA, and biosensing devices, *etc.*

6.3.2.1. General properties of In_2O_3

Indium (III) oxide (In_2O_3) is an amphoteric oxide of indium. It is an n-type semi-conductor and it forms bixbyite type cubic crystals. Its band gap has recently been recalculated to be equal to 2.9 eV from the old value of about 3.7 eV. Indium oxide is used in some types of batteries, thin film infrared reflectors transparent for visible light (hot mirrors), optical coatings, antistatic coatings, photocatalyst sensors, etc. It is also used in resistive elements and integrated circuits. When combined with tin oxide, it forms indium tin oxide, traditionally known as ITO, and used for transparent conductive coatings. In histology, indium oxide is used as a part of some stain formulations. Thin films of chromium-doped indium oxide ($In_{2-x}Cr_xO_3$) were recently reported to be magnetic semiconductors displaying high-temperature ferromagnetism, single-phase crystal structure, and semiconductor behavior with a high concentration of charge carriers. It has possible applications in spintronics as a material for spin injectors. Recent theoretical simulation predicted that the oxygen-depleted indium oxide (100) surface could be ferromagnetic [20].

6.3.2.2. Sensing prosperities of In_2O_3

The sensors based on WO_3, NiO, In_2O_3 and some composite materials exhibit good performance in NO_2 detection. Due to the high conductivity and abundant defects both in the sensing body and on the surface, indium oxide (In_2O_3) is a promising candidate for practical application. Especially, In_2O_3 shows superior response and selectivity in detecting NO_2 gas, while not so much sensitive to reducing gases. Because NO_2 is a polar molecule, the adsorption and desorption are sluggish on In_2O_3 surface which leads to the slow response and recovery speed. Through the microstructure design, the sensing properties of semiconductor oxide can be greatly improved, especially for detecting low concentration of NO_2 (ppb level) with a fast response and recovery speed. Until now, besides the different structural phases, well-defined In_2O_3 nanostructures with various morphologies such as one-dimensional nanowires, two-dimensional nanosheets and three-dimensional hierarchical microstructures have been fabricated. For various morphologies of In_2O_3 nanostructures, several approaches, such as physical evaporation technique, chemical vapor deposition, thermal oxidation, template method, homogeneous precipitation, sol‑gel method, elements directly synthesis and precursor method, have been widely reported.

Generally, as an n-type semiconductor, In_2O_3 has been extensively exploited in applications related to gas sensing. In_2O_3 is strongly sensitive to oxidizing gases.

Table 6.1: Comparison of gas-sensing characteristics of In_2O_3 gas sensors fabricated by different approaches.

Material	**Fabrication approach**	**NO_2 (ppm)**	**T (˚C)**	**Sensor response**	**Reference**
In_2O_3 nanowires	Hydrothermal route	1	250	2.57	[21]
In_2O_3 nanocrystals	Ice-water bath	1	83	52.1	[22]
In_2O_3 nanofibers	Electrospinning	100	300	1.8	[23]
SnO_2-In_2O_3	Sol-gel methods	2	250	125	[24]
In_2O_3 nanostructures	Hydrothermal route	0.5	Room temperature	618	[25]

6.4. Characterization and experimental results

6.4.1. Powders characterization:

Three different commercial powders have been bought and characterized:

1) ZnO :(Aldrich > 99 %),

2) ZnO nanopowder: (VP AdNano® ZnO 20 Degussa > 99 % particle size ~100 nm),

3) In_2O_3: (Aldrich > 99 %, particle size below 100 nm),

Particle size distribution has been determined by means of a laser granulometer before and after ultrasonication for 5 min (Fig.6.4-4.10).

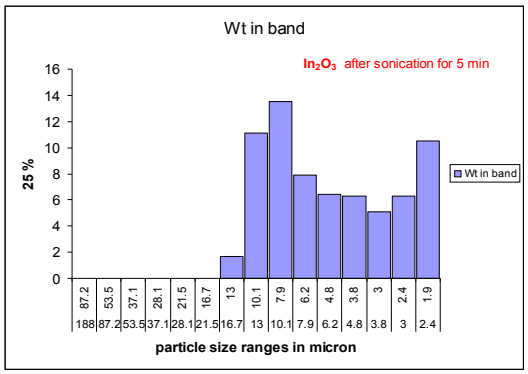

Fig.6.4: In_2O_3 particle size distribution

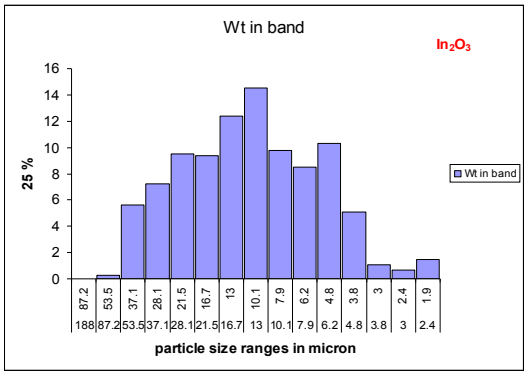

Fig.6.5: In_2O_3 particle size after sonication

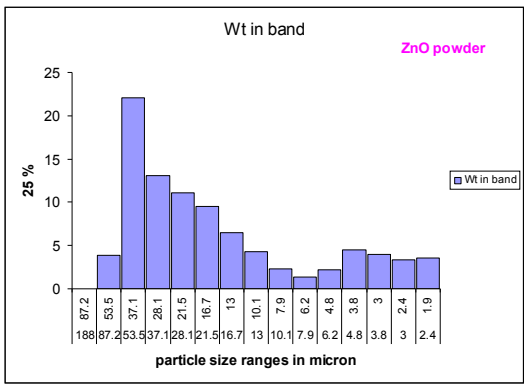

Fig.6.6: ZnO particle size distribution

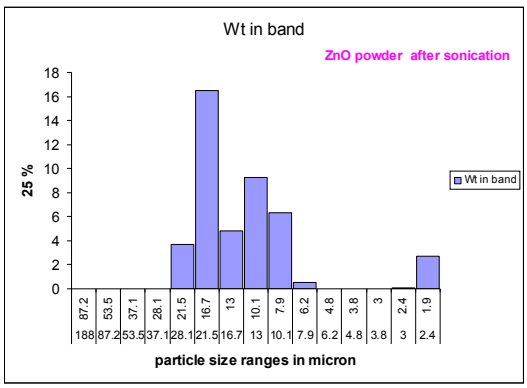

Fig.6.7: ZnO particle size after sonication

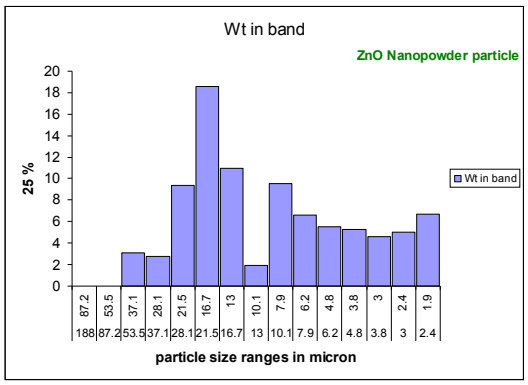

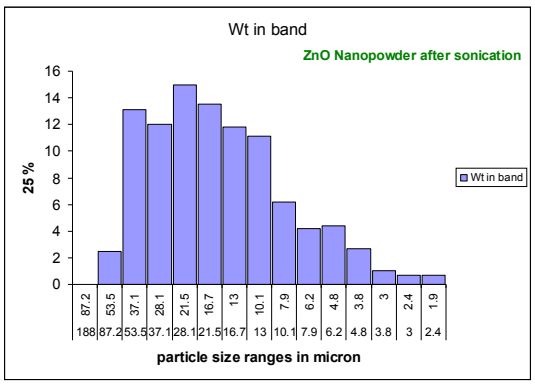

Fig.6.8: ZnO Nano particle size distribution

Fig.6.9: ZnO Nano particle size after sonication

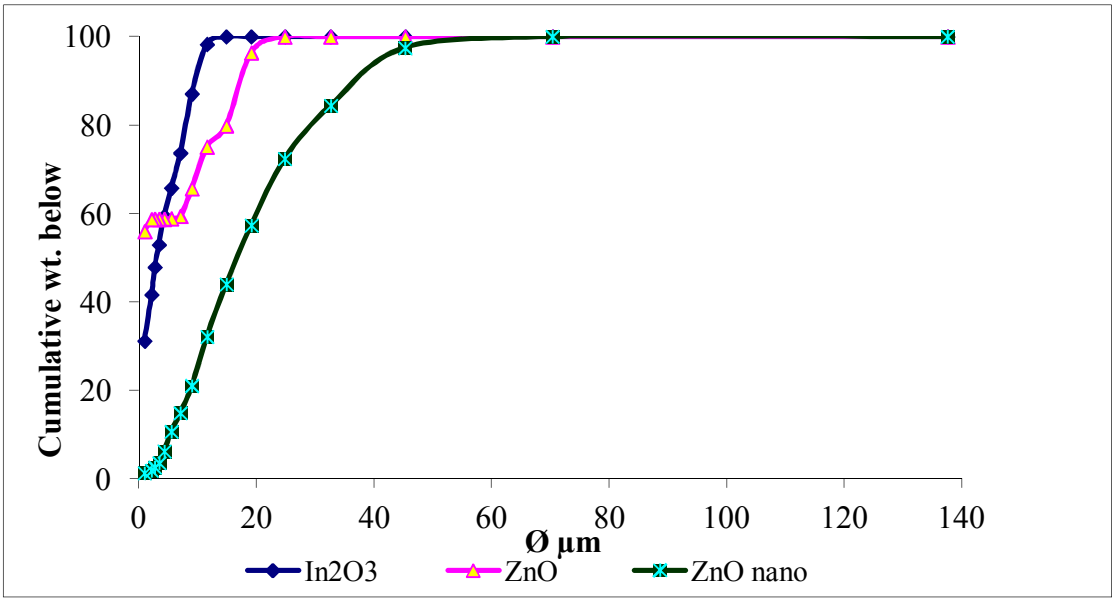

Fig.6.10: Overall cumulative curves after sonication

Tab.6.2: Diameters at 20, 50 and 80 wt% of the cumulative curve for the different powders

Cumulative wt%	**In_2O_3 µm**	**ZnO µm**	**ZnO Nano µm**
20	0.61	0.34	8.53
50	3.21	0.85	16.64

80	8.27	14.87	30.90

All the particle size distribution of the different powders indicate that they seem to be agglomerated but their dimensions are compatible with the openings of the steel screen mesh (45 microns) used for the screen printing process.

SEM observations of the used powders:

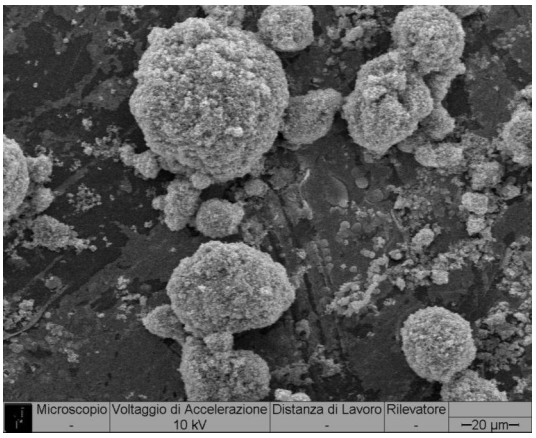

Fig.6.11: ZnO powder x 600

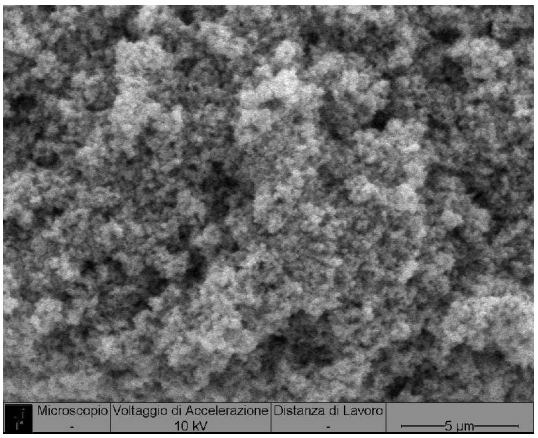

Fig.6.12: ZnO powder x 5000

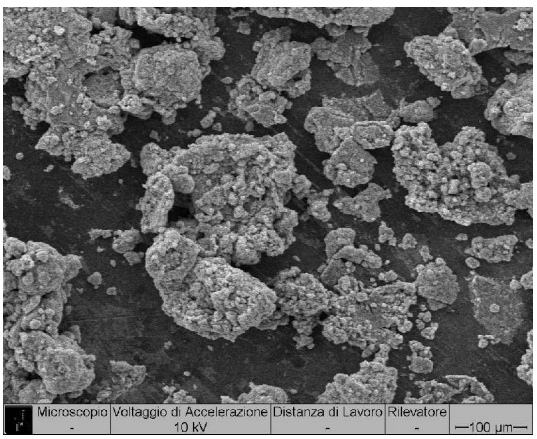

Fig.6.13: ZnO nanopowder x 150

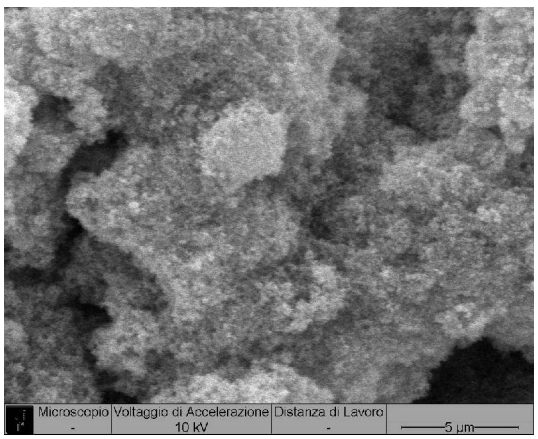

Fig.6.14: ZnO nanopowder x 5000

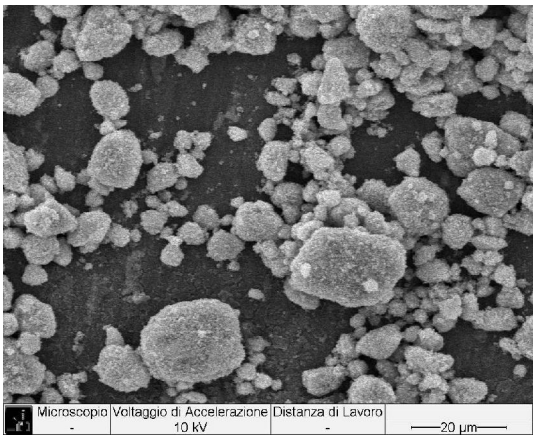

Fig.6.15: In_2O_3 powder x 1000

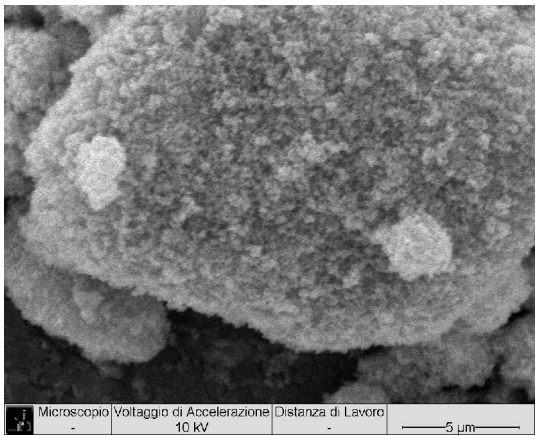

Fig.6.16: In_2O_3 powder x 5000

From SEM observations (Fig.6.11 - 4.16) we can conclude that all the powders are very fine with a tendency to agglomerate because of their small size.

These results confirm particle size measurements by means of laser granulometry.

X-Ray diffraction analyses (Fig.6.17-19) were carried out by means of a Philips PW 3830 X-ray generator, with a Cu Kα radiation (λ =0.154056 nm and 40 kV, 30 mA.

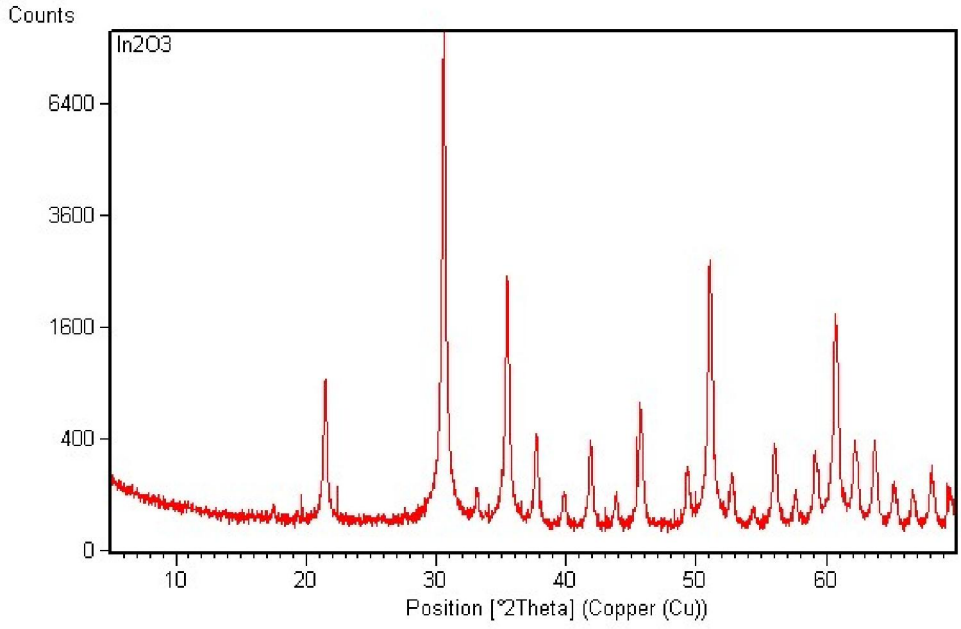

Fig.6.17: XRD pattern for In_2O_3 powder (compatible with JCPDS card 71- 2195)

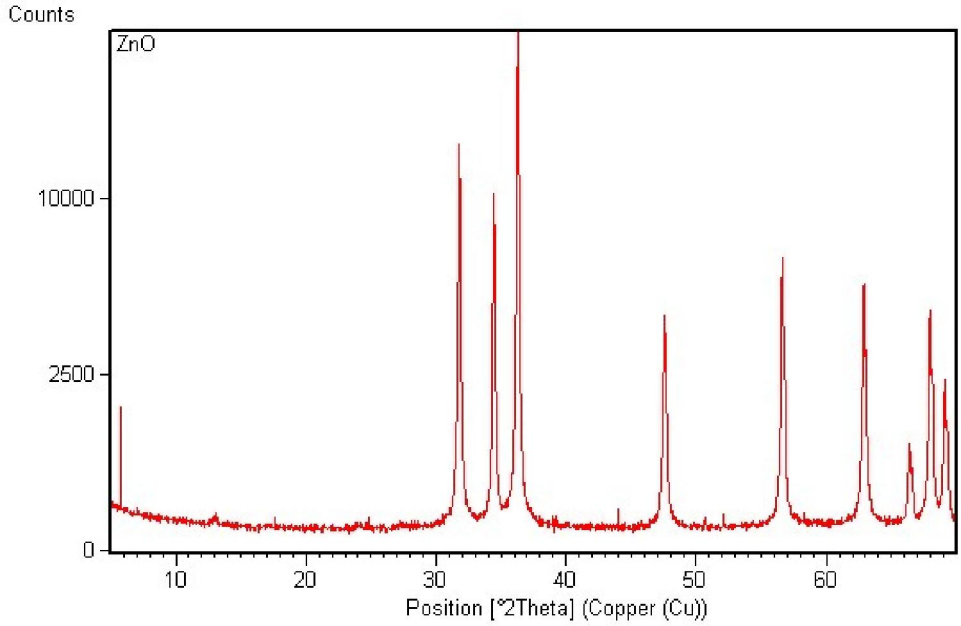

Fig.6.18: XRD pattern for ZnO powder (compatible with JCPDS card 36-1451)

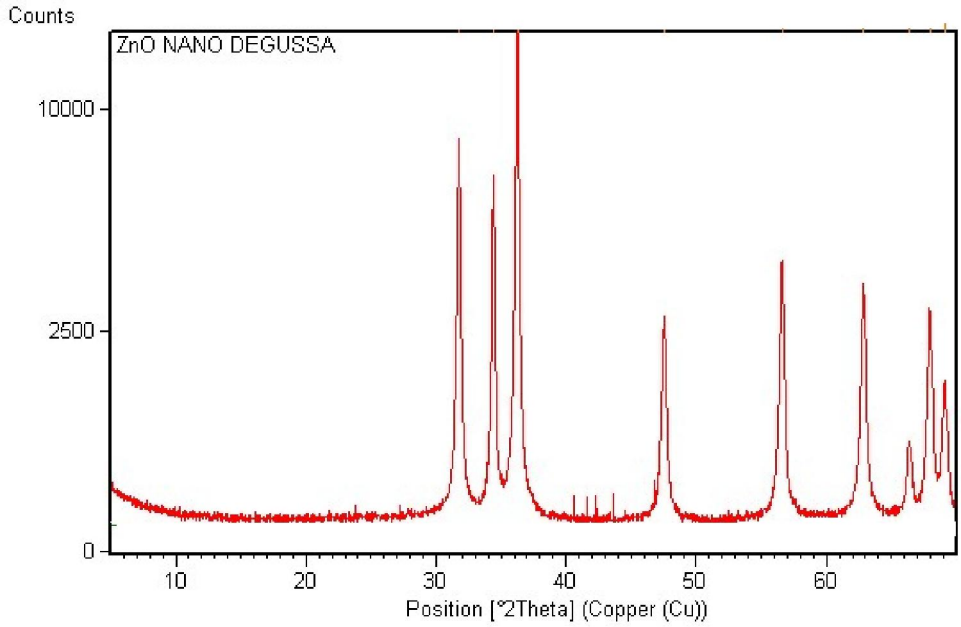

Fig.6.19: XRD pattern for ZnO nanopowder (compatible with JCPDS card 36-1451)

6.4.2. Thick - films preparation

Inks preparation took place by:

Mixing PVB "polyvinyl butyral" + EMFLOW, ball milling overnight; then mix with 2 grams of the used oxides (ZnO, In_2O_3) and ball milling again overnight and finally to check the viscosity of the prepared ink.

- Screen printing the ink over alumina substrates for vapor water interference check, and over silica and Si_3N_4 substrates for NO_2 measurements.

- Allow printed inks to dry on air overnight.

- Firing the inks over each substrate with the chosen temperature according to the nature of the substrate we used: 900°, 1000°C for alumina substrates and 700°C for both silica and Si_3N_4 substrates.

- Checking the adhesion of the inks over the substrates using scotch tape test technique.

- Screen printing interdigitated electrodes over the inks, for alumina substrates only.

- The sensor responses SR of the materials have been studied by means of electrical resistance measurements, in function of time, and varying the relative humidity (RH) by steps, each of 3 minutes (Fig.6.20).

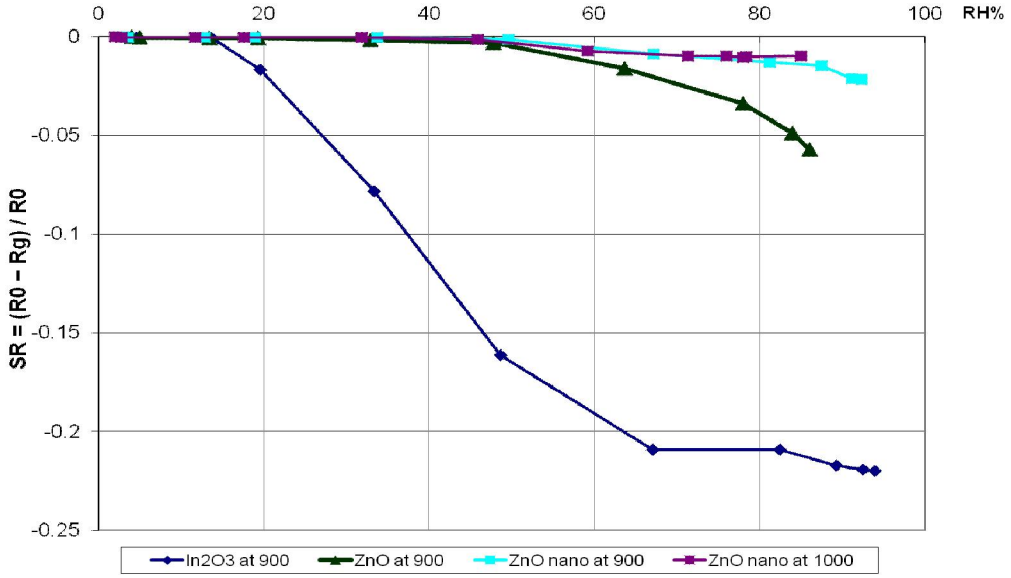

Fig.6.20: Sensor response at room temperature in function relative humidity

ZnO sensors seem to be insensitive to humidity, while In_2O_3 sensor's response is slightly influenced by water vapor presence.

6.4.3. Thick - films characterization

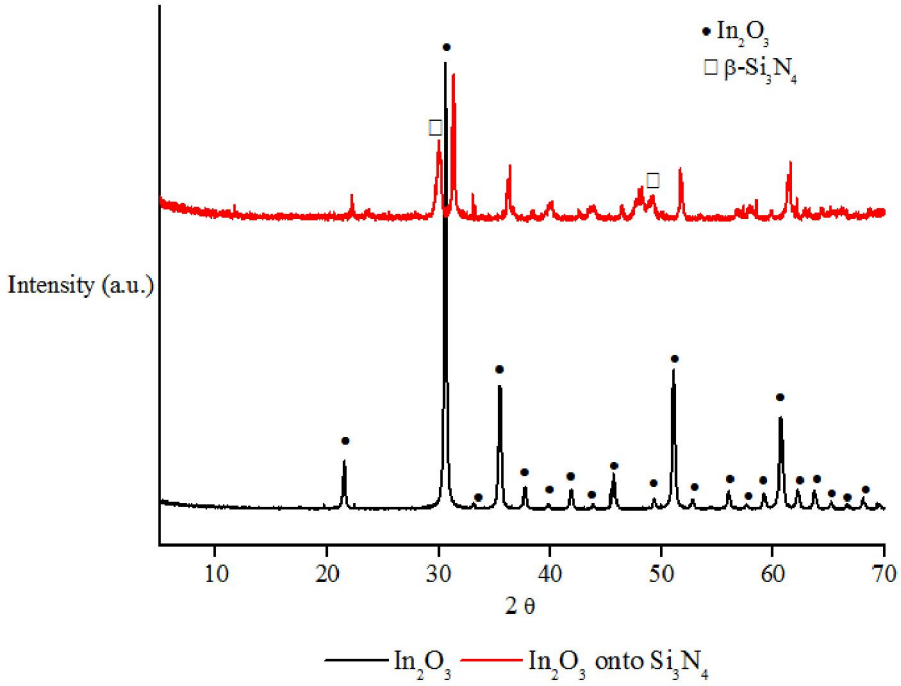

Fig.6.21: XRD pattern for In_2O_3 as received powder and thick – film onto Si_3N_4 substrate treated at 700°C (compatibles with JCPDS cards 22- 0336, 71 – 2195 and 33-1160.

XRD of In_2O_3 thick film fired at 700°C is quite close to rhombohedral phase (JCPDS card 22- 0336), while the as received In_2O_3 powder has the cubic structure (JCPDS card 71-2195). The presence of the substrate phase has been observed in the form of β- Si_3N_4 (JCPDS card 33-1160) with a right shift for all peaks which could be due to the thermal treatment (Fig.6.21).

SEM observations of the thick-films:

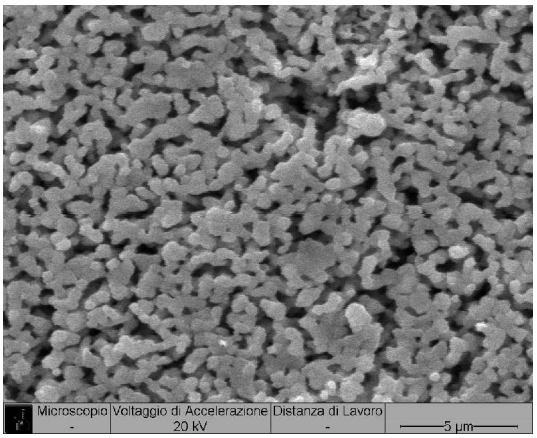

Fig.6.22: ZnO nanopowder onto Al_2O_3 substrate fired at 900°C x3000

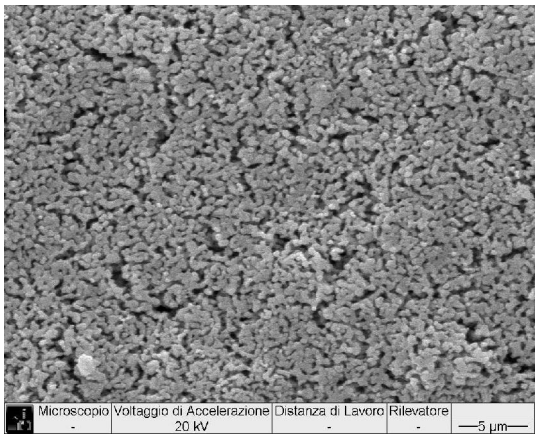

Fig.6.23: ZnO nanopowder fired at 1000°C x5000

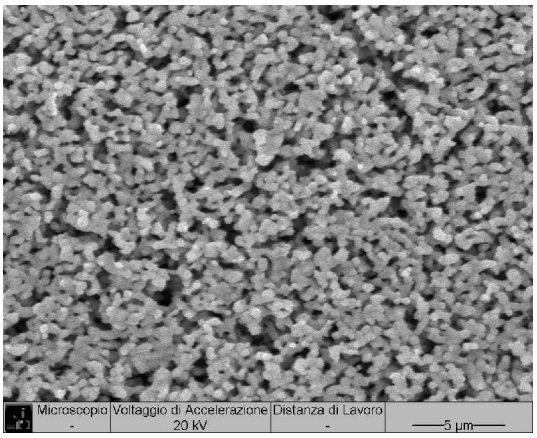

Fig.6.24: ZnO onto Al_2O_3 substrate fired at 900°C x4000

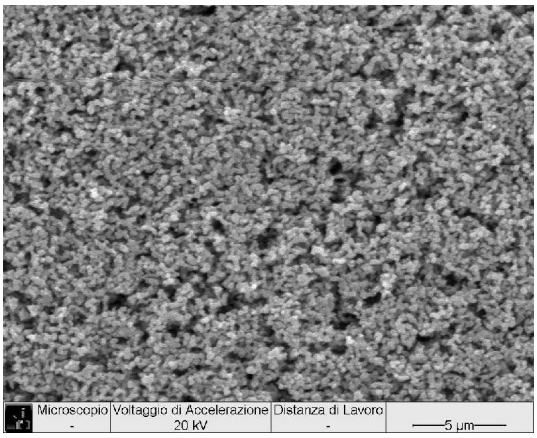

Fig.6.25: ZnO onto Alumina fired at 1000°C x5000

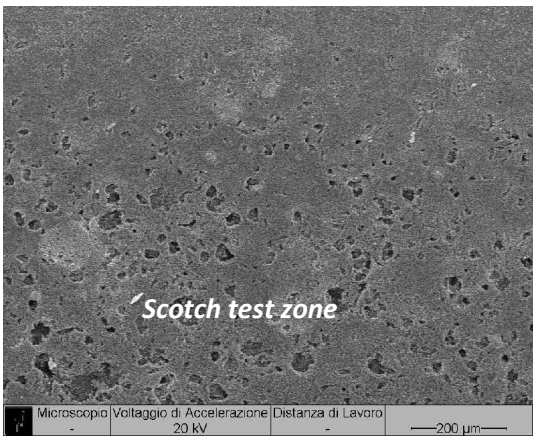

Fig.6.26: ZnO onto Si_3N_4 substrate

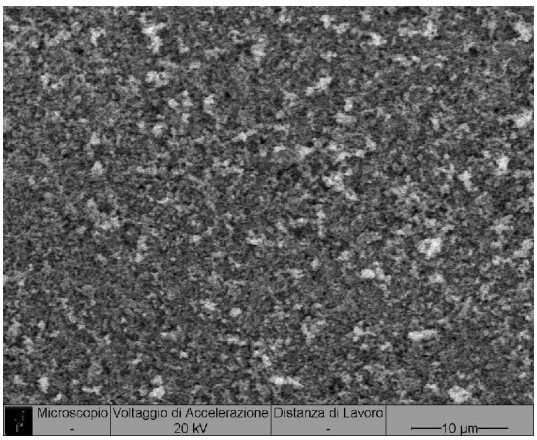

Fig.6.27: ZnO onto Si_3N_4 substrate fired

fired at 700°C x100

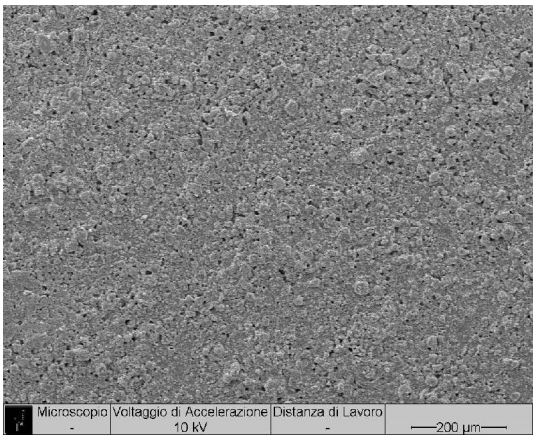

Fig.6.28: In_2O_3 on Si_3N_4 substrate fired at 700°C x100

at 700°C x1000

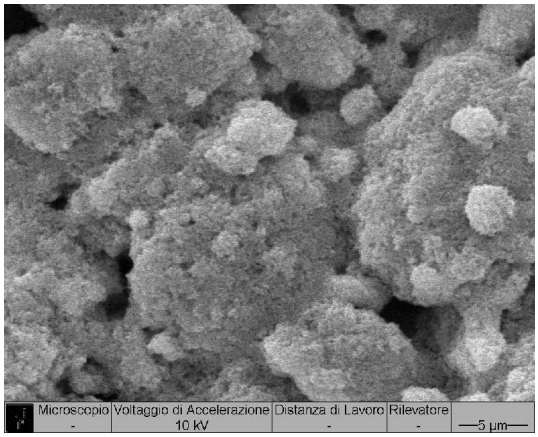

Fig.6.29: In_2O_3 on Si_3N_4 substrate fired at 700°C x 3000

ZnO and In_2O_3 thick-films presented after firing a good adhesion onto the various substrates (alumina, silica and silicon nitride).

All the films seem to be porous and compatible with the targeted application.

6.4.4. Electrical Characterization – NO_2 response

Electrical measurements in the term of sensitivity towards NO_2 have been done for:

- ZnO and In_2O_3 thick films which had been prepared in Torino (as it's illustrated above).
- ZnO thin films prepared by PV via sol-gel technique and ZnO nanorods (NR) prepared according to PV technology template of ZnO films obtained by Sol gel.
- ZnO nanowires (NW) prepared by AQ via electrospinning which were recrystallized at 500°C for 1 h.

Generally, there are some features to be considered in the evaluation of the responses:

1) Practical sensitivity: The change in $S = [R_g / R_a]$ for an estimated temperature and concentration of the target gas (NO_2).

2) Sensitivity from: the slope of the linear interpolation in a plot of log [Resistance] and log [ppm].

3) The response times in adsorption and desorption, the response time can therefore be defined as the time required for a sensor output to change from its previous state to a final settled value within an acceptable tolerance band.

Because sensors generally respond exponentially, they never actually reach their final value they just get closer and closer asymptotically until they are so close as to be regarded as settled.

There is an accepted way of stating response time as the values measured at the 90% T response [$t_{90\%\,(\text{air-to-gas})}$] and this could be calculated from the resistance time data.

4) Selectivity: i.e. the ability to discriminate the target gas (eg, NO_2) in the presence of interfering gases (e.g. H_2O)

It has been estimated for the thick films by measuring their sensitivity towards RH fig. (6.17).

5) Stability of the base line: that is, the ability to recover the base line (the one in the air) after desorption gas.

Electrical responses to NO_2 at different operating temperatures (for thick films)

Response of the two films ZnO and In_2O_3 towards NO_2 at different operating temperatures has been studied: each step has duration of 3 hours, for each temperature dry air is blown for 1h, and then a pulse of NO_2 at a concentration of 1 ppm for 1h and finally again air dried again for 1h.

Operating temperatures range from 100°C to 250°C. The whole test has a total duration of 12 hours (Fig.6.30).

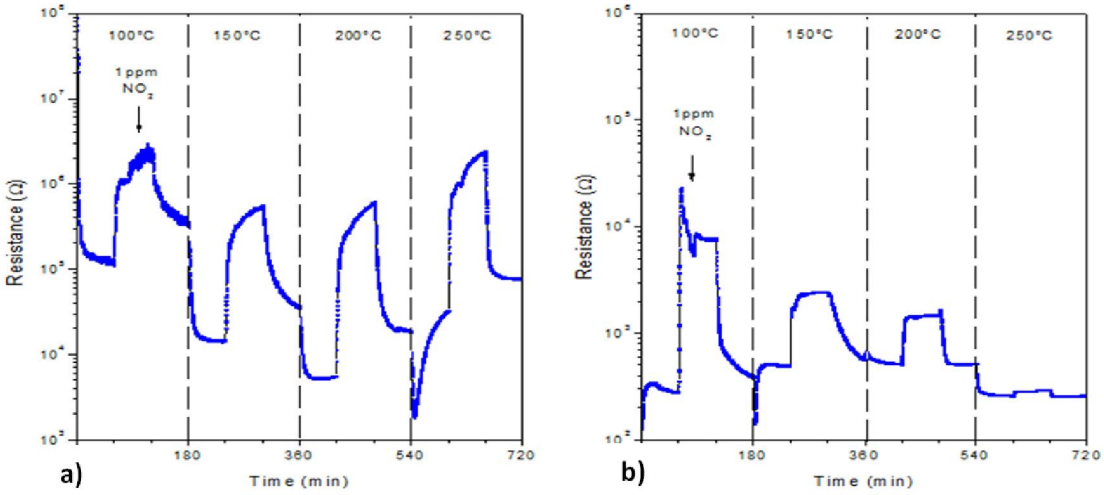

Fig.6.30: sensor signals of: a) ZnO film and b) In_2O_3 towards NO_2 at fixed concentration 1 ppm and different operating temperatures 100, 150, 200 and 250 ℃.

Therefore it seems that the best working temperatures are placed between 150 and 200°C. However, even at 250°C the sensor retains certain sensitivity, with discreet recovery of the base line and good response times (i.e. a square profile of the response).

The charts that follow present electrical responses to different concentrations of NO_2 at 2 working temperatures: 150 and 200°C (Fig.6.31).

Electrical responses to different concentrations of NO_2 at 150 °C (for thick films)

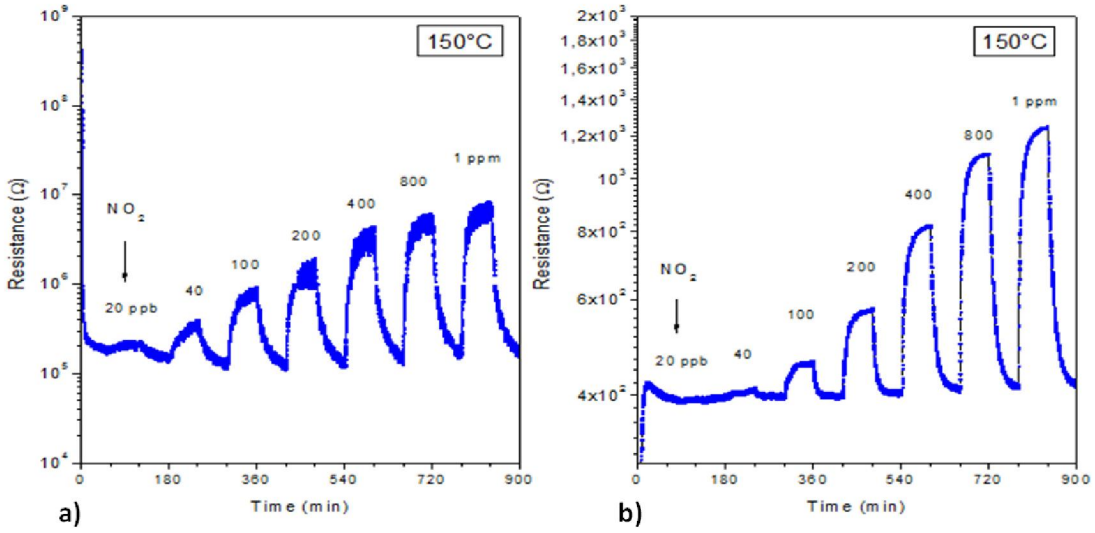

Fig.6.31: sensor signals of: a) ZnO film and b) In_2O_3 towards NO_2 at different concentrations (20 ppb - 1 ppm) and fixed operating temperature of 150˚C.

Each step of the curve has duration of 1 hour and for each temperature a ramp of concentrations ranging from 20 ppb to 1 ppm is made.

During each step dry air is blown for 1 h and then a flux of NO_2 concentration for 1 h is done. The whole test has a total duration of 15h.

From Fig.6.31, we can conclude that the limits of detection are 20 ppb and 40 ppb, respectively for the ZnO sensor and for the In_2O_3 film. To be considered for environmental applications (i.e. the quality of the air we breathe) devices must be capable of measuring concentrations of NO_2 in air at up to 200 ppb. These sensors have a detection limit that seems much lower. Also for the ZnO sensor we observe an increase of the detection limit from 20 to 40 ppb at 200°C, with respect to the results at 150°C.

Electrical responses to different concentrations of NO_2 at 200°C (for thick films)

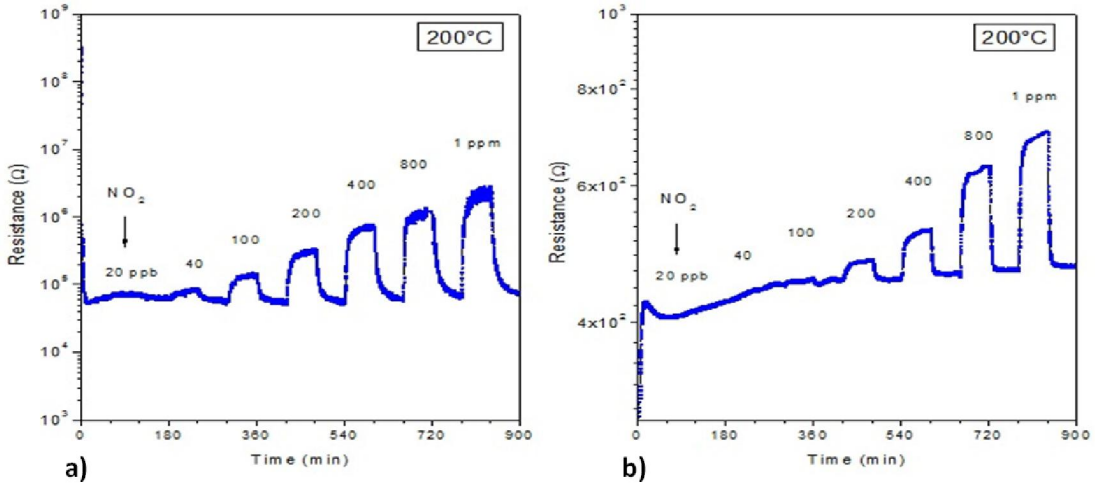

Fig.6.32: sensor signals of: a) ZnO film and b) In_2O_3 towards NO_2 at different concentrations (20 ppb - 1 ppm) and fixed operating temperatures 200 ˚C.

Fig.6.32 represents the sensor response of ZnO film and In_2O_3 film to NO_2 at different concentrations and operating temperature of 200°C: as each step has duration of 1 hour, for each temperature a ramp of concentrations ranging from 20 ppb to 1 ppm is made. During each step dry air is blown for 1 h and then a stream of NO_2 concentration for 1 h is done. The whole test has a total duration of 15 h.

From the previous figure, we can conclude that at 200°C, the detection limit for the sensor based on In_2O_3 film is in the range 100-200 ppb of NO_2. It also has a loss of sensitivity (in terms of change in the electrical impulse of gas). It improves on the other hand, the dynamic response (square plots).

ZnO thin film: Response to NO_2 at various temperatures

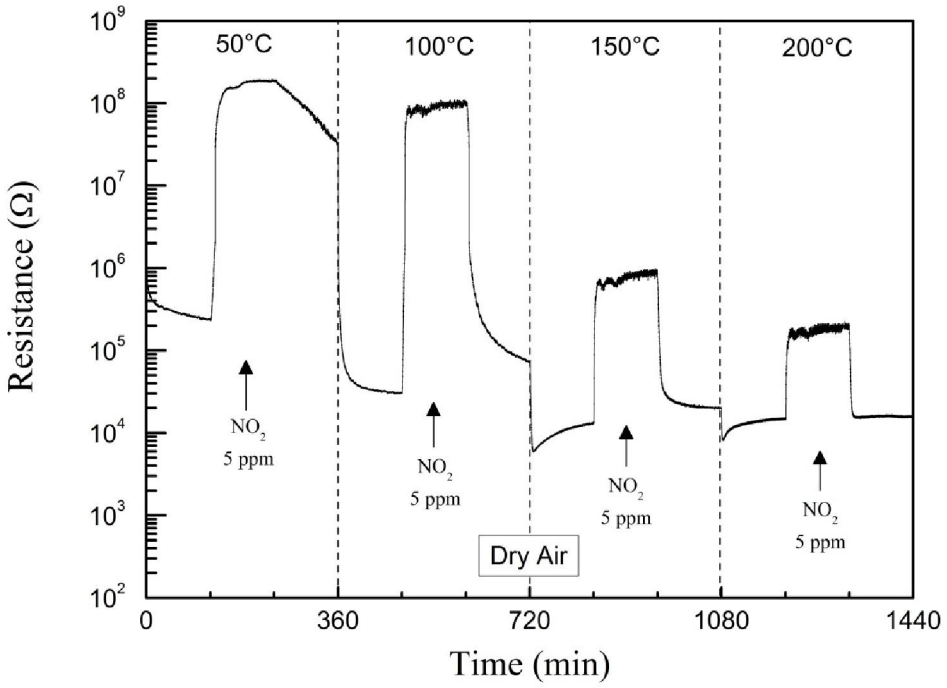

Fig.6.33: Change in sensor resistance for sol gel ZnO thin film exposed to 5 ppm of NO_2 in dry air at different working temperatures (50°C -100°C -150°C and 200°C)

The cycle for each temperature lasts 360 min and comprises 120 min of exposure in dry air, 120 min of exposure to 5 ppm of NO_2 and 120 min of exposure in dry air.

The NO_2 gas causes an increase in strength compared to that measured in air. The sensor behaves as an n-type semiconductor (charge carriers electrons).

The sensitivity of the sensor appears to be best at 100°C (increased ratio R_g / R_a). However we can see how the recovery of the base line should be faster with increasing temperature. It's quite clear that a total virtual recovery of the base line to the operating temperature of 200°C.

The best compromise between sensitivity and recovery of the base line seems to be obtained for a temperature of 150°C.

ZnO Nanorods (NR): Response to NO_2 at various temperatures

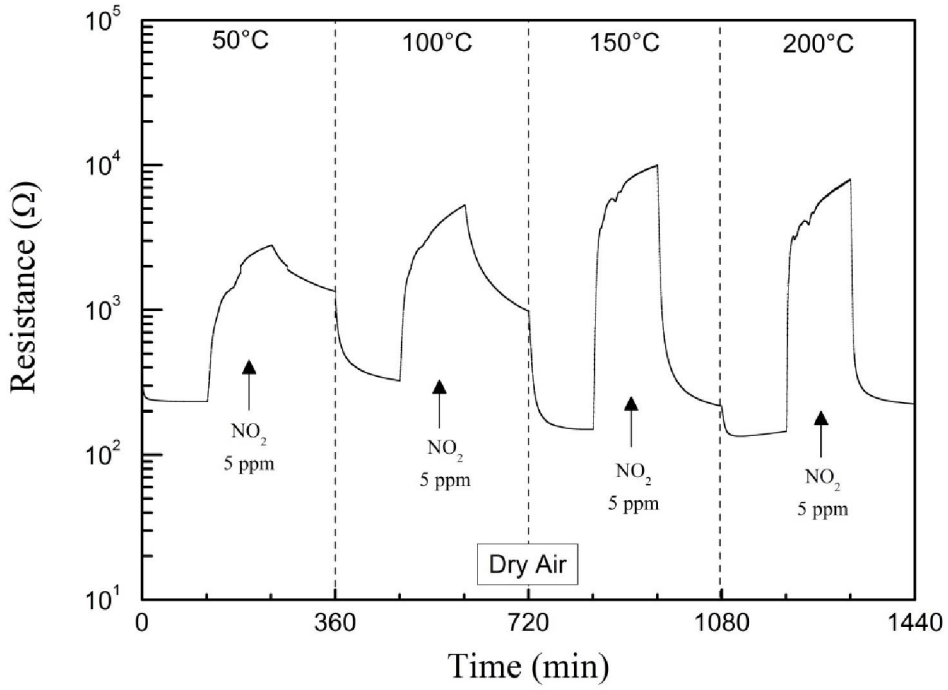

Fig.6.34: Change in sensor resistance sol gel ZnO-NR exposed to 5ppm of NO_2 in dry air at different working temperatures (50 °C -100 °C -150 °C and 200 °C).

The cycle for each temperature lasts 360 min and comprises 120 min of exposure in dry air, 120 min of exposure to 5 ppm of NO_2 and 120 min of exposure in dry air.

The NO_2 gas causes an increase in strength compared to that measured in air. The sensor behaves as an n-type semiconductor (charge carriers electrons).

The sensitivity of the sensor appears to be the best at 150°C (increased ratio R_g / R_a).

The recovery of the base line improves as the working temperature increases. However, the extent of recovery is almost equal when switching from 150°C to 200°C. However, the time of desorption is lower at 200°C.

The best compromise between sensitivity and recovery of the base line seems to be obtained for a temperature of 150°C.

ZnO thin film: Response to NO_2 at various concentrations to 150 °C and 200 °C

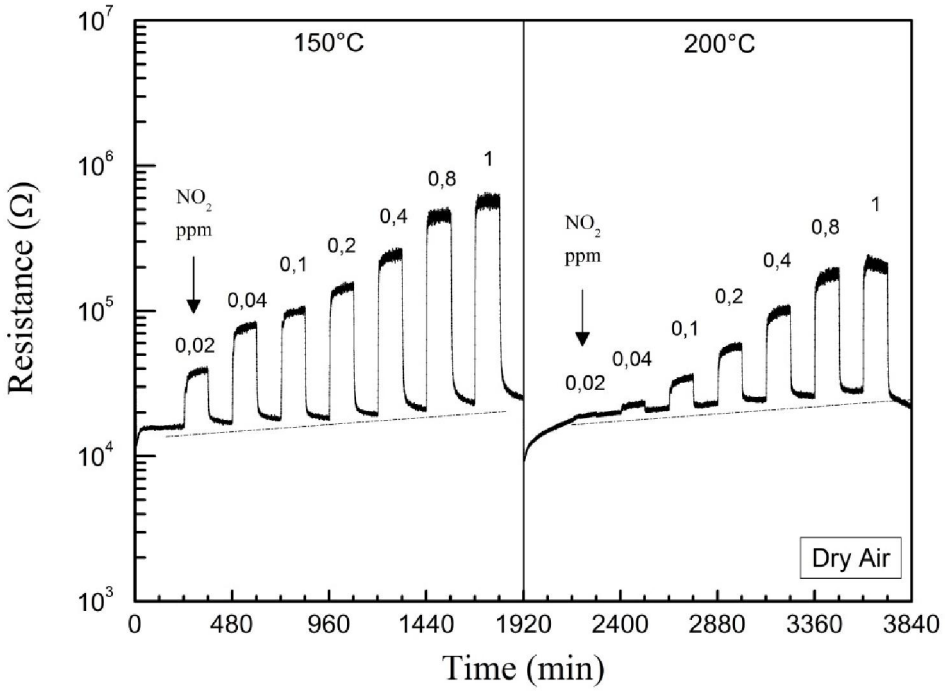

Fig.6.35: Change in sensor resistance for sol gel ZnO thin film exposed to different concentrations of NO_2 (from 20 ppb to 1 ppm) in dry air at different operating temperatures (150°C and 200°C)

The sensitivity of the sensor appears to be best at 150°C (increased ratio R_g / R_a): the minimum concentration detected is 20 ppb of NO_2. At 200°C, the minimum detectable concentration of NO_2 is 40 ppb. The baseline drift is slight but not significant for both operating temperatures.

ZnO Nanorods (NR): Response to NO_2 at various concentrations to 150 °C and 200 °C

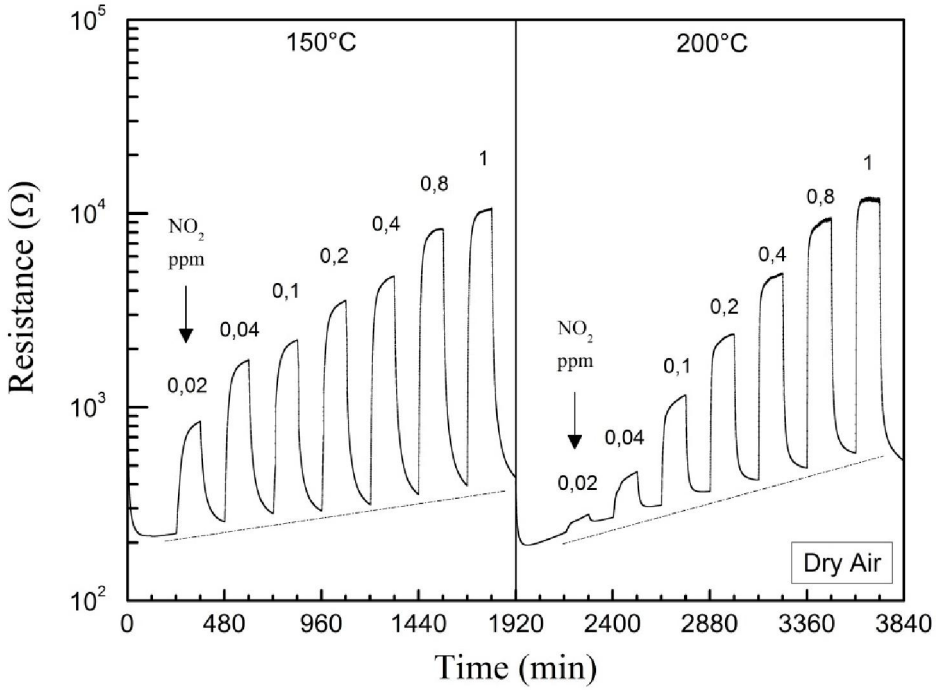

Fig.6.36: Change in sensor resistance for sol gel ZnO-NR exposed to different concentrations of NO_2 (from 20 ppb to 1 ppm) in dry air at different operating temperatures (150°C and 200°C)

The sensitivity of the sensor appears to be slightly better at 150°C (increased ratio R_g / R_a) particularly at low concentrations of NO_2. The minimum concentration detected is 20 ppb of NO_2 for both temperatures.

The base line has a slight drift at 150°C that increases if switching to an operating temperature of 200°C. Therefore, the temperature of 150°C seems to be the best temperature for the proper functioning of the sensor

Sensitivity Curve to NO_2 at 150°C

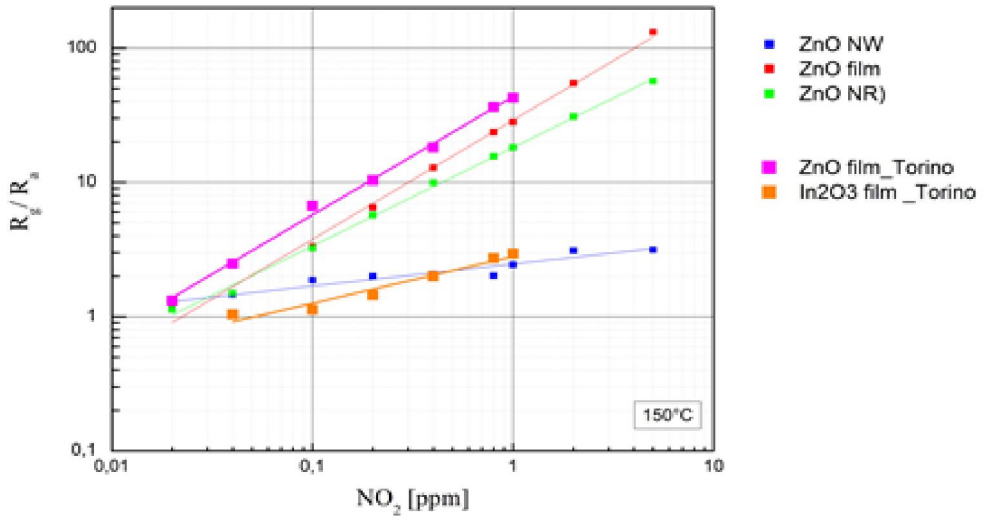

Fig.6.37: sensor response S of: ZnO and In_2O_3 thick films, ZnO thin film, ZnO-NR and ZnO-NW towards NO_2 at different concentrations (20 ppb - 1 ppm) and fixed operating temperatures 150 ℃.

Fig.6.37: shows a comparison of sensitivity (represented by straight interpolation) of the different prepared samples at 150°C and various NO_2 concentrations (20 ppb-1 ppm). It shows a diagram of a double logarithmic scale with linear interpolation of data sensitivity. Sensitivity is given by $S = (\frac{\Delta y}{\Delta x})$ where $\Delta y = R_g / R_a$ and Δx = [ppm].

Therefore, the sensitivity itself represents the resistance change (gain) for a given increase of the gas concentration.

Graphically, the sensitivity is given by the slope of the linear interpolation. Since the adsorption is represented by a curve of Langmuir (it is an exponential curve in scale moles adsorbed vs. Concentration) its representation in the graphic log / log is a straight line.

ZnO thick film and ZnO thin film have the best sensitivity and have almost the same slope.

References

1. J.-H. Lee, Review Gas sensors using hierarchical and hollow oxide nanostructures: Overview, Sens. Actuators B, 140 (2009) 319-336.
2. J. Shi, Y. Zhu, X. Zhang, W. R. G. Baeyens, A. M. Garcia-Campana, Recent developments in nanomaterial optical sensors, Tr. Anal. Chem., 23 (2004) 351-360.
3. D. Buso, G. Busato, M. Guglielmi, A. Martucci, V. Bello, G. Mattei, P. Mazzoldi and M. L. Post, Selective optical detection of H_2 and CO with SiO_2 sol–gel films containing NiO and Au nanoparticles, Nanotechnology, 18 (2007) 475505 (7pp).
4. Growth of cookie-like Au/NiO nanoparticles in SiO_2 Sol- gel Films and their optical gas sensing properties. D. Buso,M. Guglielmi, G. Mattei, P. Mazzoldi, C. Sada, M. L. Post, A. Martucci, Crystal Growth & Design 8 (2008) 744-749.
5. E. Della Gaspera, D. Buso, M. Guglielmi, A. Martucci,V. Bello, G. Mattei, M. L. Post, C. Cantalini, S. Agnoli, G. Granozzi, A. Z. Sadek , K. Kalantar-zadeh , W. Wlodarski, Comparison study of conductometric, optical and SAW gas sensors based on porous sol‑gel silica films doped with NiO and Au nanocrystals, Sensors and Actuators B 143 (2010) 567‑573.
6. Y. Xia, G. M. Whitesides, Soft Lithography, Annu. Rev. Mater. Sci. 28 (1998) 153-84.
7. O. F. Göbel, M. Nedelcu, U.Steiner, Soft Lithography of Ceramic Patterns, Adv. Funct. Mater, 17 (2007) 1131-1136.
8. K. Y. Suh, Y. S. Kim, H. H. Lee, Capillary force lithography, Advanced Materials, 13 (18) (2001) 1386-1398.

9. A. Ponzoni, E. Comini, G. Sberveglieri, J. Zhou, S. Z. Deng, N. S. Xu, Y. Ding and Z. L. Wang, Ultrasensitive and highly selective gas sensors using three-dimensional tungsten oxide nanowire networks, Applied physics letters 88 (2006) 203101.
10. Y. Zhang, J. Xu, Q. Xiang, H. Li, Q. Pan and P. Xu, "Brush-like hierarchical ZnO nanostructures: synthesis, photoluminescence and gas sensor properties", J Phys Chem C, 113(2009) 3430-3435.
11. G. Korotcenkov, Review Metal oxides for solid-state gas sensors: What determines our choice? Materials Science and Engineering B 139 (2007) 1–23.
12. Y. Ushio, M. Miyayama, H. Yanagida, Effects of interface states on gas-sensing properties of a CuO/ZnO thin-film heterojunction, Sens. Actuators B Chem. 17(1994) 221–226.
13. Ü. Özgür, Ya. I. Alivov, C. Liu, A. Teke, M. Reshchikov, S. Dogan, V. Avrutin, S.-J. Cho, and H. Morkoç, A comprehensive review of ZnO materials and devices, J. Appl. Phys. 98 (2005) 041301.
14. F. Liu, P. J. Cao, H. R. Zhang, J. Q. Li, H. J. Gao, Controlled self-assembled nanoaeroplanes, nanocombs, and tetrapod-like networks of zinc oxide Nanotechnology 15 (2004) 949.
15. Q. Wan, Q. H. Li, Y. J. Chen, T. H. Wang, X. L. He, J. P. Li, C. L. Lin, Fabrication and ethanol sensing characterization of ZnO nanowire gas sensor, Appl. Phys. Lett. 84 (2004) 3654 - 3656.
16. Z. Fan, D. Wang, P. Chang, W. Tseng, J. G. Lu, ZnO nanowire field Effect transistor and oxygen sensing property, Appl. Phys. Lett. 85 (2004) 5923 - 5925.

17. Q. Wan, C. L. Lin, X. B. Xu, T. H. Wang, Room temperature hydrogen storage characteristics of ZnO nano wires, Appl. Phys. Lett. 84 (2004) 124 – 126.

18. Z. Fan and J. G. Lu, Zinc Oxide Nanostructures: Synthesis and Properties 5 (2005) 1561-1573.

19. http://jpkc.whut.edu.cn/, 14/12/2012.

20. A. Qurashi, M. F. Irfan and M. W. Alam, In_2O_3 nanostructures and their chemical and biosensor applications, The Arabian Journal for Science and Engineering 1C 35 (2010) 125-145.

21. P.C. Xu, Z.X. Cheng, Q.Y. Pan, J.Q. Xu, Q. Xiang, W.J. Yu, Y.L. Chu, High aspect ratio In_2O_3 nanowires: synthesis, mechanism and NO_2 gas-sensing properties, Sensors and Actuators B: Chemical 130 (2008) 802‑808.

22. Ch.L. Chen, Y.L. Wei, D.R. Chen, X.L. Jiao, Indium oxide nanocrystals: capping-agent-free synthesis, size-control mechanism, and high gas-sensing performance, Materials Chemistry and Physics 125 (2011) 299‑304.

23. W. Zheng, X.F. Lu, W. Wang, Z.Y. Li, H.N. Zhang, Y. Wang, Z.J. Wang, C. Wang, A highly sensitive and fast-responding sensor based on electrospun In_2O_3 nanofibers, Sensors and Actuators B: Chemical 142 (2009) 61‑65.

24. A. Forleo, L. Francioso, M. Epifani, S. Capone, A.M. Taurino, P. Siciliano, NO_2- gas-sensing properties of mixed In_2O_3‑SnO_2 thin films, Thin Solid Films 490 (2005) 68‑73.

25. X. Xu, D. Wang, W. Wang, P. Sun, J. Ma, X. Liang, Y. Sun, Y. Ma, G. Lu, Porous hierarchical In_2O_3 nanostructures: Hydrothermal preparation and gas sensing properties, Sensors and Actuators B 171– 172 (2012) 1066– 1072.

Appendix – Experimental procedures

This section deals with the main experimental procedures used in this study for the elaboration and characterization of the used SMO sensors.

The analyses were fundamental to set up the right procedure and the proper treatments, in order to obtain a powder with the desired features, suitable to produce homogeneous and reliable components.

A.1. Pressing

The shaping of pellets can be performed by uniaxial pressing. Uniaxial pressing involves the compaction of powder into a rigid die by applying pressure in a single axial direction through a rigid punch or piston. The pressure was set at 370 MPa.

A.2. Natural sintering

The samples obtained by uniaxial pressing and by screen-printing were sintered in high temperature electrical furnace, in air, in the temperature range of 900°C – 1300°C.

A.3. X-Ray dìffraction (XRD)

The X-ray diffraction technique allows detecting the phase composition of the sample: in fact, each phase presents specific diffractions peaks, on the basis of the lattice structure and atom position. Moreover, this experimental method is employed to evaluate the structure of the crystalline materials and to measure the crystallite size.

X-ray diffraction analyses were carried out by using the conventional diffractometer Philips PW 1710, with a Cu Kα radiation (λ = 0.15405600 nm)

A schematic representation of the instrument is shown in Figure 1.

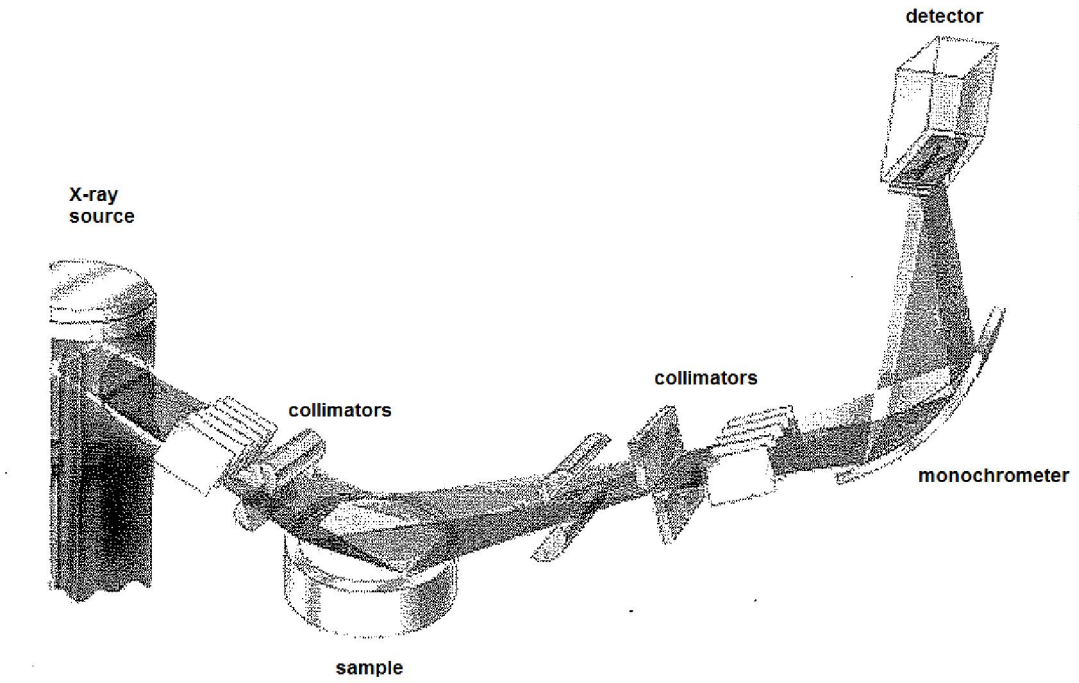

Figure 1 – Scheme of the XRD diffractometer

The X-ray source consists of a filament that heats the cathode, inducing electrons emission. The presence of two metallic electrodes, with a different potential, implies the acceleration of the electrons towards the anode (in this case, made of copper), which emits the X-ray beam having a specific wavelength range, on the basis of the metallic component and the applied tension.

The power employed in X-rays production is only 0.1%, whereas the leftover one is converted into heat, which could induce anode melting. To avoid it, a water cooling system is present.

X-rays pass through a monochromator (in this case, made of nickel), which selects the Kα radiation of copper. This radiation is then collimated upon the sample.

The instrument presents a goniometer having a Bragg-Brentano geometry, that operates in the 2 θ scanning regime, in which the detector (D) and the sample (S) move with respect to the X-rays source (X) in a synchronized way, as schematically presented in Figure 2.

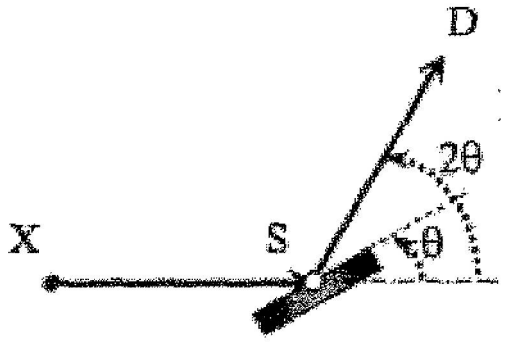

Figure 2 – Mechanism of the goniometer in the diffractometer Philips PW 1710

In this way, the incident and the diffracted beams form the same angle with the flat surface of the sample, whereas the diffracted beam forms a 2θ angle with the incident one (Figure 3).

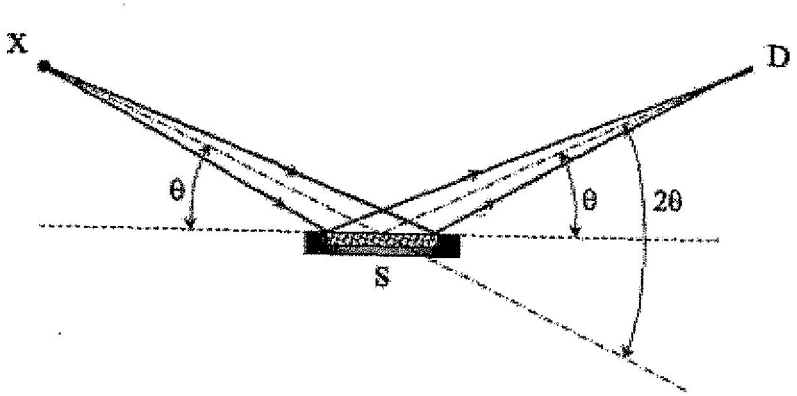

Figure 3 – The Bragg – Brentano geometry

This particular geometry is related to the Bragg equation, employed to evaluate the inter-planar distance in the crystalline lattice. In fact, when the X-rays hit the sample surface, they can interact with the lattice atoms, being their wavelength and the inter-atomic distance similar. The lattice atoms are then able to diffract the X-rays beam and a signal is recorded when a positive interference occurs, according to the Bragg equation:

$$n\lambda = 2d\sin\theta \qquad (1)$$

Where θ is the incident angle, d is the inter-atomic distance, λ is the wavelength of the X-rays beam and n is a number.

On the basis of the inter-atomic distances it is possible to evaluate the geometry and the dimensions of the elementary cell; the whole diffraction pattern allows the identification of the phases through the comparison with the ICDD (International Centre for Diffraction Data) files. In addition, the peak intensity depends on the atom position in the elementary cell: more intense are the signals, more crystalline is the sample. In this study, XRD was used to investigate the phases present in the produced powders.

The average crystallite size was ca1cu1ted by the line-broadening method, using the Scherrer's equation.

$$D = \frac{k..\lambda}{\beta.\cos\theta}$$

Where D is the crystalline size, λ is the wavelength of the Cu Kα line, k is the Scherrer's constant, assumed to be equal to 0.9, and β is the full width at half maximum of the main powder peak, assuming a Gaussian profile [1,2].

A.4. Laser granulometry

When a laser beam strikes the particles suspended in an inert medium, the produced diffracted rays present intensity and diffraction angle that depend on the size of the impacted particle.

As illustrated in Figure 4, a laser granulorneter consists of a laser beam source, at a fixed wavelength, and a series of detectors (multidiode detector) to measure the diffracted light as a function of the diffraction angle.

The granulometer Malvern Mastersizer 2000 was used to evaluate the particle size distribution of the powders dispersed in ethanol. The Mie theory is used by the instrument to calculate the particle size distribution. This theory takes into account both the diffraction index and the refractive index of both the sample and the medium. The powders were dispersed in ethanol and deagglomerated for 5 minutes, prior to each measurement.

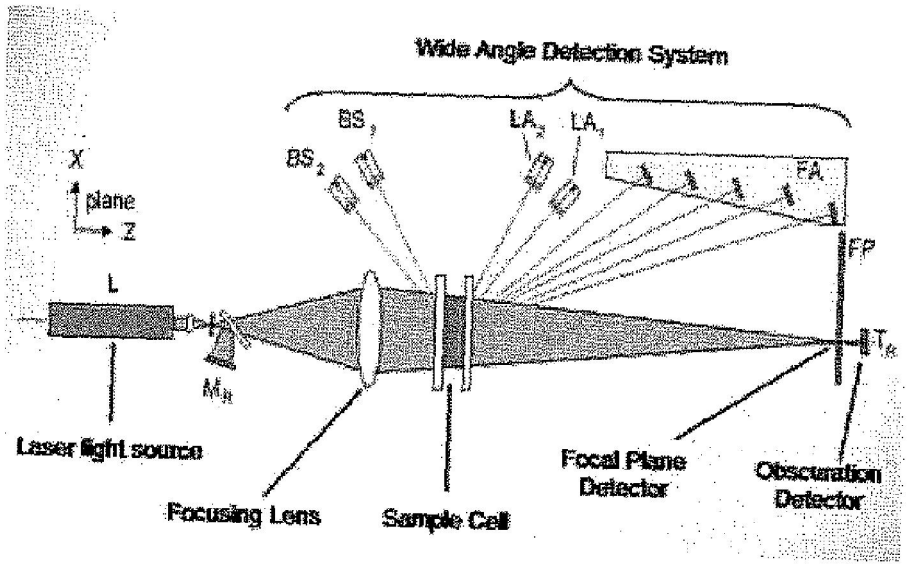

Figure 4 – Schematic representation of a laser granulometer

A.5. SEM

The Scanning Electron Microscopy (SEM) is a technique that allows a morphological characterization of powdered and massive samples. It uses the electrons for imaging, reaching higher magnifications and greater depth field than the light microscopy.

A schematic representation of an instrument is reported in Figure 5: from the electron emission source, a heated tungsten filament, the beam is focused on the sample surfaces by a series of electromagnetic lenses. The incident electrons imply electrons emission from the sample surface; they are collected by a suitable detector, during the scanning of a raster pattern, producing a topographical image of the analyzed surface. Some observations were performed in SE (secondary electrons) modality, while, when a phase contrast was needed BSE (back scattered electrons) were also detected.

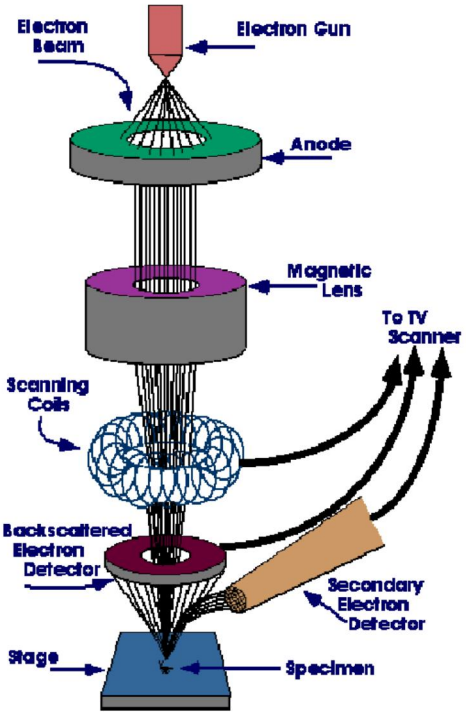

Figure 5 – Schematic representation of a SEM instrument [3]

The powders and the microstructure of the materials were observed by using SEM Hitachi S2300, and FE-SEM (Hitachi S4000 and Zeiss Merlin). A gold (chromium for FE-SEM observations) sputtering pre - treatment of all samples in order to increase the sample conductivity was usually used. The grains size was measured on polished samples, which were thermally etched at a lower temperature than the sintering one, depending on the specific SEM instrument used for the observation. This thermal etching allows revealing grain boundary for SEM observation.

A.6. Porosimetry

Porosimetry is an analytical technique used to determine various quantifiable aspects of a material's porous nature, such as pore diameter, total pore volume, surface area, and bulk and absolute densities.

The technique involves the intrusion of a non-wetting liquid (often mercury) at high pressure into a material through the use of a porosimeter. The pore size can be determined based on the external pressure needed to force the liquid into a pore against the opposing force of the liquid's surface tension.

A force balance equation known as Washburn's equation for the above material having cylindrical pores is given as:

$$P_L - P_G = \frac{4\sigma \cos\theta}{D_P}$$

P_L = pressure of liquid

P_G = pressure of gas

σ = surface tension of liquid

θ = contact angle of intrusion liquid

D_P = pore diameter

Since the technique is usually done under vacuum, the gas pressure begins at zero. The contact angle of mercury with most solids is between 135° and 142°, so an average of

140° can be taken without much error. The surface tension of mercury at 20°C under vacuum is 480 mN/m. With the various substitutions, the equation becomes:

$$D_P = \frac{1470 kPa.\mu m}{P_L}$$

As pressure increases, so does the cumulative pore volume. From the cumulative pore volume, one can find the pressure and pore diameter where 50% of the total volume has been intruded to give the median pore diameter.

A.7. The screen-printing technique

The screen-printing consists in forcing a rubber or plastic flexible blade, called squeegee, to transfer an ink onto the substrate through a screen (Figure 6).

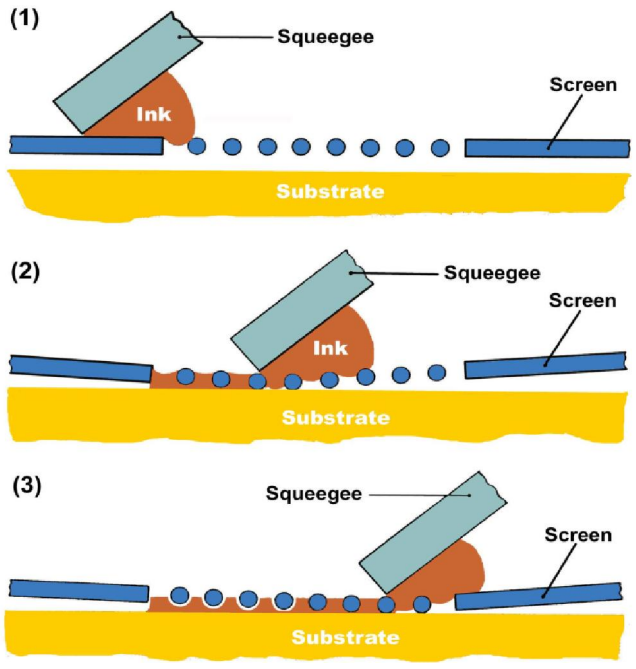

Figure 6 – The basic screen-printing process [4].

The screen defines the pattern of the printed film and also meters the amount of paste deposited onto the substrate. The most common type of screen comprises a frame, normally cast aluminum or stainless steel, onto which a finely woven mesh is stretched. The mesh itself is usually based on a plain weave pattern, as depicted in Figure 7.

For general purpose work, a typical mesh count might be 200 strands per inch: the mesh opening depends on the mesh count and the filament diameter. For a given mesh count, the smaller the filament diameter, the larger the mesh opening which will therefore allow a greater volume of ink to be deposited onto the substrate. Hence, the mesh opening provides one of the means of checking the thickness of the deposit.

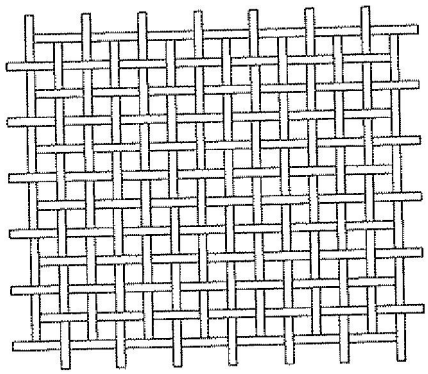

Figure 7 – A plain weave pattern for a typical thick film screen

It is possible to quantify the percentage open area of mesh through which the ink is able to pass:

$$Percentage = \frac{100A^2}{(A+D)^2} \qquad (2)$$

where A is the mesh aperture and D is the filament diameter.

A cross-section of a mesh and many definitions and terms used are shown in Figure 8.

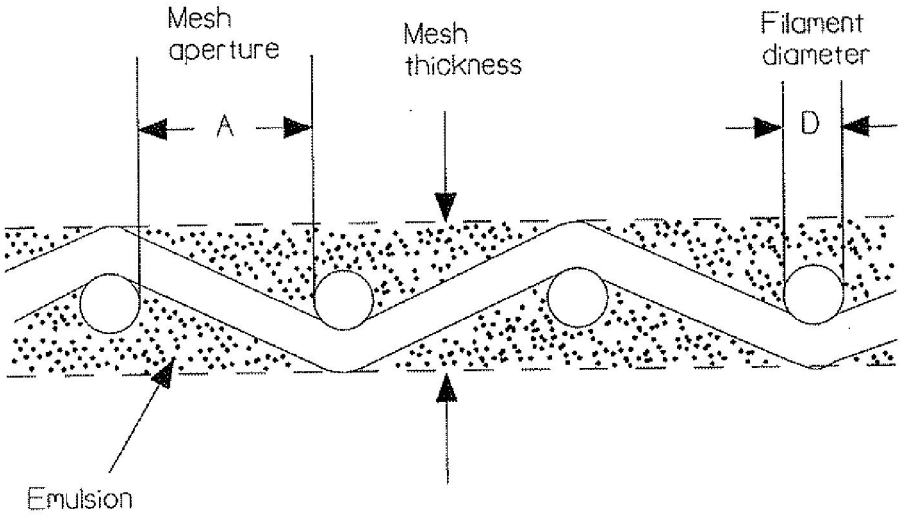

Figure 8 – Cross-section of a screen mesh

The pictures of the semi-automatic screen-printing machine used in laboratory to realize sensors are shown in Figure 9, while the masks used to screen print the components of the sensors are presented in Figure 10: in particular the screen's patterns can be different depending on what it is deposited, for example in laboratory two screens were used, the former to print the electrodes (Figure 10a), the latter to deposite the sensing layer (Figure 10b).

The screens used were all made of stainless steel and their apertures were 270 mesh, corresponding to 53 μm.

Figure 9 – Screen printer used for sensors assembly

a) 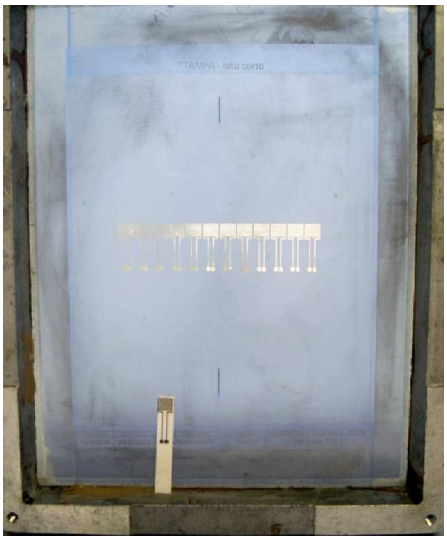 b) 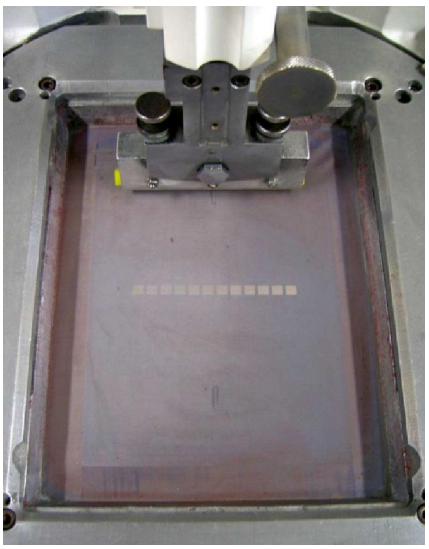

Figure 10 – Patterns of the screens used to screen print the a) electrodes and b) rectangular sensing films

A.8. Screen-printing inks

Each paste for producing thick films contains three components: the basic component, the flux and the binding phase.

The flux is a component, also called organic vehicle, which provides a homogeneous suspension of the particles of the basic components and a rheology suitable for the printing of the film configuration. Hence, the vehicle is a temporary, sacrificial ingredient, which should be removed completely in the following steps of the process, during which the microstructure of the deposits is formed.

The typical rheological behaviour of a screen-printing ink is reported in Figure 11.

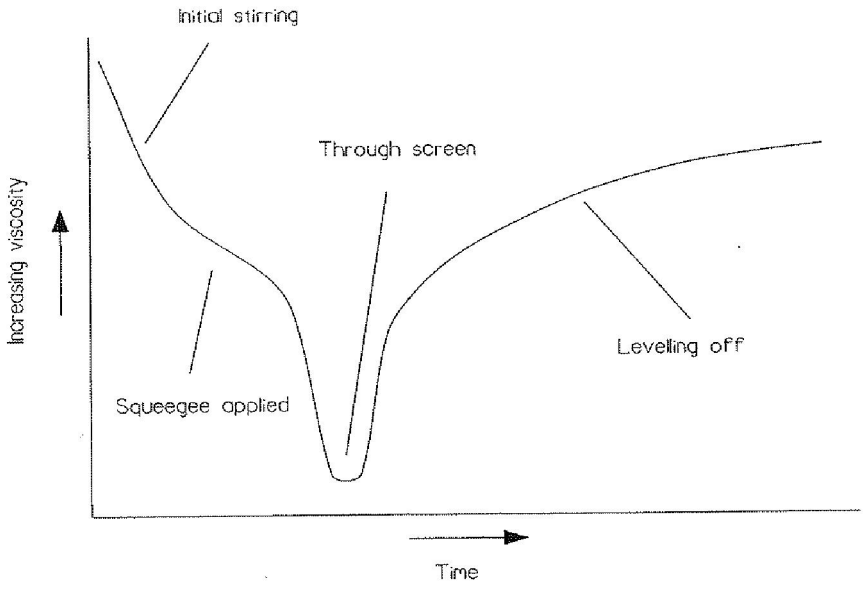

Figure 11 – Rheological behaviour of a screen-printing ink.

The rheological behaviour a paste should have is thixotropic, because firstly the ink must easily pass through the weaves of the screen thanks to the squeegee's action and then it regains its starting viscosity, such that the deposit keeps the shape of the screen's apertures when it is onto the substrate. So, referring to Figure 11, the paste's viscosity must first of all decrease during the squeegee's action, then it must rapidly increase when it passes through the screen, coming back to its starting value.

It is possible to remove the sacrificial ingredient by considering two steps: the drying and the firing processes.

In general these two steps are necessary for sensors realization: after printing, the film or electrodes should stand in air for few minutes/hours, in order for the ink to level off and settle. The object of the drying stage is to remove the organic solvents and make the printed film adherent to the substrate and relatively immune to smudging. The organic agent is still present in the ink at this stage; drying takes place at temperatures between 100-150°C in a conventional box oven.

The firing process is a phase in which the printed films or electrodes are heat treated for higher temperatures: the thermal program is specifically studied for every sample. At this step, the ink's components are thermally decomposed, leading to an evident shrinkage of the deposit (Figure 12).

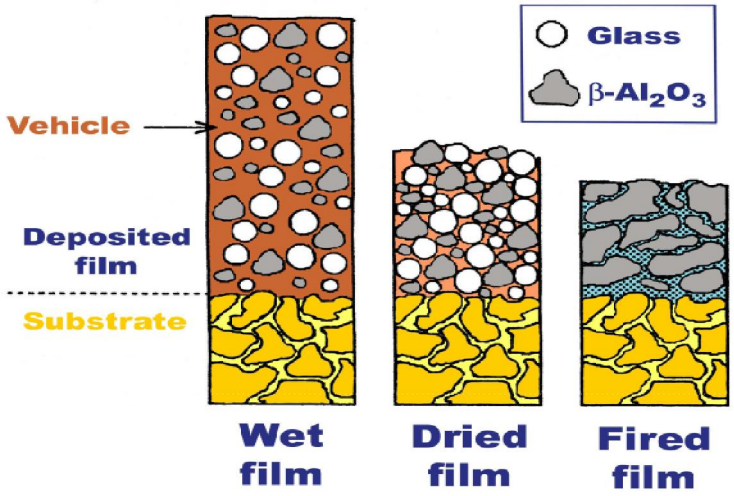

Figure 12 – Shrinkage of the thick film from the wet to the dried phase, followed by the fired stage. As an example, the basic component chosen is α-Al_2O_3

In laboratory, the organic vehicle used to realize the inks, was a blend of terpineol-type solvent, namely ethylene glycol monobutyal ether (Emflow, Emca Remex, USA). The binding phase was poly-(vinyl butyral-co-vinyl alcohol-co-vinyl acetate)

(PVB, Aldrich, USA), which created the paste plasticity and ensured the necessary adhesion of the film to the substrate before the paste was fired.

In particular, for all the pastes realized, 0.053 g of PVB and 1.2 cc of Emflow were used: these components were mixed overnight by ball-milling, in order to obtain a homogeneous viscous liquid, and then 2 g of the basic components (doped hematite) were added and mixed to the liquid, thus obtaining a dense paste, ready to be printed on the substrate. Actually two different architectures were developed to create the ceramic sensors: the first one was the classical way to realize screen-printed devices, in particular the sensing films were deposited onto α-Al_2O_3 planar substrates (Coors Tek, USA, ADS-96 R, 96% alumina, 0.85 cm × 5 cm^2) and, on top of them, interdigitated electrodes were printed, while the second one dealt with interdigitated electrodes printed onto the substrate and the sensing layer overlapped them.

Interdigitated gold electrodes were used for sensors assembly: starting from a commercial ink (ESL EUROPE 8835 (520C)), the gold paste was screen-printed onto a α-Al_2O_3 substrate by using a rubber squeegee, or onto the sensing materials: after drying overnight, the electrodes were dried and fired at 520°C for 18 minutes with a 2°C/min heating ramp to optimize their electrical conductivity, according to the ink's manufacturer recommendations.

Figure 13 refers to the architecture's sensors, obtained by printing the paste containing the sensing material (Figure 13b, in particular the ink was composed by Sr-doped hematite powder) onto an alumina substrate (Figure 13a). After the sintering treatment of the paste, gold interdigitated electrodes were printed onto the sensing material (Figure 13c), followed by a firing process.

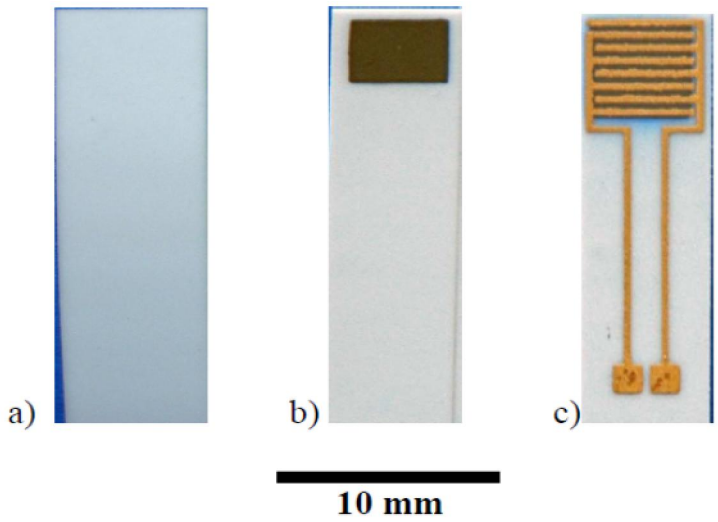

Figure 13 – Steps for the first architecture's sensors assembly

A.9. Humidity measurement device

Humidity test of the sensors were carried out by using a laboratory apparatus for their testing made of a thermostated chamber, operating at 25°C, in which relative humidity (RH) could be varied between 0 and 96%. In this system, referring to Fig. 14, compressed air was separated into two fluxes: one was dehydrated over a chromatography alumina bed, while the second one was directed through two water bubblers, generating, respectively, a dry and a humid flow [5]. Two precision microvalves allowed to recombine the two fluxes into one by means of a mixer and to adjust the RH content while keeping constant the testing conditions: a flow rate of 0.05 L/s. The ammonia flux was obtained by diluting an ammonium hydroxide solution (Fluka, USA) in deionized water (ratio 1:20) into a drechsel through which a known air flow was allowed to bubble. The laboratory apparatus for sensors testing was calibrated such that to ensure a constant air flow during electrical measurements and relative humidity (RH) was varied by steps, each one of 3 minutes.

An external alternating voltage (V = 3.6 V & 1 kHz) was applied on each tested sensor, placed into a PVC tube, acting as a variable resistance of the electrical circuit described above. The sensor resistance was determined by a calibration curve (Fig. 15), drawn by substituting the sensors, in the circuit, by known resistances. In particular, the sensors operated from about 1.3 V to 2.4 V, corresponding to about 700 kΩto 7 kΩ.

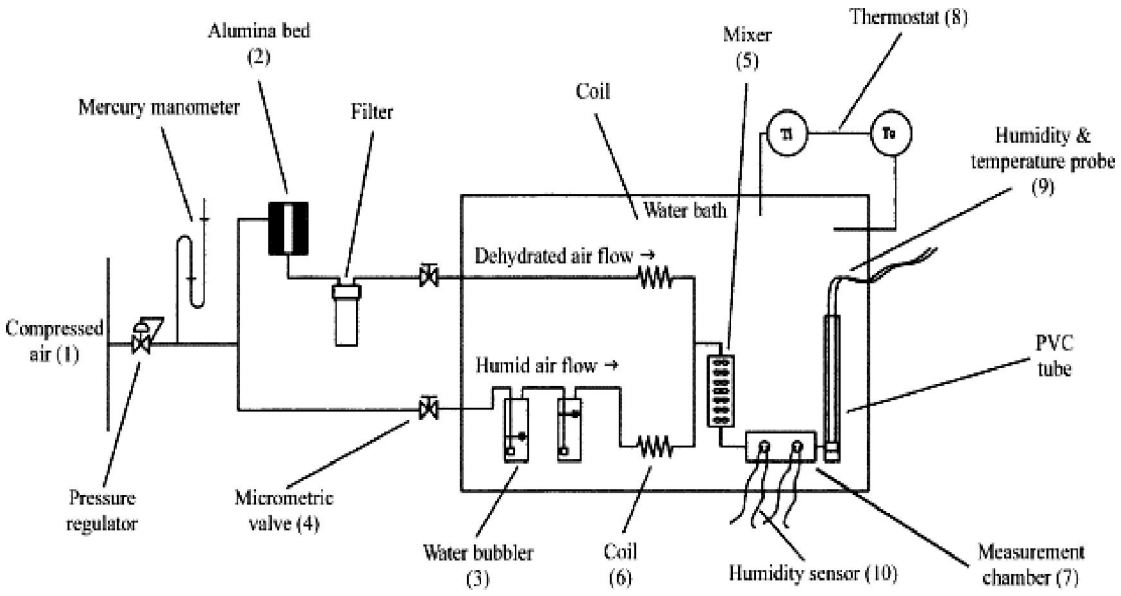

Figure 14 – Schematic representation of the laboratory apparatus for sensors testing [5]

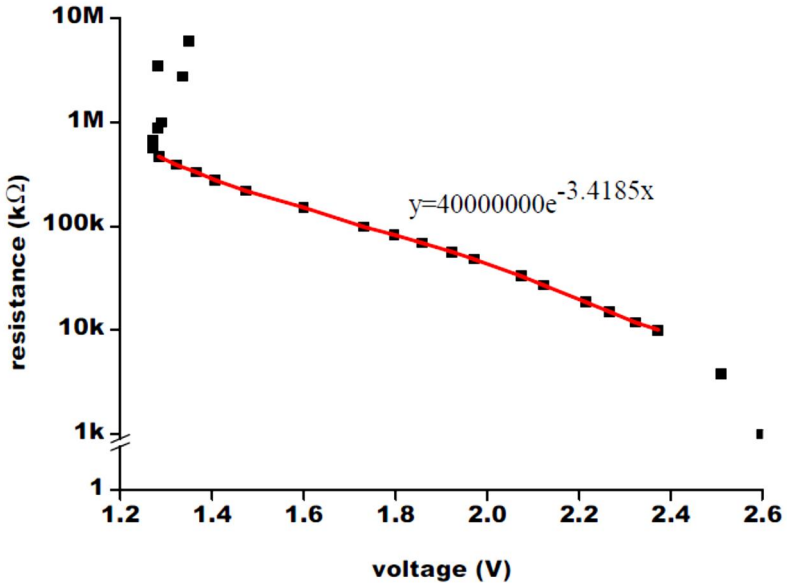

Figure 15 – Calibration curve for sensors testing: the red fit indicates the range of voltage in which the sensors operated. In the equation, y indicates the resistance, x the voltage.

RH values were measured by means of a commercial humidity and temperature probe (Delta Ohm DO9406, Italy, accuracy: ± 2.5% in the 5-90% RH range).

A.10. Impedance spectroscopy

Impedance spectroscopy (IS) is a general term that subsumes the small-signal measurement of the linear electrical response of a material of interest (including electrode effects) and the subsequent analysis of the response to yield useful information about the physicochemical properties of the system.

The impedance spectroscopy permit the measurement of the response of a system subject to an electric perturbation of an alternative voltage with a variable frequency and at a weak amplitude.

The amplitude in this case is function of the complex impedance Z (ω) of the system

$$Z(\omega) = U(\omega) / I(\omega)$$

Where Z (ω) is the complex impedance, U (ω) is the voltage and I (ω) is the intensity. Resistance R, capacity C and inductance L are the principal electric dipoles, the assembly of these dipoles permit to translate the impedance of a system in a electric circuit equivalent.

The behaviour of a material could be comparable to a capacitor or a resistance.

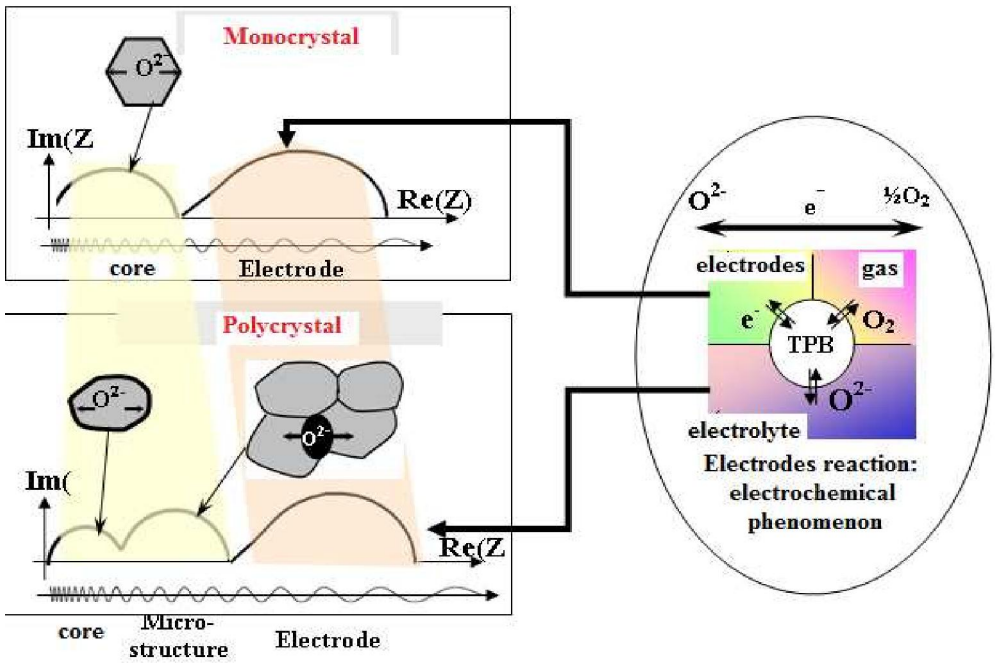

Figure 16 – The principle of the impedance spectroscopy

In the Figure 16, different electric responses of ceramic materials are reported, at low frequency the phenomenon of polarization inter-granular gives information to the electric properties of the microstructure of the sample depending on the joints of the grains and the porosity of the material.

The impedance of a system is an association of dipoles and could be represent by the Nyquist representation (Figure 17).

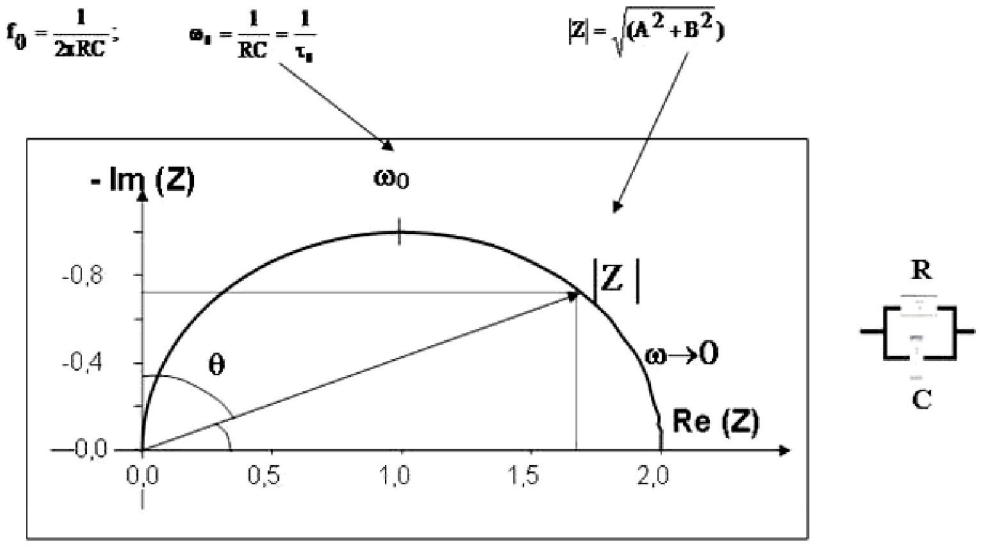

Figure 17 – Nyquist representation of a circuit

Where R is the resistance in ohms (Ω), C is the capacity in Farad (F), ω (=2πf) is the pulsation of the alternative signal of the measurement, |Z| is the Z module and f0 is the frequency in Hertz (Hz).

The impedance representation with the Nyquist method (-Im(Z) = f (Re(Z)) is a semicircle with the centre on the x-axis and the diameter R.

The intersection of the semicircle on the x-axis is the total resistance of the material, it is the value used in the data elaboration; the electric circuit equivalent is used to determinate these value.

A.11 BET analysis

In 1938, Stephen Brunauer, Paul Hugh Emmett, and Edward Teller published an article about the BET theory in a journal [7] for the first time; "BET" consists of the first initials of their family names.

BET theory aims to explain the physical adsorption of gas molecules on a solid surface and serves as the basis for an important analysis technique for the measurement of the specific surface area of a material.

The concept of the theory is an extension of the Langmuir theory, which is a theory for monolayer molecular adsorption, to multilayer adsorption with the following hypotheses:

1. Gas molecules physically adsorb on a solid in layers infinitely;

2. There is no interaction between each adsorption layer;

3. The Langmuir theory can be applied to each layer. The resulting BET equation is expressed by:

$$\frac{1}{[(P_0/P)-1]} = \frac{c-1}{V_m c}\left(\frac{P}{P_0}\right) + \frac{1}{V_m c} \qquad (3)$$

Where P and P_0 are the equilibrium and the saturation pressure of adsorbates

at the temperature of adsorption, v is the adsorbed gas quantity (for example, in volume units), V_m is the monolayer adsorbed gas quantity and c is the BET constant, which is expressed by:

$$c = \exp\left(\frac{E_1 - E_L}{RT}\right) \qquad (4)$$

E_1 is the heat of adsorption for the first layer, and E_L is that for the second and higher layers and is equal to the heat of liquefaction.

Equation (3) is an adsorption isotherm and can be plotted as a straight line with $1/v[(P_0/P)-1]$ on the y-axis and $\phi = (P/P_0)$ on the x-axis according to experimental results (Fig. 18).

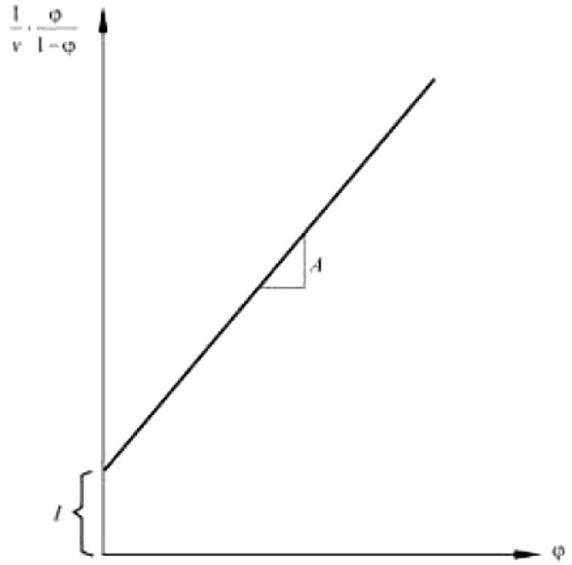

Figure 18. Schematic representation of a BET plot.

This plot is called a BET plot. The linear relationship of this equation is maintained only in the range of $0.05 < P/P_0 < 0.35$. The value of the slope A and the y-intercept I of the line are used to calculate the monolayer adsorbed gas quantity V*m* and the BET constant c. The following equations can be used:

$$V_m = \frac{1}{A+1} \qquad (5)$$

$$c = 1 + \frac{A}{I} \qquad (6)$$

The BET method is widely used in surface science for the calculation of surface areas of solids by physical adsorption of gas molecules. A total surface area S_{total} and a specific surface area S are evaluated by the following equation:

$$S_{BET,total} = \frac{V_m NS}{V} \quad (7)$$

Where V*m* is in units of volume which are also the units of the molar volume of the adsorbate gas:

$$S_{BET} = \frac{S_{total}}{a} \quad (8)$$

Where N is Avogadro's number, s is the adsorption cross section of the adsorbing species, V the molar volume of adsorbate gas and a is the mass of adsorbent (in g). The BET analyses were carried out by using the ASAP 2010 Micromeritics instrument.

References

1. L. V Azároff, R. Kaplow, N. Kato, R. J. Weiss, A. J. C. Wilson, R. A. Young, X-ray diffraction, (1974), McGraw-Hill.
2. P. Scherrer, G. N. Gesell 2 (1918) 98.
3. http://abidibo.otto.to.it/contents/attached/c4/sem2.gif.
4. G. Franzosi and J. M. Tulliani, Serigraa: tecnica preferita per la realizzazione di sensori a gas, Ceramurgia 4 (1999) 273-283.
5. J.-M. Tulliani, P. Bonville, Influence of the dopants on the electrical resistance of hematite-based humidity sensors, Ceramics International 31 (2005) 507–514.
6. S. Brunauer, P. H. Emmett and E. Teller, J. Am. Chem. Soc., 1938, 60, 309. doi:10.1021/ja01269a023.